# THERMAL STEREOLITHOGRAPHY OF HIGH-PERFORMANCE POLYMER DERIVED CERAMICS

By

Evelyn Wang

# A DISSERTATION

Submitted to
Michigan State University
in partial fulfillment of the requirements
for the degree of

Materials Science and Engineering – Doctor of Philosophy

2025

# **ABSTRACT**

This dissertation aims to develop a novel thermal stereolithography process for shaping polymer-derived ceramics (PDCs). This method solves issues in UV-based additive manufacturing (AM) for ceramic resin 3D printing where high refractive index (RI) fillers lead to low light penetration and resolution. By adopting a thermal NIR laser for the SLA process and using thermal curing, higher loadings of ceramics with higher RI difference between the particles and the resin can be processed. As a result, resin formulations based on SiC, Si, and Si<sub>3</sub>N<sub>4</sub> precursors can be processed with SLA printing to yield 3D structured green bodies that can undergo subsequent pyrolysis to ceramics.

In the first part of the research, an acrylate-based resin composition was proposed for SiC-Composite ceramics thermal SLA. This resin composition is based on passive fillers, which do not change throughout the entire process but contribute to the final ceramic yield. The printed structures are debinded and subject to polymer infiltration pyrolysis (PIP), which densifies and strengthens the printed structures. Using a small amount of preceramic polymer in the resin, a percolated structure was formed between particles during debinding to provide additional support for the porous green part. Various 2 D and 2.5 D structures and lattices composed of SiC-Composite ceramics were fabricated through this process, which has improved mechanical properties (flexural strength and toughness) at low pyrolysis temperatures (800 °C).

In the second part of the research, a preceramic polymer (PCPs)-based resin was utilized for AM of highly crystalline SiC-Composite ceramics using reaction bonding. Elemental silicon nanoparticles were blended into the resin composition as active fillers. This printing of silicon particle-containing resin is only achievable with the thermal SLA process, as silicon has an

extremely high RI of 5.44, compared to a refractive index of the resin of approximately 1.4 - 1.6. The addition of active fillers eliminates the residual carbon from PCP pyrolysis at elevated temperatures and improves mechanical properties.

In-situ Raman spectroscopy was used to characterize the polymer-to-ceramic conversion process for PDCs. This analysis allowed for real-time reaction rates to be measured. The high-temperature polymer reaction kinetics were analyzed with the in-situ setup, and the reaction kinetics were clearly illustrated in this research with complementary ex-situ studies. Finally, highly crystalline SiC-Composite ceramics with overhangs are demonstrated with both lab-scale thermal printers and 3DCeram, Sinto industrial printers. Finite element analysis (FEA) for thermal printing was also conducted to optimize the printing process and maximize the printing resolution.

#### **ACKNOWLEDGEMENTS**

This material is based on work supported by the Department of Energy (DOE) under the Award No. DE-EE0009407. All the analysis, findings, conclusions, and opinions expressed herein are solely those of the dissertation author and do not stand for DOE's view.

I want to give my most sincere thanks to my advisor, Dr. Hickner, for his support, guidance, and motivation throughout my doctoral studies. It has been a challenging and difficult four-year journey for me, filled with ups and downs. Thanks to the guidance and help from my advisor, Dr. Hickner, I was able to survive through all these challenges.

Additionally, I want to give my thanks to the Hickner group research for helping me through my research. I want to thank Dr. Harrison Cassidy for showing me the most awesome experimental setups; I want to thank Charles Rafalko and Dr. Houxiang Li for helping me with engineering issues; and Dr. Megan Matta for chemistry knowledge. Furthermore, I want to thank Dr. Shruti Gupta for supporting me and pointing out directions when I first entered the group. All the help from the group members means a lot to me, and I am honored to have you.

I want to give special acknowledgment to all the MCL and EB staff from Penn State University and Michigan State University; without their help, I could not have finished all the results of this dissertation. I am very grateful to Julie Anderson, Nichole Wonderling, Jeff Shallenberger, Dean Anderson, TJ, Bangzhi Liu, Per Askeland, and Ed Drown for their precious guidance and help.

Finally, I want to acknowledge my family members and those who helped me throughout the journey. I want to thank my parents, sisters, and all my friends who supported me and helped me during my most difficult days. And, of course, I want to thank Dr. Elizabeth Cardinale, Dr.

Rajveer Purohit, and Dr. Stacy Bull for giving me strength and another chance to embrace a new, more challenging, and fruitful journey.

Thank you to everyone who guided me and helped me in the doctoral journey; these memories will motivate me and lead me to another higher success in the future.

# TABLE OF CONTENTS

CHAPTER 1: INTRODUCTION	. 1
CHAPTER 2: LITERATURE REVIEW	. 6
CHAPTER 3: THERMAL SLA OF SIC-LOADED ACRYLATE RESINS WITH PDC	21
CHAPTER 4: STRUCTURED PDC COMPOSITES VIA NIR THERMAL SLA	46
CHAPTER 5: ADVANCING HIGH-PERFORMANCE CRYSTALLINE REACTION- SONDED PDCS THROUGH THERMAL SLA	56
CHAPTER 6: <i>IN-SITU</i> RAMAN CHARACTERIZATION FOR POLYMER-TO-CERAMIC RANSITION AND REACTION KINETICS	<del>9</del> 0
CHAPTER 7: ENGINEERING THE PRINTING RESOLUTION OF THERMAL SLA 12	20
CHAPTER 8: CONCLUSION14	<del>1</del> 0
SIBLIOGRAPHY14	43

#### **CHAPTER 1: INTRODUCTION**

#### 1.1. Overview

Ceramics, an ancient material dating back to approximately 24,000 BC<sup>1</sup>, were developed for daily human applications between 6,000 and 4,000 BC<sup>1</sup>. Their exceptional refractivity, strength, and hardness have secured their unique position in diverse applications<sup>2</sup>, ranging from home appliances to refractory furnaces. However, these advantageous properties are counterbalanced by inherent drawbacks, including brittleness, hardness, and limited processing flexibility<sup>3</sup>, which constrain<sup>3,4</sup> their production and application<sup>5</sup>.

The advent of technical ceramics<sup>6</sup>, such as silicon carbide (SiC), silicon carbonitride (SiCN), boron nitride (BN), silicon oxycarbide (SiOC), silicon nitride (Si<sub>3</sub>N<sub>4</sub>), and silicon oxynitride (SiON), have garnered significant interest in aerospace, medical, automotive, and extreme environment applications<sup>7,8</sup> due to their exceptional high-temperature performance, mechanical properties, and hardness. Compared to other material families, including polymers, metals, and composites, technical ceramics and composite ceramics have expanded their applications<sup>9</sup> across numerous fields. However, traditional top-down processing methods, limited by the inherent brittleness and hardness of these materials, impose significant challenges<sup>10</sup>. The development of PCPs and their AM technologies<sup>11</sup> has ushered into a new era for technical ceramics, enabling accurate and rapid prototyping via bottom-up 3D printing<sup>12</sup>.

Additive manufacturing, or 3D printing, represents a transformative approach to composite ceramics fabrication, offering design freedom, rapid prototyping, and reduced waste<sup>22,23</sup>. The most prevalent 3D printing techniques for composite ceramics include selective laser sintering (SLS), binder jetting, extrusion-based printing, and SLA<sup>24,25</sup>. Among these, SLA

is particularly promising for fabricating intricate composite ceramics parts with high fidelity and accuracy<sup>26</sup>. Its relatively simple setup and less stringent environmental requirements further enhance its popularity in PDC 3D printing.

The typical vat photopolymerization process for 3D printing composite ceramics comprises three key steps: resin formulation, 3D printing, and pyrolysis/post-processing<sup>13,14</sup>. The resin formulation involves combining functionalized PCPs, crosslinkers, light absorbers, inhibitors, initiators, and ceramic fillers<sup>15,16</sup>. In the 3D printing step, the resin is transferred to SLA or digital light processing (DLP) printers<sup>17</sup>, where ultraviolet (UV) light is used to solidify the resins, creating a well-defined pattern selectively<sup>18</sup>. Sequential layer-by-layer deposition enables the construction of 3D structures. The final post-processing step aims to achieve the desired structural integrity and mechanical performance<sup>19</sup>. Two primary approaches exist for obtaining dense composite ceramics parts – if only particulate fillers are desired, the as-printed part undergoes debinding to remove non-ceramic-forming polymers, followed by backfilling with PDCs for densification and strengthening; alternatively, if the polymeric binders are desired, the entire printed resin structure undergoes pyrolysis<sup>20</sup>. During pyrolysis, active fillers promote ceramic formation and sintering<sup>21</sup>, while passive fillers contribute to the final density and strength<sup>18</sup>.

The chemical processes behind the composite ceramics SLA printing process are as critical as the printing process itself. The process involves two primary stages. First, during SLA printing, functionalized PCPs with allyl or vinyl groups undergo crosslinking with smaller molecular weight crosslinkers via free-radical thiol-ene or vinyl polymerization<sup>27,28</sup>. Once the polymer reaches the gelation point and achieves sufficient crosslinking density, subsequent

layers can be deposited<sup>28</sup>. Second, during pyrolysis, the polymer-to-ceramic transformation occurs through a series of stages, including post-curing, polymeric decomposition, pyrolysis, and crystallization<sup>29,30</sup>. A thorough understanding of these stages is essential for optimizing composite ceramics 3D printing, leading to improved properties and enhanced energy efficiency<sup>31</sup>.

# 1.2. Significance of this research

The prevailing body of current research on PDC 3D printing predominantly utilizes UV light for polymerizing functional polymers<sup>32</sup>. This reliance on UV-based free-radical polymerization significantly restricts the composition of printable resins. Specifically, the SLA process is constrained by the kinetics of UV polymerization, the content, type, and shape of particulate fillers, and the overall polymerization chemistry<sup>33,34</sup>. Moreover, high-intensity UV light can accelerate polymer degradation, leading to defects in the green body<sup>35</sup>. A critical challenge arises when fabricating high-performance SiC-based ceramics, as high loadings of submicron SiC or Si particles scatter and absorb UV light, preventing adequate penetration and polymerization<sup>36,37</sup>. Consequently, a novel printing process is imperative to overcome these limitations and enable the production of high-performance SiC-based ceramic composite.

This dissertation aims to advance 3D printing technology and material development for technical ceramics. Specifically, it addresses the aforementioned challenges by exploring and developing a novel thermal SLA printing technique. Furthermore, a comprehensive understanding of the PCP pyrolysis process is crucial, as the polymer-to-ceramic transformation is a complex thermodynamic and kinetic process. Precise temperature and time control are essential for obtaining composite ceramics with the desired compositions and structures.

- The current research objective aims to address five major issues in printing PDCs:
- (1) Chapter 3: The difficulties in utilizing UV light in printing highly ceramic-loaded PCPs during SLA and DLP have limited the fabrication of high-performance composite ceramics. The current research proposes to solve this issue by proposing a completely different SLA printing technology thermal SLA printing, where NIR laser is employed to create features from a resin pool.
- (2) Chapter 4: This chapter expands the application of thermal SLA to fabricate 3D objects and lattice structures. Furthermore, to address the challenge of weak and unstable porous bodies resulting from debinding prior to PIP, a supporting structure is incorporated during the debinding process to maintain the structural integrity of the parts. Through these advancements, 2.5D printed composite ceramics with enhanced properties are achieved.
- (3) Chapter 5: Silicon nanoparticles as active fillers are introduced into the PCPs resin compositions instead of passive fillers in the previous chapters. The active fillers will facilitate reaction bonding in the sample during pyrolysis. As a result, highly crystalline carbon-free Composite ceramics are obtained in current research, where the highest mechanical performance and resolution in 3D-printed composite ceramics are demonstrated.
- (4) Chapter 6: While a plethora of current literature has revealed the structure properties of PDCs along with their polymer-to-ceramics transition behaviors, little is known about how the *in-situ* reaction takes place throughout the pyrolysis procedure and how fast the polymer-to-ceramics transition is occurring. This chapter focuses on exploring the *in-situ*

- characterization of the polymer-to-ceramics transition process and the kinetics behind ceramics formation, detailing every step in PCPs, from polymers to crystalline ceramics.
- (5) Chapter 7: Although thermal SLA can easily access a broader range of materials, printing resolution is a major drawback. Thermal diffusion into the surrounding area is the major issue limiting the resolution of thermal SLA. This chapter focuses on developing an analytical model to analyze the factors affecting thermal SLA resolution, and the results are also applied to experiments. Moreover, through collaborative work with 3DCeram, Sinto, a sub-100 μm level of resolution was obtained with thermal SLA.

#### **CHAPTER 2: LITERATURE REVIEW**

# 2.1. Polymer-derived ceramics

# 2.1.1. Definition and advantages

PDCs represent a revolutionary class of crossover materials bridging the gap between the processability of polymers and the high-temperature performance of ceramics<sup>35,38</sup>. Unlike traditional ceramics produced through high-temperature sintering of powders, PDCs are synthesized via the controlled thermal decomposition (pyrolysis) of PCPs in inert atmospheres (typically nitrogen or argon)<sup>39</sup>. This unique approach offers significant advantages in terms of processing, microstructure control, and ultimately, material properties<sup>40</sup>.

PCPs are inorganic or organometallic polymers featuring backbones composed of elements such as silicon, boron, carbon, and nitrogen<sup>40,41</sup>. Notably, these polymers possess reactive side-chains (e.g., vinyl, allyl, or hydride groups) that facilitate the polymerization reactions, such as hydrosilylation or free-radical polyaddition<sup>42</sup>. This crosslinking step is essential for creating a self-supporting, rigid, three-dimensional network prior to pyrolysis, enabling shape retention during the transformation from polymer to ceramic<sup>43</sup>. The inherent flexibility of PCPs before crosslinking allows for the application of diverse shaping techniques, including casting, molding, fiber drawing<sup>44</sup>, and, crucially, additive manufacturing<sup>45</sup>.

The pyrolysis process converts the crosslinked PCPs into an inorganic ceramic material<sup>46,47</sup>. During pyrolysis, hydrogen and organic side chains are eliminated as volatile byproducts, and the remaining inorganic framework undergoes further condensation and rearrangement, leading to the formation of either amorphous or crystalline ceramic structures<sup>47</sup>, or often a combination of both (a composite ceramic). This contrasts sharply with traditional

ceramic processing, which relies on the sintering of particulate matter under extreme conditions, often requiring high pressures and prolonged sintering time at temperatures ranging from 1500°C to over 2200°C<sup>48</sup>. Such conditions demand significant energy input and specialized equipment, which is hard to obtain in a laboratory or small factory setting.

The advantages of the PDC route over traditional sintering are multifaceted. The pyrolysis of PCPs typically occurs at temperatures between 800°C and 1500°C<sup>49</sup>, significantly reducing energy consumption and enabling the use of less specialized equipment. The ability to shape the precursor polymer before pyrolysis minimizes or eliminates the need for extensive machining of the final ceramic component, reducing material waste and manufacturing costs<sup>42</sup>, enabling near-net-shape forming, and reducing cracking or damaging the samples during topdown machining<sup>50</sup>. Furthermore, the chemical composition and molecular architecture of the PCPs directly influence the compositions, phase distributions, and microstructures of the resulting PDCs<sup>40</sup>. This allows for precise tailoring of properties such as strength, hardness, toughness, thermal stability, and oxidation resistance<sup>40</sup>. Specifically, the presence of amorphous phases, like SiOC or SiCN, within the PDC structure can significantly enhance toughness and oxidation resistance compared to fully crystalline, conventionally sintered ceramics<sup>51</sup>. The amorphous regions can absorb energy during crack propagation, while crystalline domains may deflect cracks, further increasing energy absorption. This composite nature of many PDCs, often incorporating both amorphous and crystalline phases, leads to improved fracture toughness<sup>51</sup>. Furthermore, amorphous ceramic phases, such as SiOC and SiCN, also exhibit superior oxidation resistance compared to their crystalline counterparts<sup>52</sup>. This is because amorphous ceramics have multiple grain boundaries and carbon nanodomains that separate phases apart

from each other; these boundaries largely slow down the diffusion process and effectively protect the ceramics from oxidation<sup>53</sup>.

Several classes of PCPs are commonly employed, each leading to distinct ceramic compositions. Polysilanes feature a silicon-silicon backbone and are excellent precursors for SiC, particularly when stoichiometric control is desired<sup>54</sup>. Polycarbosilanes are arguably the most versatile class of PCPs, offering high SiC yields, excellent processability, and good thermal stability, in addition to their commercial availability<sup>54</sup>. Their structures, including the nature of the side-chain functionalities, can be tailored to provide a wide range of compositional and microstructural controls for different applications. Polysilazanes are precursors for Si<sub>3</sub>N<sub>4</sub> and SiCN-based ceramics. They are particularly well-suited for the fabrication of thin films and coatings due to their exceptional oxidation resistance and low viscosity in the polymer form<sup>55</sup>. Polysiloxanes (silicones), characterized by a silicon-oxygen backbone, transform into SiOC upon pyrolysis<sup>54</sup>. SiOC exhibits excellent high-temperature stability and fracture toughness.

The selection of a specific PCP is a critical decision that dictates the subsequent processing steps and the properties of the final ceramic<sup>54</sup>. The physical and chemical characteristics of the PCP, such as viscosity, reactivity, and thermal decomposition behavior, influence the choice of shaping and processing techniques<sup>56</sup>. For instance, low-viscosity polysilazanes are well-suited for AM techniques like DLP due to their facile flowability and rapid photopolymerization<sup>57</sup>. The PCP's chemical structure directly determines the final PDC composition. Variations in stoichiometry, crosslinking density, and molecular weight influence pyrolysis behavior and the resulting ceramic phase assemblage<sup>58</sup>. The presence and nature of side chains on the PCP backbone directly impact the formation and content of graphitic carbon

domains within the PDC, further influencing its properties. For example, hydrocarbon side groups like phenyl, benzyl, and allyl are notoriously good at turning graphitic carbon into graphitic carbon in ceramics after pyrolysis<sup>59</sup>.

# 2.1.2. Polymer-to-ceramic conversion

The polymer-to-ceramic conversion process during pyrolysis is a complex, multi-stage transformation encompassing polymerization, decomposition, gas evolution, structural rearrangement, and crystallization. As generally outlined in Figure 2.1, this process is critical for achieving dense, high-performance ceramic materials from polymer precursors.

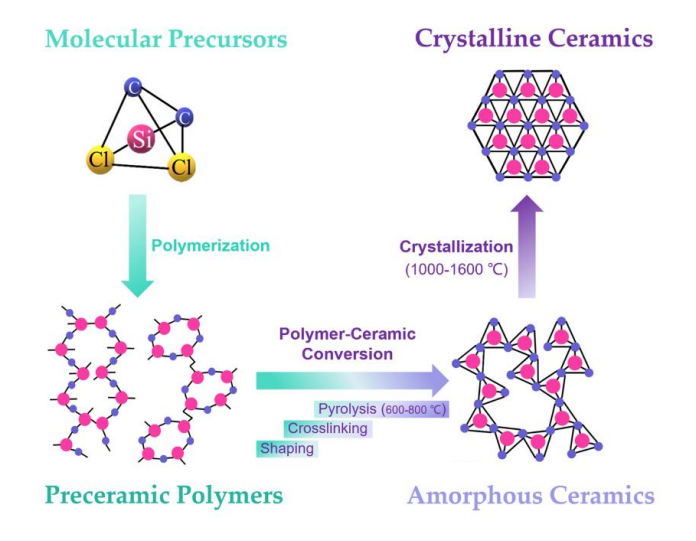


Figure 2.1. Thermal decomposition of different PCPs and their products. 60

Initially, the thermal treatment of PCPs induces shaping and crosslinking, establishing the near-net shape and enhancing the printed structures' green strength and crosslinking density. This initial stage is crucial for preserving the desired geometry prior to the subsequent high-temperature processing<sup>61</sup>.

Following shaping and crosslinking, the PCPs undergo a rapid decomposition phase characterized by the elimination of volatile organic moieties such as hydrogen, vinyl, phenyl,

silanol, and hydrides. This decomposition is accompanied by significant gas evolution within the polymeric matrix, such as CO<sub>2</sub>.<sup>62</sup> To mitigate structural damage caused by rapid gas release and oxidation, this stage is typically conducted in an inert atmosphere within a controlled furnace<sup>63</sup> (e.g., a tube furnace) using very slow heating rates (<1 °C/min). The heating rate is a critical parameter, as it directly influences the rate of thermal energy transfer to the sample's core and, consequently, the kinetics of gas evolution<sup>64</sup>. Slow heating rates facilitate controlled and more homogeneous gas release, minimizing defects' formation and preserving the samples' structural integrity. Notably, PCPs experience substantial shrinkage (up to 60 % <sup>65</sup>) during this phase, highlighting the importance of controlled gas evolution to prevent cracking and deformation <sup>65</sup>.

As the temperature increases, the decomposition process continues, albeit with a reduced rate of gaseous species evolution, as most organic species are burnt off at this stage. Instead, graphitic carbon begins to form and aggregate into nanodomains within the material<sup>59</sup>. Simultaneously, the polymer backbone transforms into amorphous ceramic phases, such as SiOC or SiCN<sup>66,67</sup>. These amorphous ceramics exhibit excellent thermal stability and shock resistance. The formation of nanodomains, where amorphous ceramic regions are interspersed with carbon clusters, creates a unique microstructure that impedes atomic diffusion across domain boundaries<sup>59,68</sup>. This microstructural feature contributes to the enhanced thermal stability of the material, enabling it to withstand temperatures up to 1500 °C with minimal structural or compositional changes<sup>68</sup>.

Beyond 1500 °C, the amorphous ceramic phases undergo crystallization, where this stage involves the nucleation and growth of crystalline phases within the amorphous matrix<sup>69–71</sup>. Sintering mechanisms facilitate interparticle bonding as crystals grow and impinge upon each

other. During a typical sintering process, the contacting crystals first form necks, which then grow into bridges. Finally, the ceramic material densifies with sufficient mass transport, resulting in a compact, consolidated structure. While sintering is effective for densification and strengthening, it is an energy-intensive process requiring specialized high-temperature furnaces and precise control of the thermal environment<sup>72</sup>. Consequently, alternative densification techniques, particularly those compatible with PDCs, are being investigated to enhance efficiency and reduce energy consumption<sup>73</sup>.

# 2.1.3. Post-processing and densification

Achieving high-density PDCs often necessitates post-processing techniques to mitigate pyrolysis's inherent shrinkage and porosity. The significant density difference between polymers (typically ~ 1 g/cm³) and ceramics (often > 3 g/cm³) leads to substantial volumetric shrinkage during the polymer-to-ceramic transition<sup>73</sup>. This shrinkage is further exacerbated by the continuous evolution of gaseous species from the sample's interior. Pressurized heating methods, such as spark plasma sintering (SPS)<sup>74</sup> and hot isostatic pressing (HIP)<sup>75</sup>, are effective strategies for densification during pyrolysis. Applying external pressure and, in the case of HIP, isostatic pressure during pyrolysis effectively counteracts these challenges, promoting densification and minimizing porosity. However, these techniques are associated with higher energy consumption and require specialized, high-temperature equipment, which can limit their widespread applicability<sup>74,75</sup>.

Alternative densification techniques, including melt infiltration (MI)<sup>76</sup>, polymer infiltration and pyrolysis (PIP)<sup>77</sup>, liquid silicon infiltration (LSI)<sup>78</sup>, and chemical vapor infiltration (CVI)<sup>79</sup>, offer effective means of densifying porous ceramic structures. As previously

discussed, PCPs undergo significant shrinkage during pyrolysis, while passive fillers within the resin remain dimensionally stable. This disparity results in the formation of pores and voids within the pyrolyzed structure. To achieve optimal density and mechanical strength, it is crucial to fill these pores with additional material<sup>78</sup>.

Methods like MI and LSI directly backfill the porous pyrolyzed structures by introducing liquid metal or silicon into the pores<sup>76,78</sup>. A vacuum is typically applied to facilitate infiltration, ensuring complete filling of the interconnected porosity. Similarly, PIP involves infiltrating the porous ceramic body with liquid PCPs, which are subsequently converted to PDCs through further pyrolysis cycles. Repeated PIP cycles lead to progressive densification and enhanced mechanical properties<sup>78</sup>.

In contrast to liquid-based infiltration techniques, CVI utilizes gaseous precursors to infiltrate the porous structure<sup>79</sup>. This approach effectively overcomes the limitations imposed by capillary forces, which can hinder liquid infiltration into fine pores with small diameters<sup>79</sup>. By employing gaseous species, CVI enables uniform deposition of ceramic material throughout the porous network, resulting in high-density, homogeneous PDCs<sup>79</sup>.

# 2.1.4. Applications

PDCs possess a unique combination of chemical and physical properties that render them exceptional high-performance materials<sup>73</sup>. Their tunable electrical properties, achievable through the incorporation of conductive fillers, expand their utility in electronic applications.

Furthermore, recent studies have demonstrated ultra-high piezoresistivity in PDCs such as SiCN and SiOC, with piezoresistive coefficients ranging from 1000 to 4000<sup>73</sup>. This remarkable sensitivity to mechanical stress and their adjustable electrical conductivity position PDCs as

promising candidates for high-temperature applications, including microelectromechanical systems (MEMS) and battery electrodes<sup>73</sup>.

The mechanical performance of PDCs, characterized by their high strength, toughness, hardness, and high-temperature stability, constitutes their most significant attribute. Historically, PCPs have served as precursors for the fabrication of ceramic fibers exhibiting extraordinary mechanical properties<sup>80</sup>. Ceramic fibers like SiBCN, SiC, SiOC, and BN, among others, reported in the literature demonstrating elastic moduli up to 400 GPa<sup>81</sup>. The inherent high hardness and strength of PDCs also make them ideal for coating and structural applications<sup>80</sup>. They can be fabricated into complex shapes or deposited onto various substrates, providing robust protection against scratching, weathering, corrosion, and wear<sup>80</sup>.

The combination of PDCs with various ceramic fillers, including fibers and particles, leads to the formation of composite ceramics<sup>9</sup>. These composite ceramics leverage the inherent flexibility of the PDCs and the superior performance of the ceramic reinforcement, resulting in materials with enhanced mechanical properties and stability. This tailored approach allows for the development of advanced materials capable of withstanding extreme operating conditions. Their exceptional high-temperature performance further extends their applicability to demanding sectors such as aerospace, automotive, and energy<sup>9,82,83</sup>.

#### 2.2 AM of ceramics

#### 2.2.1. Overview of ceramics AM

The advent of PCPs has significantly advanced the field of ceramic AM, enabling the fabrication of complex ceramic structures with tailored compositions and architectures<sup>84</sup>. AM technologies, also known as 3D printing, offer unparalleled design freedom and the ability to

produce near-net-shape components, effectively bridging the gap between the design flexibility of polymers and the high-performance characteristics of ceramics<sup>18,85</sup>.

A variety of PCP-based ceramic resin formulations and AM techniques have been developed to meet the diverse requirements of various applications<sup>86</sup>. These AM methods include extrusion-based printing, vat photopolymerization, material jetting, and selective laser sintering (SLS). While all these techniques utilize a layer-by-layer fabrication approach, they differ significantly in their material deposition fashions and solidification mechanisms<sup>12</sup>.

Extrusion-based AM involves the deposition of high-viscosity polymeric precursors in a controlled manner to build 3D structures. The resins employed in this technique can be either thermoplastic, which undergo reversible viscosity transitions upon heating and cooling<sup>87</sup>; or thermoset, which undergoes irreversible curing reactions after extrusion. Thermoset resins typically possess high viscosity to maintain structural integrity during deposition so that they can retain the shape for the post-curing process<sup>88</sup>.

Material jetting utilizes inkjet technology to deposit liquid precursors or binders selectively onto a powder bed. In this process, liquid droplets of PCPs are dispensed onto the ceramic powder bed through inkjet nozzles. Sequential deposition of powder layers and liquid precursors enables the construction of 3D structures<sup>50</sup>.

Vat photopolymerization, encompassing techniques such as SLA, DLP, and masked stereolithography (MSLA), currently represents a prominent AM approach for ceramics<sup>89,90</sup>. These techniques rely on the free-radical polymerization of resin components within a vat. In SLA, a galvanometric system consisting of a set of mirrors directs a focused laser beam across the resin surface to selectively solidify the material, forming 2D patterns<sup>26,60</sup>. While SLA offers

high precision, its point-by-point scanning approach can be time-consuming. MSLA addresses this limitation by employing an array of light sources and a liquid crystal display (LCD) screen as a mask to project entire 2D layers onto the resin surface, significantly accelerating the fabrication process. 60,91 DLP utilizes a micromirror device (DMD) to project light patterns from the source onto the resin vat. DMDs can handle higher energy densities than LCDs, making DLP particularly well-suited for processing particle-filled resins, which require greater penetration depths. 92 Figure 2.2 lists a typical AM process for PCPs, which shows that liquid polymer reins are crosslinked through different AM technologies to achieve their final shape and structure.

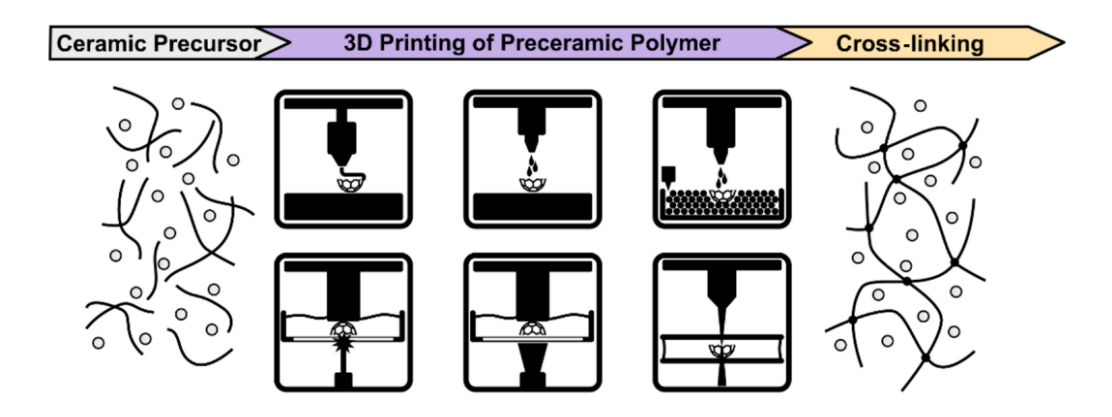


Figure 2.2. AM of PDCs<sup>92</sup>

#### 2.2.2. SLA for PDCs

SLA has emerged as a particularly well-suited AM technique for the fabrication of PDCs among all the methods mentioned in section 2.2.1, primarily due to its high precision and ability to produce near-net-shape components with exceptional accuracy and fidelity<sup>61,93</sup>. Vinyl-terminated and thiol-terminated resins are widely employed in ceramic-based SLA formulations<sup>94</sup>. While both vinyl-vinyl photopolymerization and thiol-ene click chemistry proceed via free-radical mechanisms, thiol-ene reactions offer distinct advantages. The stepwise nature of thiol-ene click chemistry minimizes chain transfer and side reactions, leading to

improved control over the polymerization process. Furthermore, thiols tend to react with oxygen, reducing oxygen inhibition and accelerating the curing and printing processes <sup>94–96</sup>.

A typical SLA resin formulation for PDC comprises several key components in addition to the basic PCPs. Multifunctional crosslinkers, either thiol-terminated or vinyl-terminated, facilitate network formation <sup>96</sup>. Reactive and non-reactive diluents, including monofunctional or non-functional species, are incorporated to reduce resin viscosity, thereby enhancing flow and recoating during the SLA process. Light absorbers, such as carbon black and Sudan dyes, absorb incident UV radiation and transfer the absorbed energy to the monomers, initiating crosslinking. Photoinitiators and inhibitors are crucial for initiation and controlling the rate of polymerization. Inhibitors, such as benzophenones, effectively scavenge free radicals, extending the shelf life of the resin <sup>35,94</sup>.

For the SLA type of printing, Jacob's equation (eq. 2.1) is usually considered the golden rule for conducting the printing<sup>97</sup>, where a working curve curing depth versus energy dosage can be plotted to guide the SLA process.

$$C_{d} = D_{p} \times \ln\left(\frac{E}{E_{C}}\right) \tag{2.1}$$

Where  $C_d$  stands for the actual curing depth,  $D_p$  denotes how far the light can penetrate through the resin layers, E means energy dosage applied during the printing process, and  $E_c$  is the critical amount of energy for the resin to cure.

# 2.2.3. Challenges in UV-SLA

A fundamental challenge in SLA of particle-filled PCP resins lies in achieving adequate UV light penetration and adequate polymerization. Effective layer formation requires sufficient photon flux to reach a critical depth within the resin, ensuring that the concentration of free

radicals reaches a threshold necessary for polymerization and structural integrity<sup>97</sup>. However, the presence of fillers, which are essential for achieving high ceramic loadings, significantly complicates this process. These fillers scatter and attenuate UV light, impeding its penetration, especially when the RI of these particles is high. Increasing the UV light intensity, while potentially increasing the penetration depth, can exacerbate light scattering, leading to reduced printing resolution rather than enhanced penetration<sup>98,99</sup>. Furthermore, even when sufficient penetration is achieved, the prolonged exposure times required for highly loaded resins render the process impractical for efficient fabrication. While there is no effective method of solving this issue, people have been trying to use limited filler loadings and filler sizes during the SLA process for PCPs<sup>12</sup>.

Shrinkage and warpage pose significant challenges in UV-printed PCP structures. Lower particle loadings, while facilitating light penetration, result in greater dimensional changes during pyrolysis, compromising the dimensional accuracy of the final ceramic part<sup>21</sup>. Moreover, incomplete curing during printing introduces residual stresses within the samples, leading to stress concentrations and potential crack formation. During pyrolysis, the evolution of volatile species from the sample's interior can further exacerbate these issues<sup>21</sup>. In the absence of adequate internal support structures, these gaseous species can induce damage, resulting in cracks and warpages in the pyrolyzed components<sup>21</sup>.

#### 2.3. Characterization of PDCs

Extensive efforts have been dedicated to the *ex-situ* characterization of PDCs to elucidate their structural-property relationship and polymer-to-ceramic transformation mechanisms.

Various analytical techniques, including spectroscopy, X-ray analysis, electron microscopy<sup>73</sup>,

and nuclear magnetic resonance (NMR)<sup>100</sup>, have been employed to characterize PDCs across all pyrolysis stages.

Spectroscopic techniques, such as Fourier-transform infrared spectroscopy (FTIR) and Raman spectroscopy, offer convenient and efficient methods for obtaining structural information from PCPs and PDCs<sup>101</sup>. In FTIR, infrared radiation spanning a range of wavelengths is directed onto the samples. The absorption of specific wavelengths, corresponding to certain molecular vibrational modes, provides insights into the sample's chemical structures<sup>102</sup>. Conversely, Raman spectroscopy utilizes a focused laser beam to induce Stokes scattering, where photons with longer wavelengths are emitted and detected<sup>103</sup>. These techniques are particularly effective for analyzing the vibrational modes of polymers, including functional groups and side chains. Furthermore, Raman spectroscopy is invaluable for characterizing graphitic carbon, specifically the D and G bands, and monitoring the evolution of carbon structures during pyrolysis<sup>104</sup>.

X-ray-based techniques, including X-ray diffraction (XRD), X-ray photoelectron spectroscopy (XPS), and X-ray reflectivity (XRR), provide complementary structural and compositional information. XRD enables the identification of crystalline phases, determination of crystallite sizes, and analysis of crystal structures by detecting constructive interference patterns arising from X-ray scattering. Bragg's law is then used to calculate the crystal structure from the measured patterns<sup>93</sup>. XPS offers a precise method for analyzing materials' elemental composition and chemical environment. Upon irradiation with high-energy X-rays, core-level photoelectrons are emitted and detected under vacuum, providing detailed information about the chemical states of constituent atoms, particularly valuable for characterizing non-stoichiometric ceramics such as SiOC and SiCN<sup>105</sup>. XRR, by analyzing the reflected X-ray intensity at

interfaces, allows for the non-destructive determination of film thickness and density, making it particularly useful for characterizing thin films and coatings<sup>106</sup>.

Electron microscopy techniques provide direct visualization of the morphological and crystalline features of PDCs. Utilizing electrons as probes, these methods offer sub-nanometer spatial resolutions, enabling detailed analysis of microstructure<sup>21</sup>. Scanning electron microscopy (SEM) analyzes backscattered and secondary electrons to reveal morphology, grain boundaries, and the distribution of amorphous and crystalline phases<sup>107</sup>. Energy-dispersive X-ray spectroscopy (EDS), coupled with SEM, provides elemental composition and mapping, elucidating the homogeneity and elemental distribution within the ceramic. Transmission electron microscopy (TEM), by analyzing transmitted electrons, allows for the characterization of nanodomains and nanocrystalline structures<sup>59</sup>, revealing features such as nanosized turbostratic carbon networks surrounding SiC/Si<sub>3</sub>N<sub>4</sub> nanodomains<sup>59</sup>.

Numerous other characterization techniques contribute to a comprehensive understanding of the chemical and physical properties of PDCs and PCPs at the sub-nanometer scale<sup>21</sup>. This wealth of information is essential for elucidating the polymer-to-ceramic transformation mechanisms, tailoring PDC properties, and developing advanced materials for diverse applications.

# 2.4. Key findings and research gaps

From the literature review, it can be concluded that PCPs are becoming a popular choice for applications in 3D printing ceramics. Most of the current research has focused on UV-based SLA for fabricating composite ceramics, including SiOC, SiCN, and others<sup>42,108</sup>. These materials have shown promising properties and performances. Extensive research has been undertaken on

*ex-situ* structural characterizations of PCPs and PDCs and their potential applications. While the current research shows that 3D printing PDCs with enhanced properties is very promising, several gaps remain.

- (1) Limited exploration of high-performance ceramics: there is a notable lack of research on fabricating high-performance ceramics, such as SiC, using PCP-based AM techniques.
- (2) Challenges in highly loaded resin printing: significant challenges persist in printing highly loaded resins, particularly those incorporating high RI fillers, hindering the production of dense, high-performance ceramic parts.
- (3) Incomplete understanding of the polymer-to-ceramic transformation: a more detailed understanding of this process is required to optimize processing parameters and tailor the properties of PDCs.
- (4) Difficulties in achieving highly crystalline and carbon-free PDCs: gaps exist in developing strategies for producing these desirable materials for specific high-temperature applications.

This thesis will attempt to close some of these gaps in knowledge and described in the later chapters.

# CHAPTER 3: THERMAL SLA OF SIC-LOADED ACRYLATE RESINS WITH PDC INFILTRATION

Parts of this work are adapted from: ACS Appl. Eng. Mater. 2025, https://doi.org/10.1021/acsaenm.5c00054. This is the version of the article after peer review or editing as submitted by the authors for publication. The publisher is not responsible for any errors or omissions in this version of the manuscript or any version derived from it.

#### 3.1 Abstract

The implementation of SLA for fabricating 3D-structured PDCs has greatly improved the resolution, manufacturing potential, and capability to produce complicated component geometries in ceramic materials. However, different material systems impose challenges to the traditional UV SLA photocrosslinking process due to a narrow window of material selection requirements – UV transparency, UV degradation resistance, ability to support the photoinduced radical curing mechanism, and ambient shelf-life stability. Herein, a NIR thermal SLA printing technology is demonstrated on a composite thermally-curable acrylate-based highly loaded resin to overcome current issues with UV light-driven SLA additive manufacturing of PCPs. For this thermal SLA crosslinking method without UV photopolymerization, a high-intensity NIR laser  $(\lambda = 808 \text{ nm})$  was used to generate localized thermal heating at the resin pool interface, which led to rapid, targeted thermal free-radical polymerization and solidification of the SiC particleladen acrylate-based resin during laser scanning. Thermally cured printed parts were demonstrated using a gantry-based movement platform and a resin pool in a top-down laser scanning configuration. After printing, the green bodies were debinded, followed by PIP during post-processing, which enhanced the mechanical strength of the pyrolyzed samples. This work

demonstrated the fabrication of a reinforced PDC composite material with crystalline SiC fillers and an amorphous matrix made of SiOC and SiCN. The flexural strength of the NIR-printed samples reached 48 MPa with a fracture toughness of 4 MPa·m<sup>1/2</sup>.

#### 3.2 Introduction

The low density, thermal resistance, and high-strength properties of SiC have attracted attention from aerospace, turbine, and electronic applications<sup>109</sup>. However, as an abrasive material, SiC is difficult to machine into high-fidelity structures with complicated shapes.

Therefore, new methods using novel processing techniques are needed for shaping SiC and related carbides<sup>109</sup>. As an emerging method for fabricating complex, 3D structures, AM has been adapted to many materials, namely polymers, metals, composites, and ceramics<sup>89</sup>. PDCs stand out as excellent candidates for AM due to the potential to shape components in an easy-to-process polymeric form before ceramic conversion<sup>60</sup>, which has been demonstrated in several examples<sup>108</sup>.

PCPs such as polysilazanes and polycarbosilanes are promising targets for 3D printing as their pyrolysis yields SiCN<sup>110</sup> and SiOC<sup>101</sup> materials with excellent mechanical properties and high ceramic yield. As demonstrated by Wang et al.<sup>95</sup>, AM methods such as SLA can be applied to the rapid fabrication of SiOC 3D structures through free-radical crosslinking and solidification, including thiol-ene crosslinking of PCPs. Ceramic materials such as SiCN<sup>110</sup>, SiC<sup>111</sup>, and PDC composites<sup>86</sup> have been fabricated through SLA. Additionally, PCP resins can also be formulated with ceramic particles to improve the overall performance of the materials and increase the ceramic yield during processing<sup>11</sup>.

PCPs are usually processed thermally in conventional manufacturing, and these thermal processes have been adapted to suit various AM methods. There are three major conventional 3D printing methods for PCPs: material extrusion, laser powder bed fusion, and sheet lamination. Direct ink writing (DIW) and fused filament fabrication (FFF) are examples of material extrusion-type printing. For DIW, heat is applied upon extrusion of the material from a nozzle to crosslink the PCP and solidify the printed structure. Kemp et al. 112 designed a composite ink with boron nitride particles and PCP, which cures at elevated temperatures with the help of thermal initiators. Gorjan et al. 113 proposed a printing method where PCP combined with plasticizer and ceramic fillers are used as the solid feedstock, which will melt upon heating, and the extruded filament will solidify upon cooling, mimicking typical polymer-based FFF. Selective laser curing (SLC) is an example of laser powder bed fusion, a process very similar to SLS of polymers and metals. Friedel et al. 114 showed that with constant recoating of the feed material, a CO<sub>2</sub> laser can melt the PCP. It also demonstrated the printing of a 3D structure from a PCP powder bed composed of a mixture of PCP and SiC particles. Laminated object manufacturing (LOM) is an example of sheet lamination PCP printing. Sieber et al. 115 demonstrated a LOM process for PCP processing, where paper sheets infiltrated with PCP are stacked together with hot pressing to fuse the structure.

There have been several previous reports on the SLA of PCPs<sup>60,116</sup>. However, the majority of the work has emphasized UV-based SLA<sup>97</sup> and DLP<sup>97</sup>, since acrylate-based photoresins rapidly cure under UV light irradiation<sup>95</sup>, which gives high-resolution and structural flexibility<sup>117</sup> of the samples. A higher solid content of crystalline ceramic particles is desired in PCP formulations<sup>28</sup>, as these fillers reduce the overall shrinkage during pyrolysis, preserve the

structural integrity of the samples<sup>117</sup>, increase ceramic yield<sup>108</sup>, and strengthen the final parts<sup>86</sup>. Thermal SLA, as proposed here, solves many issues encountered in UV-based photocrosslinking SLA printing, where a much wider selection of polymers and curing mechanisms are available for printing, and the particle content in the printing ink can be much higher than 20 wt% (upper limit of many UV-printing techniques)<sup>86</sup>, which ensures high crystallinity and high-density ceramic parts after pyrolysis. Thermal printing decreases the need for post-processing of the samples, where the samples are strong enough to undergo a direct debinding or pyrolysis process. Additionally, the pot life of thermal resin can be much longer than that of traditional UV resins<sup>109</sup>, and no light inhibitors are needed. Due to the intrinsic limitations of UV printing<sup>111,118,119</sup>, several studies have already been conducted on converting IR laser into UV light with up-conversion nanoparticles and IR initiators<sup>120</sup> in SLA processing. These prior reports demonstrate the usefulness of NIR laser thermal curing over UV curing, including higher penetration depth and less structural damage<sup>121</sup>.

Laser-based technology has attracted much attention in materials processing, including processes like stereolithography, cutting, localized heating, and probing <sup>122</sup>. The earliest use of thermal laser-assisted 3D printing of polymers was in 1994<sup>21</sup>, when a high-intensity 10.6 μm CO<sub>2</sub> laser was used for 3D printing of a ring structure with silica-filled epoxy and polyester. High temperatures (200 - 280 °C) are often associated with CO<sub>2</sub> laser excitation, which leads to burning and distortion of the printed structure <sup>123</sup>. After the debut of AM with IR laser excitation, researchers continued to tune IR laser-based processes in making well-defined 3D structures using powder bed fusion-based processing to avoid overheating the materials, controlling heat diffusion and object resolution, and monitoring the high-temperature process. Fu<sup>124</sup> compared a

visible 532 nm laser with a 10.6 μm CO<sub>2</sub> laser, which was used in curing thermal-initiated resins, where it was discovered that both UV and IR wavelengths can cause structural damage by electronic and vibrational excitation, respectively. Fortenbaugh et al. <sup>125</sup> extended the application of a 532 nm laser and applied the photothermal <sup>126</sup> effect on silicone hydrosilylation using 100 nm gold nanoparticles. It was observed that light-absorbing fillers like gold nanoparticles promote a massive increase in the curing speed due to the light-to-heat conversion of photothermally active particles. NIR laser excitation, with wavelengths in the range of 750 nm to 1300 nm<sup>127</sup>, stands out as an excellent source of heat as it preserves the polymeric structures without significant chemical damage. <sup>128</sup> More recent work also utilized a NIR laser in direct ink writing of optical silicones <sup>129</sup> and a CO<sub>2</sub> laser for SiC binder jetting <sup>114</sup>, demonstrating laser-based technology's precision and printing capabilities with different printing techniques.

This work reports a novel thermal SLA method for crosslinking highly loaded PCP resins. Thermally-cured, acrylate-based resins with high SiC particle loadings (50 wt%) are demonstrated for various printed structures. The printed polymers were debinded and subjected to PIP to obtain excellent mechanical properties under low pyrolysis temperatures (800 °C). 25,26 The thermal-curing SLA technique offers significant advantages due to its versatile resin composition and particle loading capabilities, allowing various fillers at high volume percentages, provided that the particles absorb sufficient IR light to cure the resin. Additionally, this technology supports a broad range of thermal curing reaction mechanisms, offering greater flexibility compared to UV-based photopolymerization techniques.

# 3.3. Experimental section

#### 3.3.1. Materials

All chemicals (Figure 3.1) were used as received without further purification. Diurethane dimethacrylate (DUDMA), acetone (99.5 %), and dicumyl peroxide (98 %) were purchased from Sigma-Aldrich (St. Louis, MO). Durazane 1800 as the preceramic polymer (PCP) was supplied by Merck KGaA (Darmstadt, Germany), and silicon carbide particles (1  $\mu$ m,  $\beta$ -phase, > 99.5 %) were purchased from Beantown Chemical (Hudson, NH).

Figure 3.1. Chemical structures of (a) DUDMA, (b) dicumyl peroxide, (c) Durazane 1800. 3.3.2. Sample preparation

The preparation of the resin formulation consists of two steps. First, 100 g of DUDMA with an equal mass of SiC particles was transferred into a round-bottom flask, with 1 wt% dicumyl peroxide added as a thermal initiator. Then, 50 mL of acetone was added to the flask, and the mixture was subsequently stirred at 600 RPM for 10 h. Finally, all the solvent was removed with a rotary evaporator, which gave the resin composition (*DUDMA-SiC 50:50*) for subsequent printing. Durazane 1800 was pre-mixed with 1 wt% dicumyl peroxide for the polymer infiltration process, as described in the following sections.

# 3.3.3. NIR thermal SLA printer

For fabrication of the thermal SLA printer, all optics were purchased from Thorlabs Inc. (Newton, NJ), and a Lumics (Berlin, Germany) 808 nm fiber laser was used as the thermal laser source for printing. The printer consists of three parts – the NIR laser with an optical cage, the X-Y-Z gantry that controls the laser movement, and a stainless-steel baseplate mesh to support the printed structure, Figure 3.2.

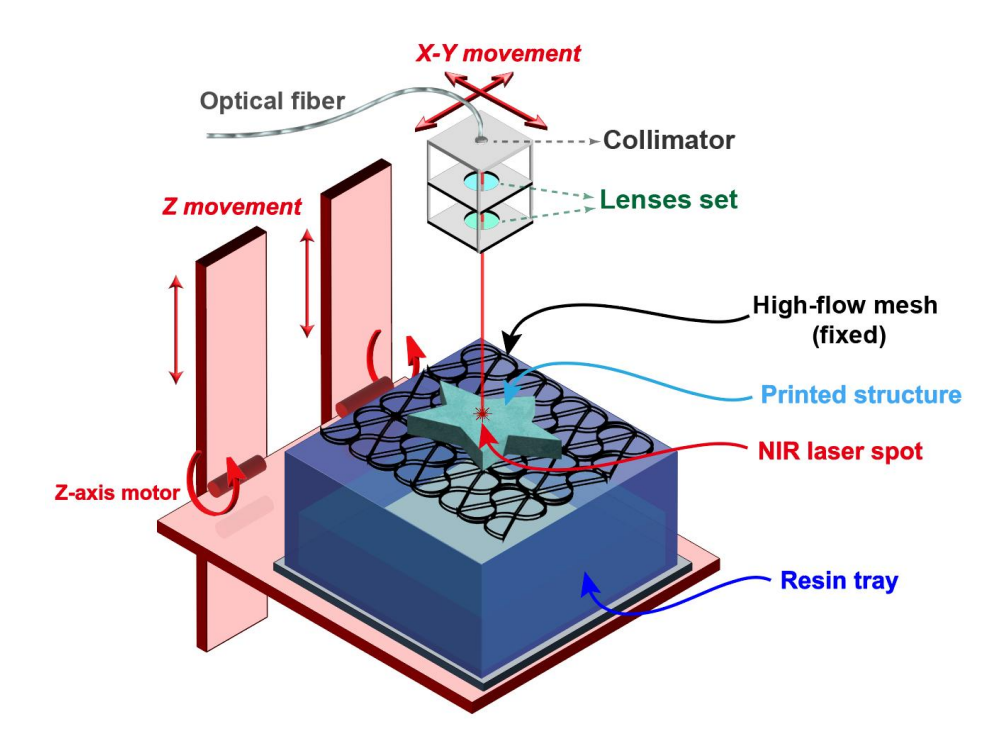


Figure 3.2. Thermal SLA printer schematic for thermal printing of the resin composition DUDMA-SiC 50:50.

An optical fiber was used for the NIR laser to guide the laser generated from the 808 nm diode laser to the printing position. The advantage of using a fiber-coupled laser optic is that the laser module does not need to be attached to the moving print head, thus facilitating top-down SLA printing. The optic fiber was connected to a cage system, where the laser passed through a

collimator and a set of lenses before focusing on the sample surface. More details are illustrated in Figure 3.3.

For the printer and the X-Y-Z gantry movement stage, two motors control the x-y position of the laser to cure the resin at programmed locations. The z-axis movement added new layers to the printed structure, where a fixed stainless-steel mesh supported the printed structure while the resin tray was moved upwards with the z-axis to further immerse the sample in the resin pool. The travel speed of the laser was set to be much faster (250 mm/s) than the printing speed (5 mm/s) to ensure it was not curing the empty area between the printing parts. A thermal camera (FLIR C3-X Compact Thermal Camera, Wilsonville, OR) was fixed onto the setup to monitor the printing temperature, where a temperature range of 140 °C to 160 °C was maintained to avoid both overcuring and undercuring without burning the resin.

The energy density of the laser is given by eq. 3.1:

$$\eta = \frac{P}{D_{\text{PV}}} \tag{3.1}$$

where  $\eta$  is the energy density of the laser beam, P is the power output of the laser, D is the beam's diameter, and  $\nu$  represents the laser beam's scanning speed on the surface of the printing resin.

The laser output was 2.96 W, the diameter of the laser beam was 2.0 mm, and the scanning speed was 5 mm/s. The calculated energy density of the laser beam was 29.6 J/cm<sup>2</sup>.

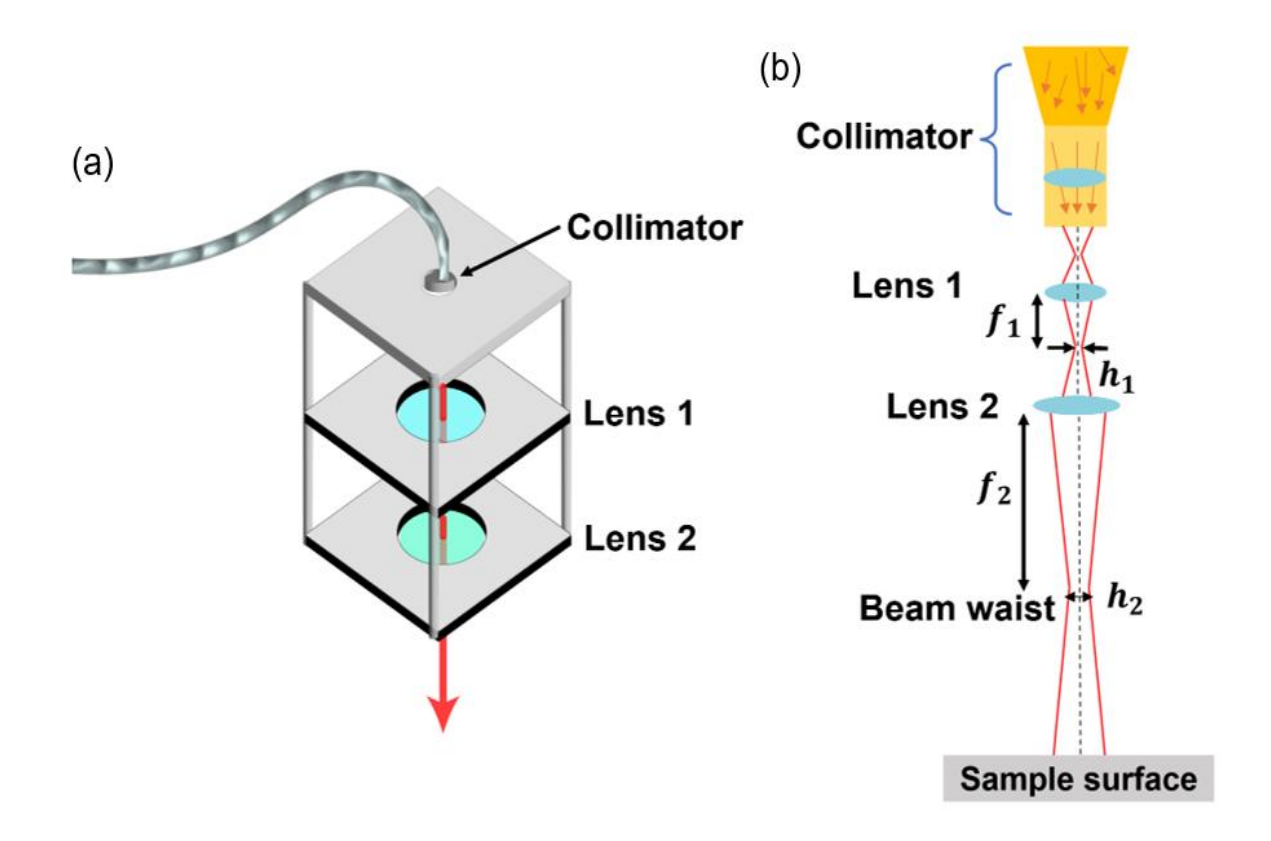


Figure 3.3. (a) Configuration of the optical cage system for NIR thermal SLA printer; (b) diagram of optical beam path through the cage system.

The configuration of the optical cage system for the NIR thermal SLA printer is depicted in Figure 3.3, where three components make up the system – a laser collimator and two lenses. The laser generated from the diode will be randomly scattered in the fiber optic; therefore, a collimator and lenses are needed to collimate and control the beam divergence. The beam expander will change the beam waist diameter (h) and divergence angle. Since a larger beam waist will lead to lower divergence, a set of beam expanders was used to ensure printing accuracy (Figure 3.3). When placing two lenses apart at a distance equal to the sum of their focal lengths, we have eq. 3.2:

$$\frac{f_1}{f_2} = \frac{h_1}{h_2} \tag{3.2}$$

where  $f_1$  and  $f_2$  are the focal lengths of two lenses, respectively, and  $h_1$  and  $h_2$  are the radius of the beam entering and leaving the two lenses, respectively. The beam parameters:  $h_1 = 0.8$  mm,  $h_2 = 3$  mm,  $f_1 = 4$  mm, and  $f_2 = 15$  mm were used to maintain high printing resolution.

3.3.4. Green body formation

Samples with a range of geometries were fabricated with the thermal SLA printer using the *DUDMA-SiC 50:50* resin, and the resulting single-layer green body structures are shown in the photograph in Figure 3.4(a). A schematic of the thermal crosslinking is shown in Figure 3.4(b). To baseline chemical compositions and mechanical properties, oven-cured samples with the same resin composition were fabricated and processed in silicone molds. Oven curing of the samples was performed by heating the resin in a convection oven at 150 °C for 5 min, during which the resin was cured in a 2 cm x 5 cm bar-shaped specimen.

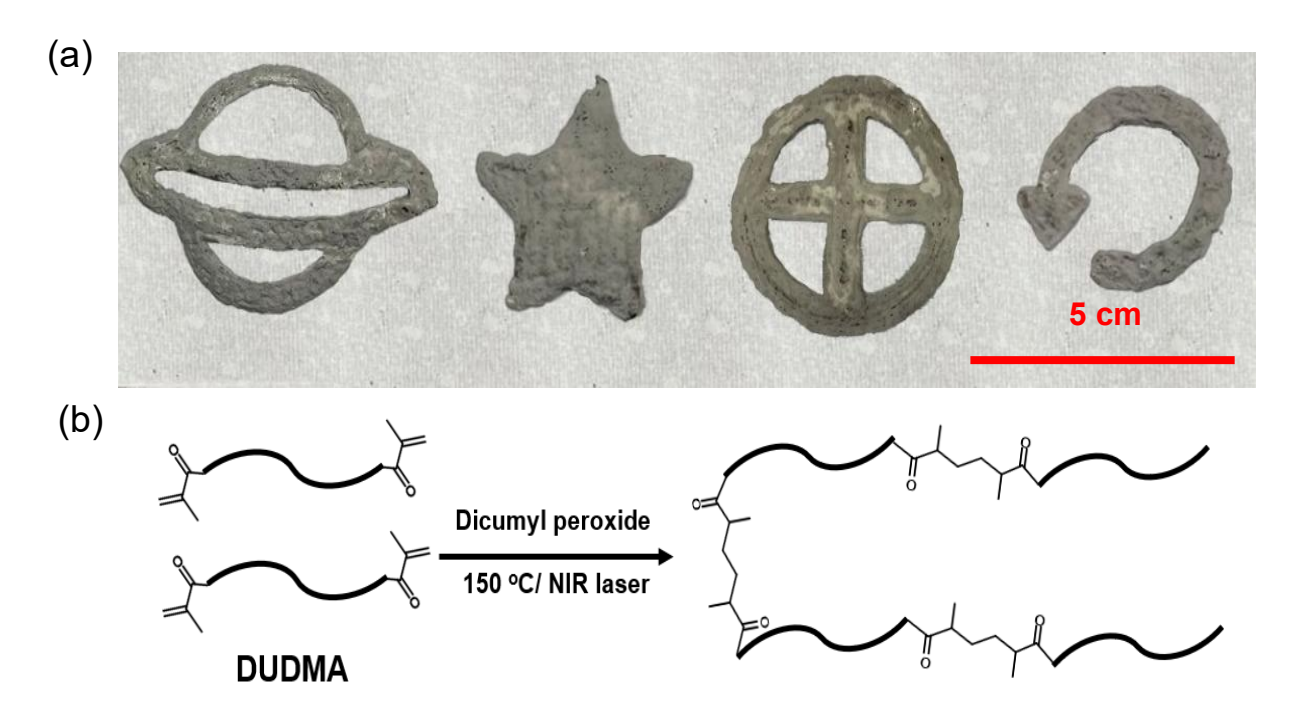


Figure 3.4. (a) Thermal SLA printed green body structures; (b) chemical crosslinking reaction during the thermal SLA printing.

### 3.3.5. PIP

The first step in processing the as-printed green body sample is debinding, during which most of the organics that will not become ceramic are removed. The debinding process removes all the unpolymerized and polymerized acrylate resin from the samples to increase the porosity for PIP. Green body samples were heated in air at 0.4 °C/min to 500 °C in a muffle furnace and held for 1 h to remove all the polymeric species. The sample was then cooled to room temperature at a rate of 0.4 °C/min to yield the green body, a porous scaffold composed mainly of SiC particles.

PIP is a post-processing procedure where PCPs are infiltrated into the pores of the debinded sample to increase the density and structural integrity of the samples once pyrolyzed. Every cycle of PIP consists of three steps – vacuum infiltration with liquid PCP of the debinded structure, curing of the PCPs, and pyrolysis of the PCPs. A higher number of PIP cycles will lead to denser structures with improved mechanical properties, assuming that the porous structure remains open and can be infiltrated with liquid PCP. Durazane 1800 was chosen as the best PCP to fill the porous SiC particle scaffold due to two factors: (1) as a polysilazane, it will yield SiCN and SiOC, which can give excellent mechanical strength 130,131; and (2) the PCP itself is very low viscosity and flows into the porous SiC particulate scaffold easily, making the infiltration process faster and more complete.

The debinded samples were placed on the bottom of the round-bottom flask. Then, a vacuum pump was applied to lower the pressure below 5 kPa. After low pressure was achieved, Durazane 1800 was released dropwise (10 mL/min) onto the samples until they were fully

immersed. The samples were left under vacuum for 20 min to equilibrate before removal from the flask, and another pyrolysis cycle was conducted.

Pyrolysis of the PDC-infiltrated sample turns the PCP into ceramic, obtaining a densified PDC composite. In a typical pyrolysis procedure, the sample was transferred into a tube furnace after polymer infiltration. The sample was heated to 170 °C from room temperature with a ramp rate of 1.2 °C/min to cure the PCP, and then the temperature was increased to 800 °C with a ramp rate of 0.48 °C/min. After dwelling at 800 °C for an hour, the sample was cooled to room temperature with a 1 °C/min cooling rate. During the entire pyrolysis process, argon flow (50 cm³/min, 99.95 % ultra-high purity) was used to maintain an inert environment in the tube furnace.

## 3.3.6. Characterization

FTIR was performed on a Bruker Vertex 70 IR spectrometer (Billerica, MA) equipped with a liquid nitrogen-cooled mid-band mercury cadmium telluride detector. Diamond attenuated total reflection (ATR) was used to analyze the resin and ceramic chemical compositions in the 500 – 2000 cm<sup>-1</sup> range. The deconvolution of the FTIR peaks was performed using Gaussian fitting. For liquid samples, a thin layer was spread onto the crystal for analysis. For solid samples, a flat part of the sample was pressed down against the crystal. For powder samples, a sample press was used to press the powder against the diamond window to ensure good contact for analysis. The crystalline structure of the pyrolyzed samples was characterized by XRD (Malvern Panalytical Empyrean, Malvern, United Kingdom) within a 2θ range of 30° to 75°. The microscopic morphology and elemental distribution of the samples were characterized by SEM (Verios 5 XHR SEM, Waltham, MA). The elemental composition of the samples was measured

with XPS (VersaProbe III, Chanhassen, MN) equipped with a monochromatic Al  $k\alpha$  x-ray source ( $h\nu = 1,486.6 \text{ eV}$ ) and a concentric hemispherical analyzer<sup>132</sup>. The samples were fractured in air immediately prior to being introduced to the vacuum system to examine the cross-section and avoid minimizing any surface oxidation that was present. The density was determined using the Archimedes method. Since PIP does not change the dimensions of the sample<sup>133</sup>, the linear shrinkage of the sample after debinding was calculated by the percent change in length after debinding, given by eq. 3.3:

$$S = \frac{L_0 - L}{L_0} \tag{3.3}$$

where S is the shrinkage of the sample after debinding,  $L_0$  and L stand for the length of the samples before and after debinding, respectively.

The flexural strength was measured using an MTS Criterion 43 (C43.504, Eden Prairie, MN) with an MTS 1kN S-beam load cell in a 3-point bend fixture. Flexural strength  $\sigma$  is given by eq. 3.4 (ASTM C1341-13):

$$\sigma = \frac{3FL}{2bd^2} \tag{3.4}$$

where F is the fracture load, L is the support span length, b and d are the width and thickness of the sample, respectively.

Vickers microindentation (Qness Q60 A+, QATM, Austria) was employed on the polished cross-sections of mounted bar samples. An applied load of 10 kgf (n = 5 per sample) was utilized to measure these ceramic materials' hardness and fracture resistance. The indentation fracture toughness (K<sub>IFR</sub>) was calculated using eq. 3.5 given by Anstis et al. <sup>134,135</sup> and the assumed elastic modulus of silicon carbide (Voigt-Reuss-Hill average, 434 GPa<sup>33</sup>). The crack

lengths were measured using the average of five parallel lines (as described in Quinn's method<sup>136</sup>) for horizontal and vertical diagonals with image analysis software.

Fracture toughness K<sub>IFR</sub> is given by eq. 3.5:<sup>134,135</sup>

$$K_{IFR} = 0.016 \sqrt{\frac{E}{H}} \frac{P}{e^{3/2}}$$
 (3.5)

where E and H is the elastic modulus and hardness of the sample, respectively, P is the peak load, and c is the crack length.

# 3.4. Results and discussion

FTIR analysis was conducted on uncured, oven-cured, and NIR-printed green body samples (Figure 3.5(a, b)) to compare the changes in the chemical composition of the resin between NIR printing and oven-curing methods. Additionally, the chemical composition of pyrolyzed Durazane PCP (Figure 3.5(c)) and debinded green body after PIP was also investigated (Figure 3.5(d)) with FTIR.

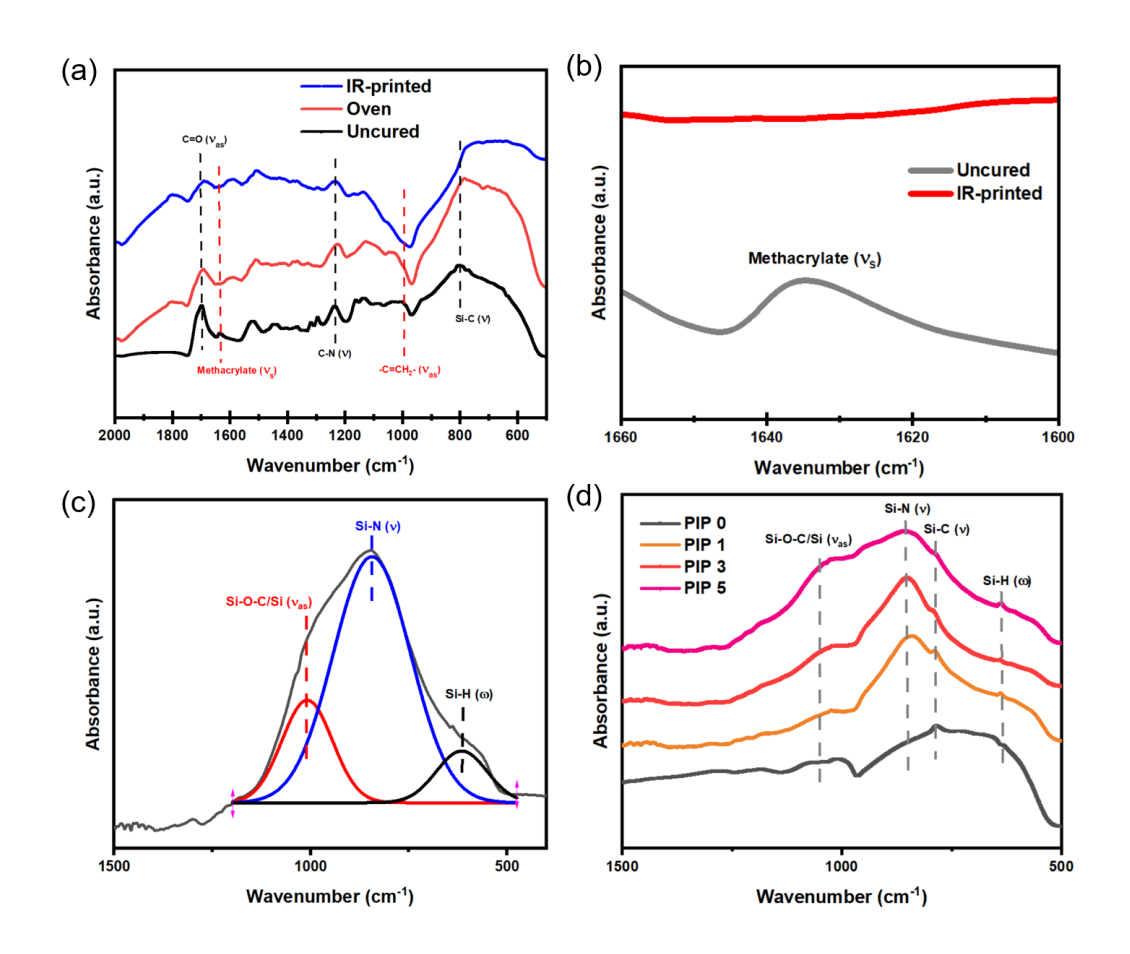


Figure 3.5. (a) FTIR spectrum of NIR-printed, oven-cured, and uncured DUDMA-SiC 50:50 samples; (b) local FTIR spectrum of NIR-printed and uncured DUDMA-SiC 50:50 samples; (c) deconvoluted FTIR spectrum of Durazane pyrolyzed at 800 °C; (d) FTIR spectrum of NIR-printed DUDMA-SiC 50:50 samples after PIP.

From Figures 3.5(a, b), it can be concluded that there are no significant differences in chemical composition between the oven-cured samples and NIR-printed samples in the mid-IR spectral region. The attenuation of the methacrylate symmetric stretching peak  $v_s$  (C=C)<sup>137</sup> at 1635 cm<sup>-1</sup> and the disappearance of the asymmetric stretching band  $v_{as}$  (-C-H) in the -C=CH<sub>2</sub>-moiety<sup>137</sup> at around 994 cm<sup>-1</sup> are evidence of acrylate curing after heat treatment. The FTIR spectrum in Figure 3.5(c) shows the chemical composition of Durazane after pyrolysis at 800 °C,

which is identical to the PIP pyrolysis. The deconvoluted peaks at 1007 cm<sup>-1</sup>, 850 cm<sup>-1</sup>, and 620 cm<sup>-1</sup> correspond to  $v_{as}$  (Si-O-C/Si), v (Si-N), and wagging band  $\omega$  (Si-H) <sup>138</sup>, respectively. Figure 3.5(d) shows the FTIR spectra of PDC composite samples after PIP processing. This data shows the same v (Si-O-C/Si), v (Si-N), and  $\omega$ (Si-H) peaks as the matrix PDC shown in Figure 3.5(c). Moreover, there is evidence of a weak  $v_{as}$  (Si-O-Si)<sup>139</sup> peak at 1090 cm<sup>-1</sup>, and a v (Si-C) peak from 780 - 790 cm<sup>-1</sup>, indicating multiple ceramic components, including SiC, SiCN, SiO<sub>2</sub>, and SiOC in the final PDC composite.

The SiC particle fillers, matrix PDC, and the resulting PDC composites were analyzed with XRD to show the presence of crystalline phases in the materials (Figure 3.6). All pyrolyzed samples were treated under argon (50 cm<sup>3</sup>/min) at 800 °C with the same heating and cooling procedure detailed in the experimental section.

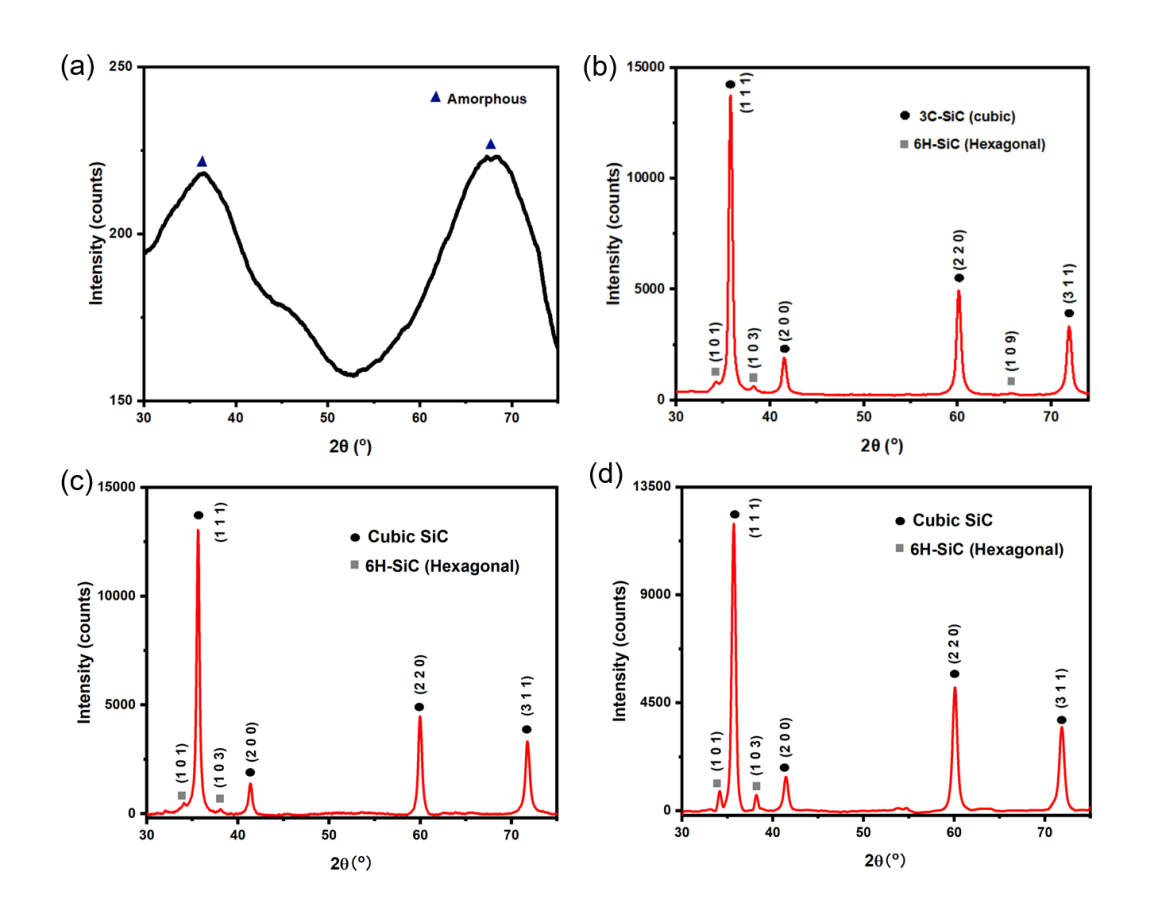


Figure 3.6. XRD patterns of: (a) pyrolyzed Durazane 1800; (b) SiC filler particles; (c) oven-cured sample after 3 cycles of PIP; (d) NIR-printed sample after 3 cycles of PIP.

After pyrolysis of the PDC at 800 °C, two broad peaks at  $2\theta = 33.2^{\circ}$  and  $68.0^{\circ}$  indicate there are only amorphous phases for pyrolyzed Durazane 1800 (Figure 3.6 (a)), where the amorphous halo of these peaks demonstrates the material exists in cubic 3C-SiC phase<sup>55</sup>. For oven-cured (Figure 3.6 (c)) and NIR-printed samples after PIP (Figure 3.6 (d)), the peaks at  $2\theta = 35.8^{\circ}$ ,  $41.5^{\circ}$ ,  $60.1^{\circ}$  and  $71.9^{\circ}$  correspond to crystalline cubic 3C-SiC particles;  $2\theta = 34.3^{\circ}$ ,  $38.3^{\circ}$ ,  $41.6^{\circ}$ ,  $45.4^{\circ}$ ,  $54.7^{\circ}$ ,  $60.1^{\circ}$ ,  $65.8^{\circ}$ ,  $71.9^{\circ}$  and  $73.5^{\circ}$  represent hexagonal 6H-SiC particles<sup>140</sup>. Throughout each PIP cycle, XRD patterns of the NIR-printed and oven-cured samples showed they have the similar composition. Thus, only samples after 3 cycles of PIP are shown here. It

can be concluded that the final ceramic part is made of highly crystalline SiC particles (mostly cubic phase) and amorphous PDC.

XPS experiments were conducted on thermally cured Durazane 1800 samples pyrolyzed under argon at 800 °C (Figure 3.7) to determine the matrix PDC composition in the presence of the SiC particles.

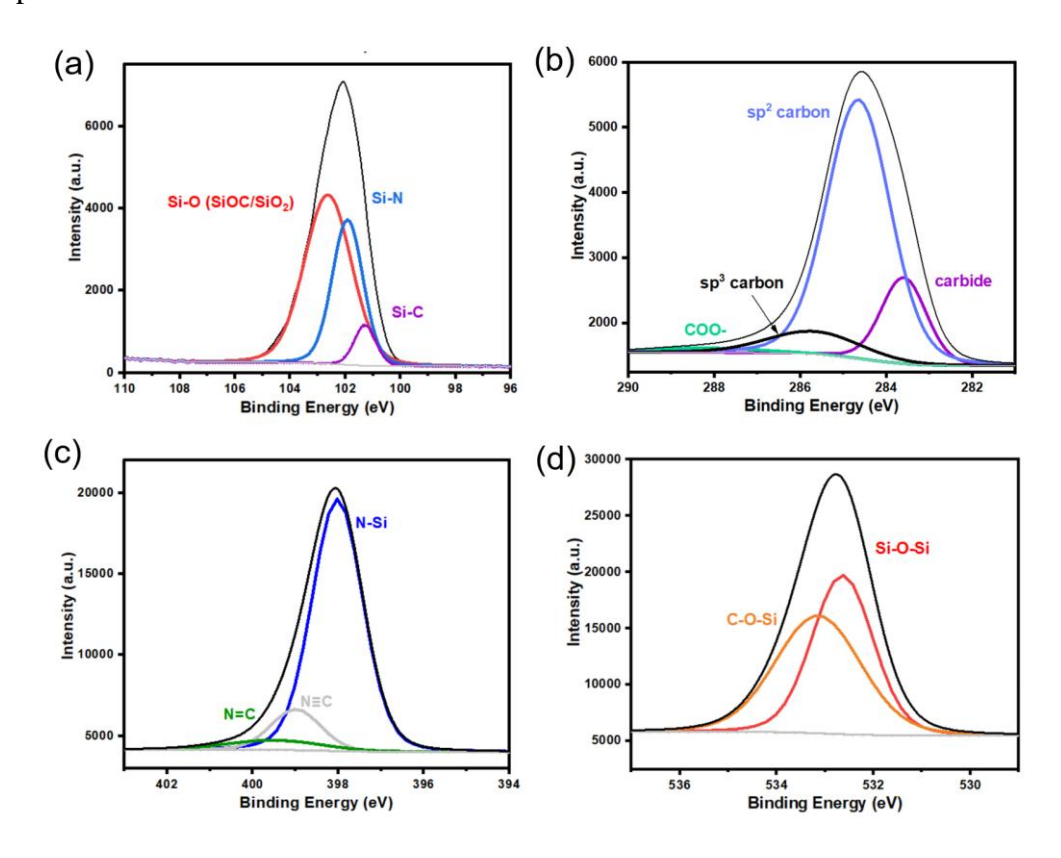


Figure 3.7. (a) XPS spectrum of Si 2p; (b) XPS spectrum of C 1s; (c) XPS spectrum of N 1s; (d) XPS spectrum of O 1s. All the spectra are taken for pyrolyzed Durazane.

From the Si 2p XPS spectrum in Figure 3.7(a), peaks at 102.6 eV, 101.9 eV, and 101.3 eV correspond to Si-O (SiOC/SiO<sub>2</sub>), Si-N and Si-C, respectively. For the C 1s spectrum (Figure 3.7(b)), peaks at 288.1 eV, 285.7 eV, 284.6 eV, and 283.6 eV correspond to COO-, sp<sup>3</sup> carbon, sp<sup>2</sup> carbon, and carbide, respectively. Turning to N 1s XPS spectra in Figure 3.7(c), the three

peaks identified at 399.4 eV, 399.0 eV, and 398.0 eV are N=C, N=C, and N-Si. Finally, the two peaks in the O 1s spectrum (Figure 3.7(d)) indicate two types of O: C-O-Si at 532.2 eV and Si-O-Si at 532.6 eV. From the XPS spectra, C, N, O, and Si are calculated to have 25.7 atom%, 18.8 atom%, 20.3 atom%, and 35.3 atom% abundance in the sample, respectively.

XPS spectra show the elemental composition of the ceramic matrix of the PDC composite. When combining the results from XPS (Figure 3.7) and FTIR (Figure 3.5(c)), it can be concluded that the ceramic matrix from pyrolysis of Durazane is mainly made of a mixture of SiCN and SiOC, with some SiO<sub>2</sub> in the sample. When considering the evidence from XRD (Figure 3.6(a)) and FTIR (Figure 3.5(d)), It can be concluded that the samples after PIP are mainly composed of crystalline 3C-SiC SiC particles (Figure 3.6(b-d)) with an amorphous SiCN and SiOC matrix.

SEM analysis was conducted to analyze the morphology of the samples and to determine how the PIP process changed their microstructure and porosity. The SEM micrograph of the NIR-printed samples and the oven-cured samples showed similar microstructures (Figure 3.8), where an increase in PIP cycles helped to decrease the gaps between SiC particles with increased PDC yield.

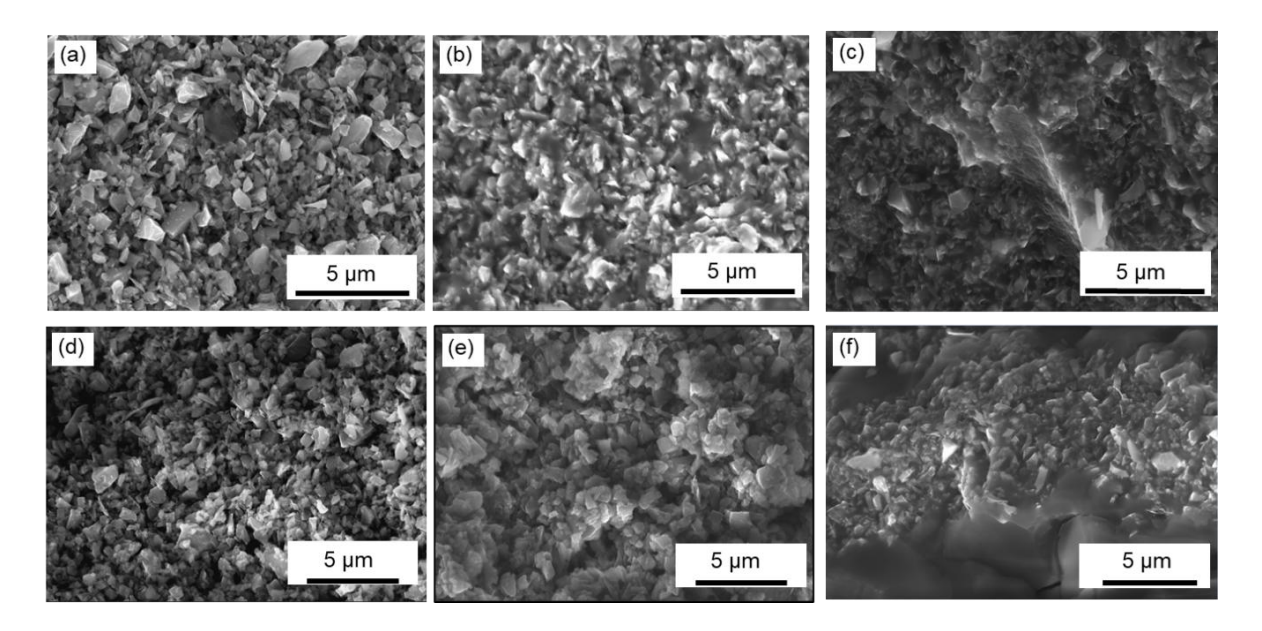


Figure 3.8. (a) Oven-cured sample after debinding (PIP 0); (b) oven-cured sample after 1 cycle of PIP (PIP 1); (c) oven-cured sample after 5 cycles of PIP (PIP 5); (d) NIR-printed sample after debinding (PIP 0); (e) NIR-printed sample after 1 cycle of PIP (PIP 1); (f) NIR-printed sample after 5 cycles of PIP (PIP 5). All images were taken on fractured surfaces.

The *DUDMA-SiC 50:50* sample after debinding (PIP 0) showed a rough surface composed primarily of crystalline SiC particles due to the near-complete burn-off of the binder. There were no sample dimensional changes throughout the PIP cycles; the only dimensional change associated with the post-processing procedure was the debinding of the green body, during which 9.4 % linear shrinkage occurred following the removal of organic binders. Since the PIP process does not increase the volume of the samples, PCP infiltrated into the pores will turn into PDC within the porous body and densify the samples after pyrolysis. After one cycle of PIP, most of the SiC particles were held together with amorphous SiOC and SiCN from the PCP (Durazane) (Figure 3.8 (b)). However, pores are still visible in these samples, and the density after one PIP cycle was 1.76 g/cm<sup>3</sup> for NIR-printed samples. After five cycles of PIP, almost all

the particles in the sample appear to be consolidated, and there are no visible pores in the sample, according to microscopic analysis, Figure 3.8(f). Moreover, the samples after five cycles of PIP showed a non-porous structure, where fewer openings are present in the amorphous SiOC and SiCN matrix region.

The density of the NIR-printed samples increased from 0.85 to 2.36 g/cm<sup>3</sup> after five PIP cycles toward an estimated composite theoretical density of 2.60 g/cm<sup>3</sup>. The theoretical density was estimated assuming a composition of 40 wt % SiC ( $\rho = 3.21$  g/cm<sup>3</sup>) and 60 wt % amorphous SiOC ( $\rho = 2.3$  g/cm<sup>3</sup>). Figure 3.9 shows density measurements for NIR-printed and oven-cured samples as a function of the number of PIP cycles. This data demonstrates that the oven-cured and printed samples showed similar density increases during the PIP processes.

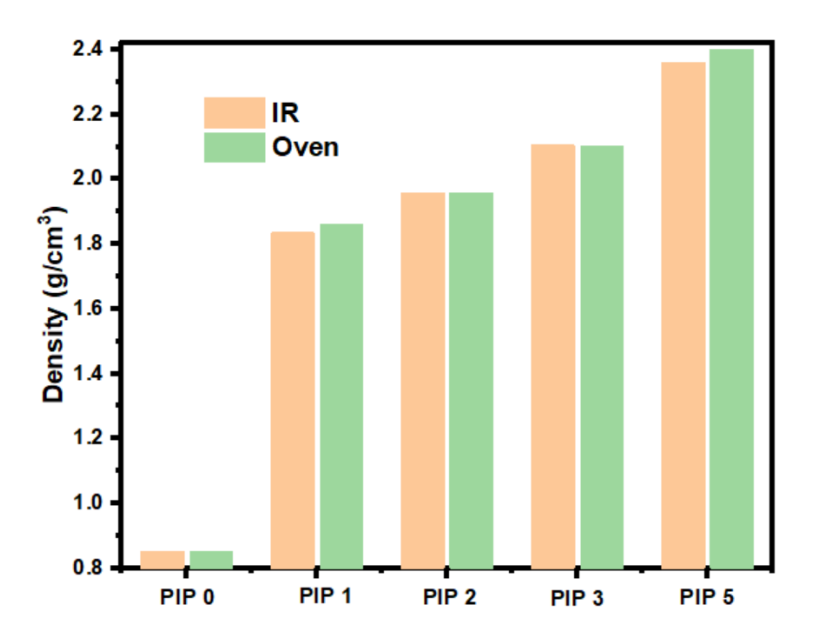


Figure 3.9. Density measurement of oven-cured and NIR-printed samples after different PIP cycles.

As discussed in the previous section, PIP as a post-processing method will densify and strengthen the porous debinded samples. Mechanical analyses, including three-point bending and

microindentation, were performed to determine the flexural strength and fracture toughness of oven-cured and NIR laser-printed samples. This testing allowed us to assess the impact of PIP on the strength and fracture toughness of the samples.

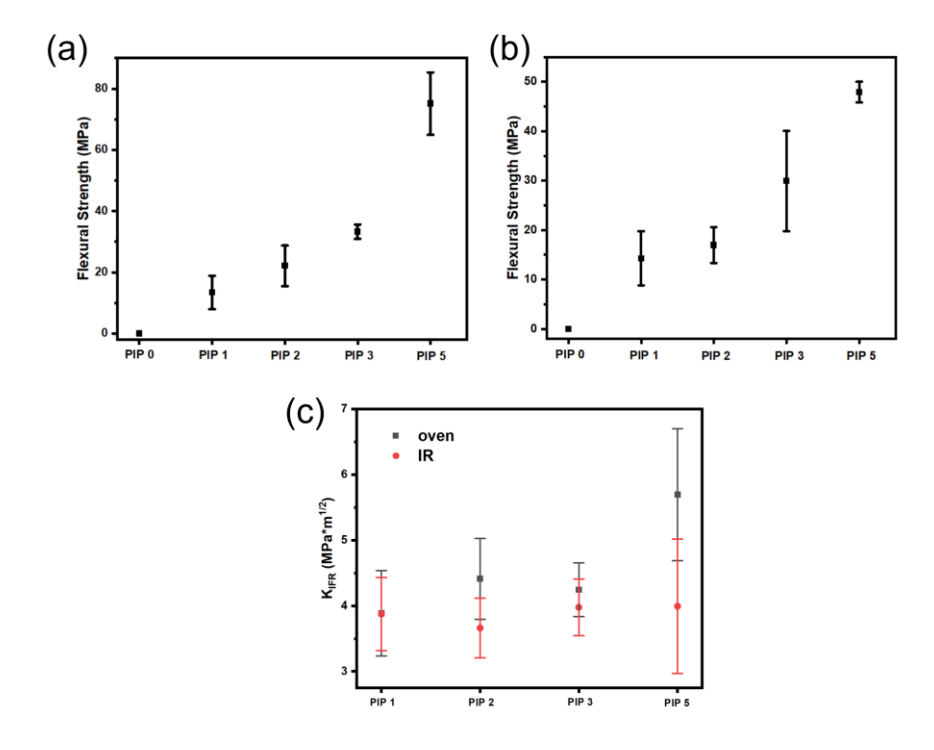


Figure 3.10. (a) Flexural strength of PIPed oven-cured *DUDMA-SiC 50:50* samples; (b) flexural strength of PIPed IR DUDMA-SiC 50:50 samples; (c) fracture toughness of DUDMA-SiC 50:50 samples. Error bars represent the standard deviation (± SD) of the measurement.

The debinded green body samples only have negligible strength (0.1 MPa). However, the flexural strength of oven-cured samples increased from 13.43 MPa (PIP 1) to 75.12 MPa (PIP 5) with a 459 % increase (Figure 3.10(a)), which can be explained by the fact that the PDC composites were becoming denser with an increased PIP cycle count. The oven-cured and PIPed samples showed excellent flexural strength,  $75.1 \pm 10.2$  MPa (PIP 5, Figure 3.10(a)), which is comparable to the 3D printed SiC PDC composite reported before with a flexural strength of 66.8 MPa. 141 Compared to oven-cured samples, the NIR printed samples after PIP showed

relatively lower mechanical strength,  $47.9 \pm 2.1$  MPa (Figure 3.10(b)). This is likely due to the NIR-printed samples having more defects than oven-cured samples due to the layered nature of 3D printing. Additionally, the NIR-printed samples have a rougher surface finish because the printer is only a first proof-of-concept. Typically, the flexural strength of polymer-derived ceramics (PDCs) is relatively low, leading researchers to enhance strength by adding fillers or whiskers. Our PDC composites show significantly improved strength compared to preceramic polymers alone and are comparable to reported values. For example, Cramer et al.  $^{142}$  66.8 MPa using binder jet 3D printing with polycarbosilanes. Kemp et al.  $^{112}$  reported 56.4  $\pm$  7.6 MPa by adding hBN in polysilazane. Xiong et al.  $^{119}$  obtained 33.2 MPa with SiC whiskers, and Huang et al.  $^{143}$  reported 15.8 MPa for porous SiC.

The fracture toughness of the samples was measured using the indentation method described in the main manuscript. The parameters that need to be measured for this method are hardness, crack length, and the force applied to the tip. The indentation fracture toughness increased by 47 % for oven-cured samples after 5 PIP cycles, while it only increased negligibly (3.1 %) for NIR-printed samples, where it reached  $5.7 \pm 0.9$  MPa·m<sup>1/2</sup> for oven-cured samples and  $4.0 \pm 0.9$  MPa·m<sup>1/2</sup> for NIR-printed samples (Figure 3.10(c)). Higher PIP cycles tend to toughen the microstructure and enhance mechanical properties as they increase the fracture resistance of the samples. After a PIP cycle, the infiltration PDCs are softer and act as plastic regions to absorb more energy during fracture. However, IR-printed samples exhibit a less pronounced improvement in fracture toughness. This can be attributed to the presence of inherent defects introduced during the IR printing process, as evidenced in the SEM micrograph. These defects likely act as stress concentrators and preferential sites for crack initiation, limiting the

efficacy of the toughening mechanisms provided by the plastic matrix. The average reported fracture toughness of Si-C-N and Si-O-C systems<sup>21</sup> is 0.56 - 3 MPa·m<sup>1/2</sup>. Thus, the PDC composite in this report shows an improvement over materials systems that have been demonstrated previously.

#### 3.5. Conclusions

This work presents the development of a novel thermal SLA printer to fabricate PDC composite parts, solving issues with UV-based SLA printing of PCPs. Additionally, a thermal printing resin composition was reported in this study, with a SiC particle loading of 50 wt%. FTIR analysis showed a small compositional difference between laser-cured and oven-cured PDC samples, which supports the feasibility of NIR thermal printing in obtaining PDC materials with good properties. The crystalline structure of the particles and the matrix was characterized by XRD analysis, where the results confirm that the filler particles are crystalline 3C-SiC particles while the matrix is amorphous. The chemical composition of the PDC composite after PIP was measured with FTIR and XPS, demonstrating that amorphous SiOC and SiCN are the main components of the matrix. Following PIP, the printed parts demonstrated high mechanical strengths (48 MPa) and fracture toughness (4.0  $\pm$  0.9 MPa·m<sup>1/2</sup>). SEM images showed how the PIP procedure strengthened the samples – consolidating the particulate filler with an amorphous PDC matrix from PCP pyrolysis. During printing, heat conduction in the resin causes thermal energy to diffuse beyond the irradiated area, reducing resolution. Future work will focus on improving heat dissipation through enhanced convection and conduction cooling, which could mitigate thermal diffusion and improve resolution. This prototype demonstrates NIR laser

stereolithography for preceramic polymers, addressing challenges in UV-based printing and showing the potential of thermal SLA for fabricating PDC 3D-printed parts.

### CHAPTER 4: STRUCTURED PDC COMPOSITES VIA NIR THERMAL SLA

Parts of this work are adapted from the work of Evelyn Wang and Michael A. Hickner.

Under review under ACS Applied Polymer Materials. This is the version of the article after peer review or editing as submitted by the authors for publication. The publisher is not responsible for any errors or omissions in this version of the manuscript, or any version derived from it.

#### 4.1. Abstract

We have developed NIR thermal SLA to print 2.5D-structured PDC composites with high SiC particle loadings in a PDC matrix. When combined with PIP, this approach overcomes the challenges associated with traditional UV-based printing techniques when printing composite resins – namely low light penetration, limited particle loadings, high shrinkage, and weak mechanical properties. Using a NIR laser to deliver spatially controlled thermal energy to the surface of a reactive resin pool induces localized thermally initiated free-radical polymerization in a top-down SLA configuration. After printing the green body, post-processing methods, including debinding and PIP, are employed to densify and strengthen the printed samples. A Si-O-C<sub>x</sub> support network was formed in the debinded samples using a small amount of PCP in the printing resin to maintain the structural integrity of this porous preform. After 5 cycles of PIP, the PDC composites demonstrated a flexural strength of  $74.3 \pm 13.7$  MPa with a density of 2.31 g/cm<sup>3</sup>. Different 2.5 D lattice designs were fabricated using this printing and materials processing method, and a compressive strength of  $32.8 \pm 11.2$  MPa was obtained for lightweight honeycomb structures with an effective density of 1.07 g/cm<sup>3</sup>.

## 4.2. Introduction

As a high-performance material, composite ceramics are gaining attention for a broad spectrum of applications, including aerospace, biomedical, energy, and electronics<sup>115,119,144</sup>. However, relative to other materials, composite ceramics have achieved a limited role in these applications, primarily because ceramics are difficult to process into intricate structures, which can limit their development.<sup>84</sup> Despite having excellent mechanical properties, environmental resistance, and temperature tolerance, the hurdles surrounding ceramic processing have primarily limited the adoption of this class of materials.<sup>50</sup>

The introduction of PDCs has opened the door to combining the mechanical performance of Composite ceramics with the superior processability of polymer.<sup>21</sup> Liquid PCPs can be shaped into components with complex geometries due to the flexibility offered by polymer processes such as molding and AM.<sup>145</sup> These shaped PCP green bodies can then be pyrolyzed under high temperatures and transformed into ceramics such as SiC, SiOC, SiCN, Si<sub>3</sub>N<sub>4</sub>, and SiBCN, among others.<sup>50,97,116</sup> PDCs are used in ceramics infiltration, ceramic fiber fabrication, and AM.<sup>21</sup> Unlike traditional ceramic AM with powder processing<sup>50</sup>, PDCs do not require techniques for consolidating a ceramic structure using traditional sintering pathways<sup>146</sup>, which makes PDC-AM a potential low-temperature method of producing ceramic parts.<sup>91</sup> The pyrolysis temperature of PCPs ranges from 800 – 1300 °C,<sup>84</sup> which is significantly lower than the sintering temperature of ceramics like SiC and Si<sub>3</sub>N<sub>4</sub>.<sup>144</sup> Moreover, PDCs can offer high modulus, high strength, and oxidation and creep resistance up to 1500 °C, even though they are usually semicrystalline with the presence of crystalline ceramic nanodomains in an amorphous matrix.<sup>147</sup>

The development of AM methods has progressed rapidly, evolving from simple 2D printing techniques into stereolithography or additive manufacturing of three-dimensional objects (3D printing). 148 With the advent of readily available 3D printing hardware, researchers have focused on adapting the well-defined principles of AM to a vast catalog of materials. A great process has been made by adopting different approaches in 3D printing technologies from 2D platforms, such as origami-inspired approaches <sup>149</sup> (2D plane folding into 3D structures), layer-by-layer stacking 150, and 1D extrusion direct writing 88. Currently, a number of 3D printing methods have achieved maturity – FFF, SLS, DLP, DIW, material/binder jetting, and others. 91,116 UV light-based processes, specifically DLP and SLA, have enjoyed widespread adoption in several manufacturing processes and have been demonstrated to be effective in producing complex and smooth 3D structures with functionalized PCPs<sup>50</sup>. However, UV-based printing of PCPs is limited in terms of materials and resin compositions. Dense Composite ceramics with high particle loadings are desired in resin compositions. However, the large refractive index mismatch between the filler particles and the polymer precursors inevitably leads to significant light scattering and reduced penetration depth, lowering the printing resolution and decreasing print speed. 105 Direct UV-SLA of polysilazanes requires a photoinitiator absorbing UVC region<sup>101</sup>. Such short-wavelength UV light is more likely to cause damage to the polymer and requires a high-power mercury-vapor lamp<sup>151</sup>. Even though many reports add crosslinker with vinyl<sup>146</sup>, acrylate<sup>117</sup>, or thiol<sup>101</sup> functionality to facilitate the printing of PCP, they inevitably lower the ceramic yield of PDC and increase the carbon content in the pyrolyzed ceramic samples<sup>59</sup>.

There has been two adoptions of harnessing thermal energy in realizing thermal-based 3D printing in the literature as an alternative to UV-based SLA – either directly utilizing the thermal energy from the NIR laser for polymerization<sup>152,153</sup> or using additives like gold nanoparticles as photothermal converters in polymerization<sup>154</sup>. The most significant advantage of using a NIR thermal SLA to induce thermal curing of the resin is the broad potential scope of thermal curing chemistry across a range of materials<sup>152</sup>. Also, the NIR thermal SLA technique can print resin compositions with high particle content (47.6 wt% SiC particles (1 µm) in this report), which has not been demonstrated with a UV-based printer due to light penetration issues. Since the highintensity laser heats the resin rapidly, the crosslinking reaction occurs quickly – with sufficient green strength achieved in as little as a tenth of a second during the printing process. The resulting ceramic parts from thermal SLA have relatively high resolution and smooth surfaces compared to 3D printing methods like DIW<sup>153</sup>. Finally, post-processing is simplified for composite ceramics printed via NIR thermal SLA, where the green body can be pyrolyzed into a ceramic component after simple washing and post-curing, similar to conventional UV SLA posttreatments.

Polymer infiltration and pyrolysis is an effective method of obtaining reinforced ceramic composite materials, during which PCP is infiltrated into the porous preform and subsequently pyrolyzed into PDC.<sup>142</sup> A higher number of PIP cycles can lower the residual porosity in the preform and yield a densified and reinforced structure with densities approaching the theoretical material density. Repeated PIP cycles (up to 5 or 7 cycles) benefit the sample by providing more linkages between the particles while simultaneously vaporizing unnecessary atoms, thereby increasing ceramic yield and mechanical strength with each successive pyrolysis step.<sup>155</sup>

In this work, we report developing an NIR thermal SLA printing method for the AM of highly loaded resin compositions. A porous body composed primarily of SiC particles with a supporting PCP-derived structure is fabricated through printing and subsequent debinding.

Durazane 1800 was used in multiple PIP cycles to produce dense PDC composites. The printed samples and lattices demonstrate reasonable flexural strength and compressive strength, which demonstrates this printing method is capable of producing lightweight particle-based composite ceramics with excellent mechanical properties and size features on the order of millimeters.

# 4.3. Experimental section

## 4.3.1. Materials

Poly(propylene glycol) dimethacrylate (PPGDA,  $M_n$  = 560), acetone (99.5 %), and dicumyl peroxide (98 %) were purchased from Sigma-Aldrich (St. Louis, MO). Durazane 1800 was supplied by Merck KGaA (Darmstadt, Germany), and silicon carbide (1  $\mu$ m,  $\beta$ -phase, > 99.5%) was purchased from Beantown Chemical (Hudson, NH). SMP 877 resin was purchased from Starfire Systems (Glenville, NY). All chemicals were used as received. The optics for the NIR thermal SLA printer were purchased from Thorlabs Inc. (Newton, NJ), and an 808 nm fiber laser (33 W) was supplied by Lumics (Berlin, Germany) as the thermal SLA laser source.

Figure 4.1. Chemical structures of (a) PPGDA; (b) Durazane 1800; (c) dicumyl peroxide; (d) SMP 877.

Figure 4.1 shows the chemical structures of the materials used in this report, while Table 4.1 lists the resin compositions.

Table 4.1. Resin chemical compositions

	PP	PP10%877	PP20%877	PP30%877
		(PP877)		
PPGDA / g	10	10	10	10
Dicumyl Peroxide / g	0.1	0.1	0.1	0.1
SMP 877 / g	0	1	2	3
SiC / g	10	10	10	10

# 4.3.2. Sample preparation

The resin mixture for printing consists of two types of resins: acrylate oligomer PPGDA as the major resin component for crosslinking and facilitating the support of 3D structures and polycarbosilane SMP 877 as the minor resin component for obtaining a percolated Si-O- $C_x$ 

supporting structure in the green bodies during debinding. For a typical resin composition, all the resin ingredients (Table 4.1) were transferred into a 500 mL round bottom flask. After adding 100 mL of acetone to the flask with the resin components, the mixture was stirred with a magnetic stirrer at 600 RPM for 12 h. After mixing, the acetone was subsequently removed with a rotary evaporator, obtaining the printing resin *PP877*.

# 4.3.3. Thermal SLA printer

The NIR thermal SLA printer consists of four major parts: a high-intensity 808 nm NIR laser fixed onto an optical cage, a fixed build support, a mesh build plate that moves in the z-axis, and a resin tray (Figure 4.2).

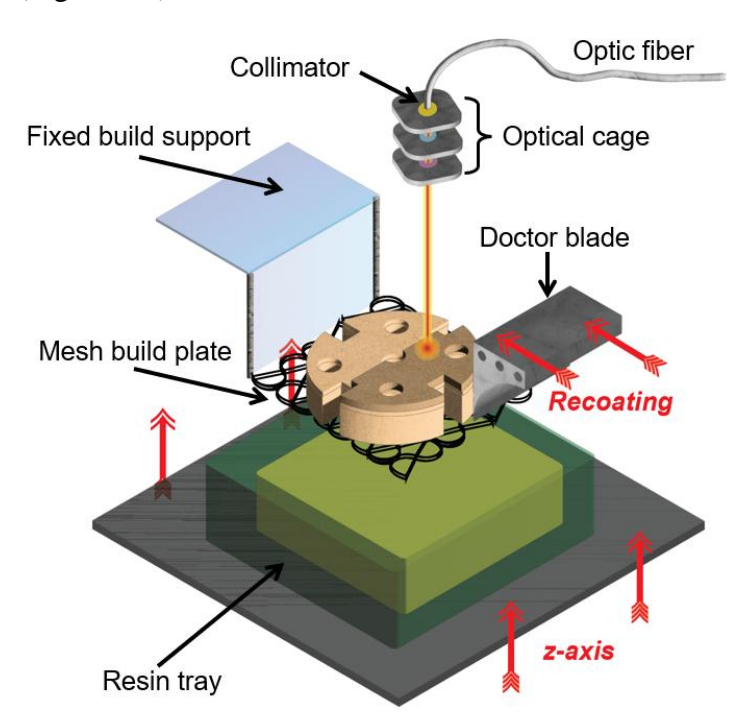


Figure 4.2. NIR thermal SLA printer for fabrication of 2.5D structures.

The optical cage is attached to an x-y-axis gantry, where a collimator and a set of lenses are fixed in the optical cage for beam collimation and controlling the laser waist diameter and divergence (the same in section 3.3.3). A mesh build plate is fixed onto the build support to hold

the newly constructed structures built in a traditional laser-wise fashion. The resin reservoir will move up the z-axis to replenish new liquid resin layers onto the printed structures. Notably, the laser and the gantry can move at speeds up to 10 cm/s during the printing, resulting in a printing speed comparable to UV SLA.

During a typical printing process, a 3D model is sliced with 3D printing software (Creality Slicer 4.8.2) to generate a set of G-code instructions for the printer. The 3D printing process begins with immersing the mesh build plate into the resin pool by elevating the resin tray on z-axis support. After the mesh build plate is coated with a single resin layer, the NIR laser writes the first layer onto the high-flow mesh. Then, the resin tray will move up to recoat the resin on the solidified layers with the help of a doctor's blade, providing new resin layers for the NIR laser to cure. New layers will be generated so that a 3D structure can be fabricated through laser and gantry movements. The transition from 2D to 3D printing is achieved by stacking multiple layers together, where each layer contributes to the details and structures of the final prints. Thermal images were taken using a Teledyne FLIR C5 thermal camera (Figure 4.3), capturing how the NIR laser delivered localized heat to the resin pool. After printing, the parts were washed with acetone 3 times to remove uncured resin, and the samples were fully cured in a vented oven at 150 °C for 20 min.



Figure 4.3. NIR-assisted SLA process under a thermal camera.

Figure 4.3 demonstrates a typical NIR-assisted SLA process visualized using a thermal camera. Heat is spatially distributed only in the printing area to obtain the desired structures and minimize the thermal curing of non-printed areas.

# 4.3.4. Sample post-processing

A two-step post-processing scheme was applied to densify and strengthen the green body. First, the green body was transferred to a vented muffle furnace at room temperature. The sample was subsequently heated to 500 °C with a ramp rate of 0.4 °C /min, dwelled for 1 h, and cooled down to room temperature with a ramp rate of 1 °C/min for decomposition and removing most of the polymeric species. After debinding, the porous preform was subsequently processed by PIP, where the debinded porous preform was densified by multiple cycles of infiltrating PCP and pyrolysis. The debinded sample was transferred into a three-neck round-bottom flask during a typical PIP cycle. Then, the flask was sealed and degassed until the system reached a pressure of less than 5 kPa. A low-viscosity (20 °C, 10 - 40 cp) PCP Durazane 1800 was chosen for backfilling the pores/channels in the sample. Durazane 1800 (with 1 wt.% dicumyl peroxide as

thermal initiator) was released dropwise onto the sample at a 10 mL/min rate until the sample was fully immersed. The sample was kept under the vacuum for 20 min until no more bubbles were released from the structures. After infiltration, the sample was transferred to a tube furnace under argon flow (50 cm³/min). The sample was heated to 170 °C with a ramp rate of 1.2 °C /min and subsequently heated to 800 °C with a ramp rate of 0.48 °C/min. The sample was held at 800 °C for 1 h before being cooled to room temperature at 1 °C/min. Repeating this procedure of infiltration and pyrolysis will produce samples processed with multiple PIP cycles.

## 4.3.5. Characterization

All characterization methods are the same (section 3.3.6) except for compressive strength. The mechanical properties were measured with an MTS Criterion 43 (C43.504, Eden Prairie, MN) load frame. Compressive strength was measured with an MTS 20 kN S-beam load cell equipped with compression platens.

The performance index,  $P_1$  during the compression test is calculated as shown in eq.  $4.1^{145}$ :

$$P_{\rm I} = \frac{\rho}{\sigma} \tag{4.1}$$

where  $\rho$  and  $\sigma$  represent the sample's density and compressive strength.

## 4.4. Results and discussion

The printed 2.5D structures (Figure 4.4) showed excellent layer-to-layer adhesion with the NIR thermal SLA printer. When fabricating hollow 2.5D structures, the printer demonstrates the ability to maintain high fidelity and accuracy.

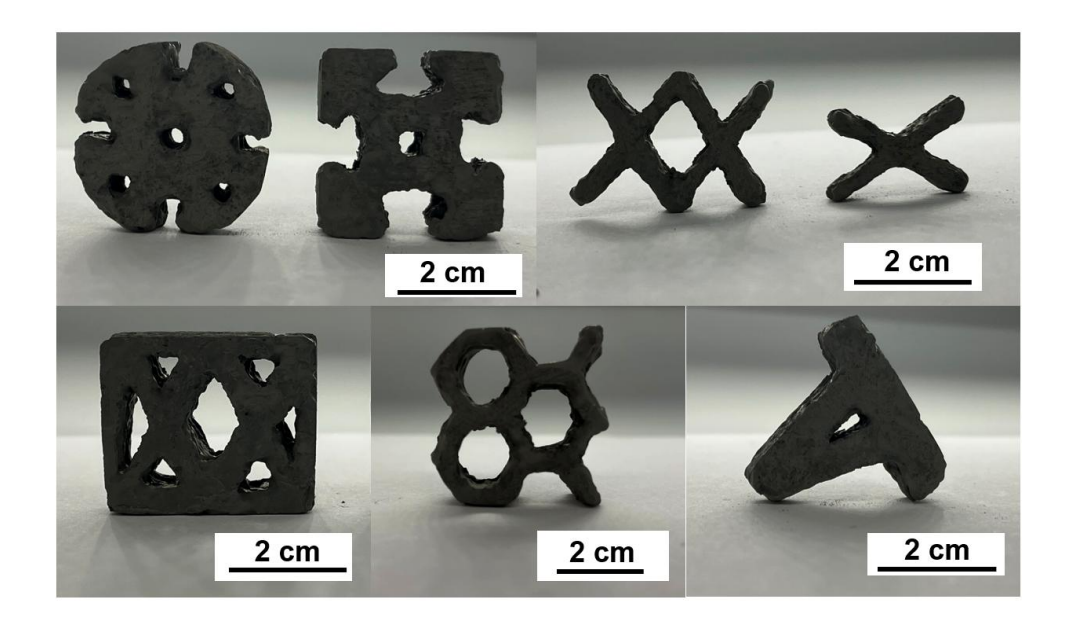


Figure 4.4. Demonstration of 2.5D-printed green part structures with NIR thermal SLA printer.

Printing resolution was demonstrated by fabricating different lattice structures, where structures as fine as 1.20 mm can be made through a single scan of the NIR laser. Overall, the NIR thermal SLA demonstrates the capability to reproduce the details from the original 3D models.

FTIR spectra are shown for NIR-printed, un-cured printing resin *PP877* (Figure 4.5(a, b)); debinded samples with and without Si-O-C<sub>x</sub> structural support (Figure 4.5(c)); and debinded green body after different cycles of PIP (Figure 4.5(d)).

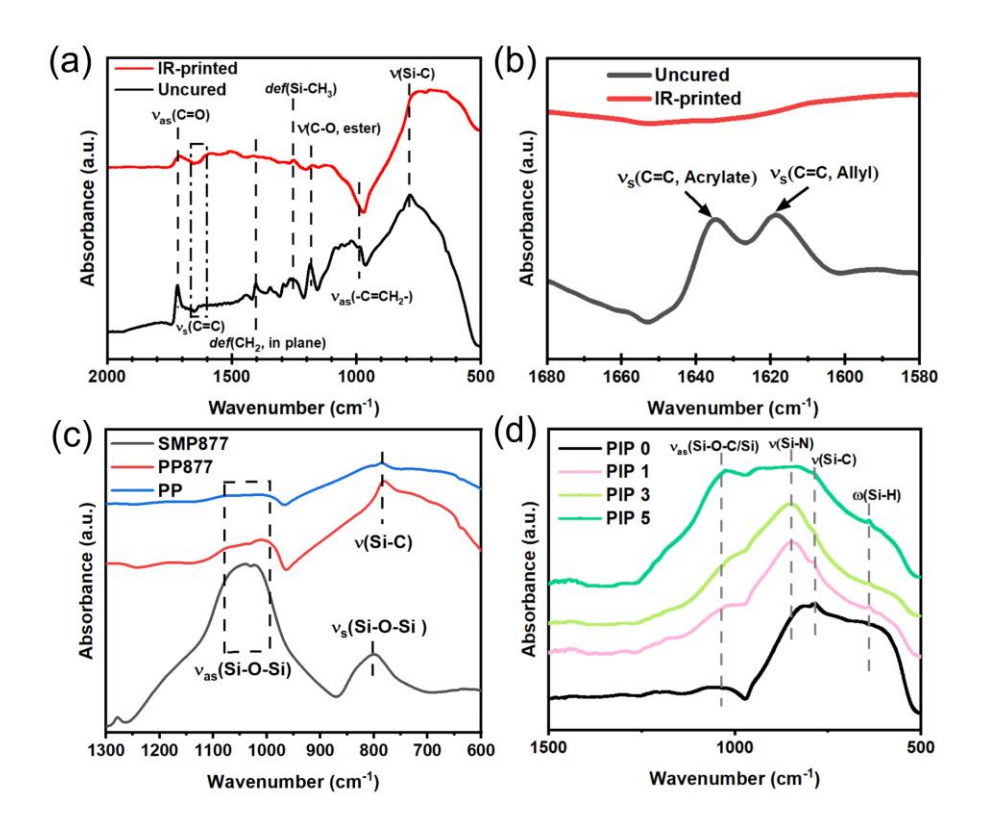


Figure 4.5. FTIR spectrum of (a) IR-printed and uncured *PP877* samples; (b) IR-printed and uncured *PP877* samples zoomed-in range; (c) SMP 877, *PP*, and *PP877* debinded in the air at 500 °C (in Table 4.1); (d) IR-cured *PP877* samples after cycles of PIP.

Figure 4.5(a,b) highlights the resin composition before and after IR printing. The diminished  $v_{as}$ (-C-H) in the -C=CH<sub>2</sub>- moiety<sup>137</sup> at 980 cm<sup>-1</sup>, and the disappearance of acrylic<sup>137</sup>  $v_s$ (C=C) and allyl  $v_s$ (C=C) peak at 1635 cm<sup>-1</sup> and 1615 cm<sup>-1</sup> showed clear evidence of curing of the acrylate-terminated PPGDA and allyl group in SMP 877 resin. While SMP 877 resin does not cure on its own under 200 °C, this data supports that adding the methacrylate resin promotes the crosslinking of the SMP 877 resin. The purpose of adding SMP 877 as PCP before debinding is to support the debinded structure since the SMP 877 does not fully burn away. In contrast, pure acrylate resins burn entirely off at this temperature. Figure 4.5(c) shows that pure SMP 877 (black curve), after debinding in the air at 500 °C, turns into a network containing a Si-O-Si

structure, where the peaks at  $1020 - 1050 \, \mathrm{cm^{-1}}$  and  $780 - 790 \, \mathrm{cm^{-1}}$  correspond to asymmetric and symmetric  $v(\mathrm{Si\text{-}O\text{-}Si})^{139}$ , respectively. Compared to the resin composition with structural support (*PP*877, red curve), the resin composition without structural support (*PP*, blue curve) showed a weaker  $v(\mathrm{Si\text{-}O\text{-}Si})$  peak. Figure 4.5(d) shows the chemical composition of the printed samples after different cycles of PIP, and there is evidence of  $\mathrm{SiO_2^{139}}$  ( $v_{as}(\mathrm{Si\text{-}O\text{-}Si})$  at  $1050 - 1070 \, \mathrm{cm^{-1}}$ ) and  $\mathrm{SiOC}$  ( $v_{as}(\mathrm{Si\text{-}O\text{-}C})$  at  $1025 \, \mathrm{cm^{-1}}$ ). Additionally, the  $v(\mathrm{Si\text{-}N})$  bond at  $830 - 840 \, \mathrm{cm^{-1}}$ ,  $v(\mathrm{Si\text{-}C})$  bond at  $785 \, \mathrm{cm^{-1}}$ , and  $\omega(\mathrm{Si\text{-}H})$  bond  $^{138}$  at  $638 \, \mathrm{cm^{-1}}$  indicates some presence of SiCN and unpyrolyzed Si-H.

The XPS analysis was conducted on the structural support after debinding to determine its chemical composition, Figure 4.6.

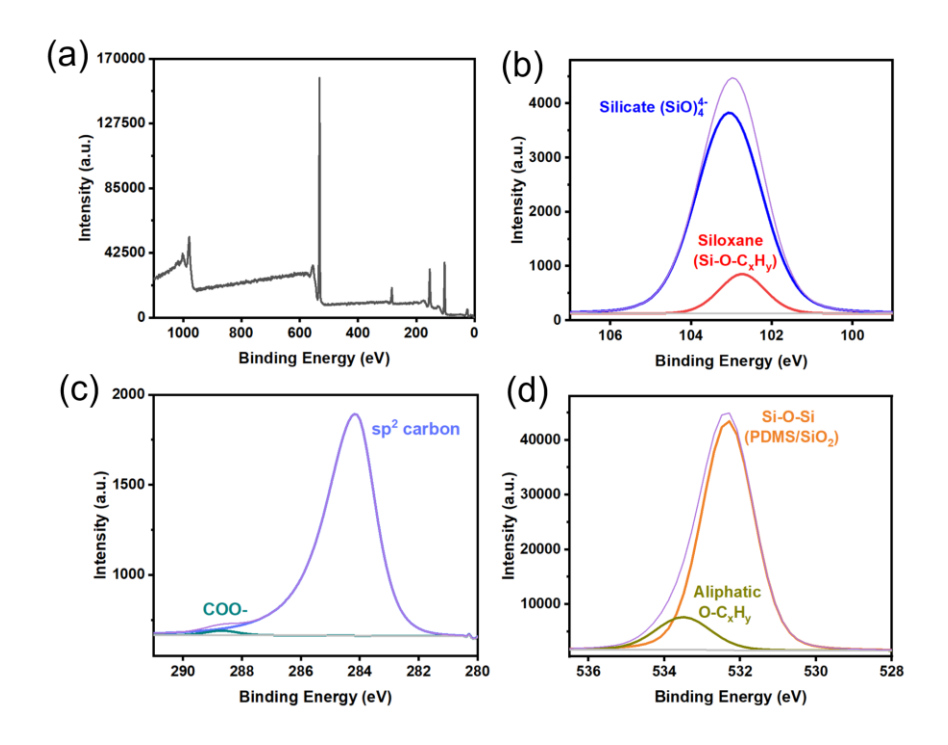


Figure 4.6. (a) XPS survey spectrum; (b) XPS spectrum of Si 2p; (c) XPS spectrum of C 1s; (d) XPS spectrum of O 1s of resin SMP-877 without fillers debinded in the air at 500 °C.

Figure 4.6(a) shows the survey spectrum of SMP-877 debinded in the air at 500 °C, where the debinding procedure is identical to the green body debinding. In Figure 4.6(b) Si 2p spectrum, the XPS peaks at 102.7 eV and 103.1 eV correspond to siloxane<sup>156</sup> and silicate<sup>156</sup>, showcasing both inorganic and organic structural characteristics in the debinded samples. In the C 1s spectrum in Figure 4.6(c), the peaks at 284.2 eV and 288.7 eV correspond to sp<sup>2</sup> carbon and COO-, respectively<sup>156</sup>. The peaks at 532.3 eV and 533.5 eV are assigned to (Figure 4.6(d)) correspond to Si-O-Si (PDMS/SiO<sub>2</sub>) and aliphatic groups<sup>156</sup>, reinforcing the previous finding in Si 2p spectrum there are both inorganic and organic moieties in the green bodies after debinding in air. Additionally, after debinding in the air at 500 °C, SMP 877 turns into a rigid, yellow-colored solid structure instead of a white powder, which is evidence of the percolated Si-O-C<sub>x</sub> network being formed in the debinded 3D-printed samples.

When combining insights from the FTIR data in Figure 4.5(c), it can be concluded that adding SMP 877 into the green body and debinding in the air will turn into a network of Si-O-C<sub>x</sub>. Incorporating SiOC and SiCN by the PIP process densifies the porous preforms and strengthens the material.

XRD analysis (Figure 4.7) was conducted on the pyrolyzed Durazane 1800 sample and *PP877* sample after 5 cycles of PIP to analyze the crystalline structure and phases of the matrix PDC and the samples after PIP.

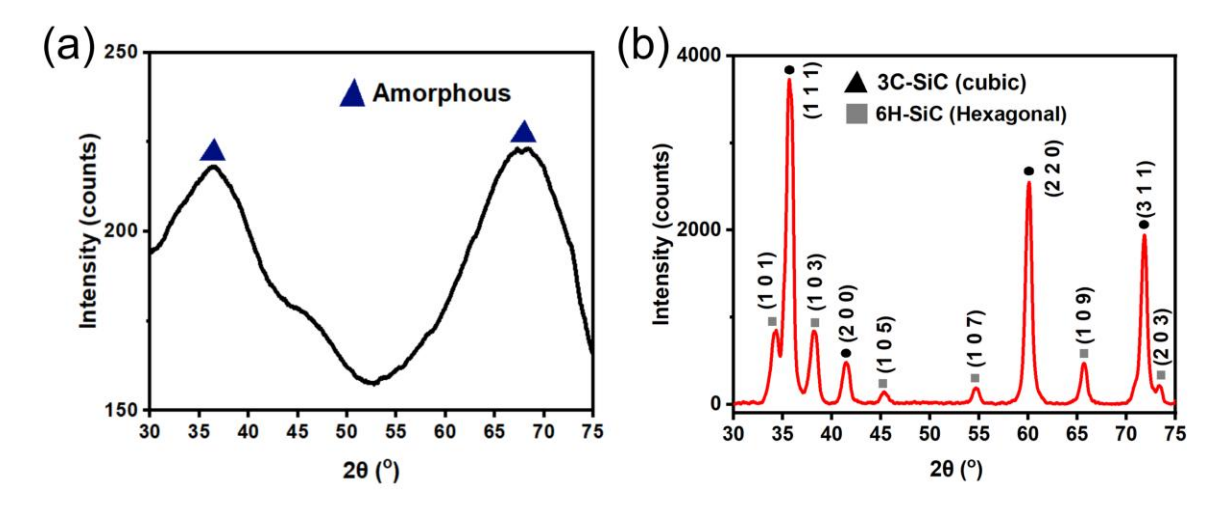


Figure 4.7. (a) XRD pattern of pyrolyzed Durazane 1800; (b) XRD pattern of PP877 sample after 5 cycles of PIP. Both samples are pyrolyzed under identical furnace conditions detailed in the experimental section.

It is evident in Figure 4.7(a) that there is no distinguishable crystalline species from the pyrolyzed Durazane, where the amorphous halo at around 35 - 38° and 65 - 70° represents 3C-SiC. This data demonstrates that the PDC introduced in the PIP process is entirely amorphous. The XRD patterns of the samples after PIP and Durazane 1800 after pyrolysis are shown in Figure 4.7(b), where cubic SiC from the incorporated particles are found to be the most abundant crystalline structures in all the samples. This confirms that the samples are made of crystalline 3C-SiC particles with minor 6H-SiC and amorphous PDC matrix from post-processing PIP.

SEM micrographs of debinded samples were taken after different cycles of PIP (Figure 4.8) to analyze structural changes throughout the post-processing steps. This analysis helps explain the enhanced mechanical properties observed in the 3D-printed samples.

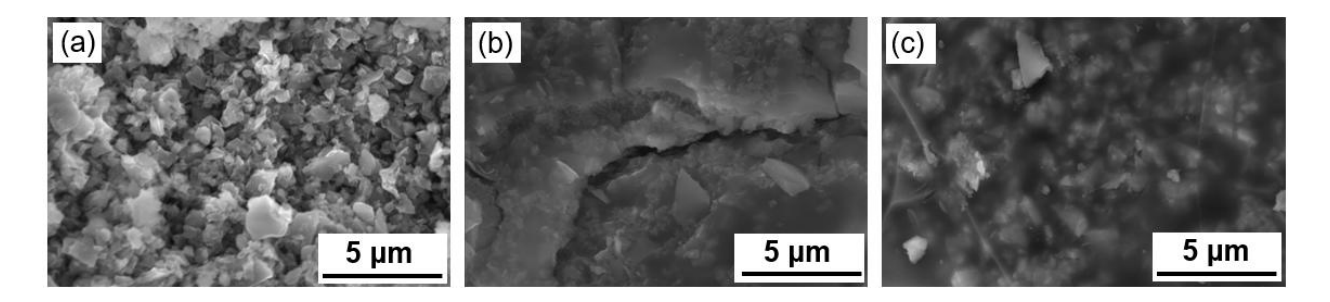


Figure 4.8. SEM micrographs of NIR-printed *PP877* sample after (a) debinding (PIP 0, porous preform); (b) 3 cycles of PIP (PIP 3); (c) 5 cycles of PIP (PIP 5).

The effects of how PIP strengthens the porous debinded samples are shown in Figure 4.8. From these SEM micrographs, it is evident that with higher PIP cycles, there are reduced openings and cracks throughout the samples. The samples after debinding (Figure 4.8(a)) are composed of SiC particles packed together, and large pores are present in the debinded sample. After 3 cycles of PIP (Figure 4.8(b)), it is evident that the infiltrated PDC binds the particles together. Most particles are consolidated after 3 cycles of PIP, while the sample still has large openings and cracks. Finally, after 5 cycles of PIP (Figure 4.8(c)), all the visual cracks and openings are closed, and the particles are entirely bonded with PDC. This composite structure contributes to the high mechanical properties of the samples.

It can be concluded that after PIP, the porous preform is impregnated with amorphous PDC, establishing linkages between different particles. Crystalline 3C-SiC particles are bound to each other with amorphous PDC (SiCN and SiOC) from infiltration and pyrolysis of PCP.

Fabricating a porous preform will require the removal of the binder in the printed green body. However, binder burnout leaves behind a debinded sample composed of unsintered particles, which have very low mechanical strength and make an intricate component challenging to handle in subsequent processing steps.<sup>157</sup> For samples with 3D structures and overhanging

features, this binder burnout step will weaken the debinded green body (porous preform), and parts with little support or small features will break.<sup>88,158</sup> Introducing a Si-O-C<sub>x</sub> network in the debinded samples grants the debinded structures (porous preforms) enough mechanical strength to support their own weight and arrest cracking during the PIP process.

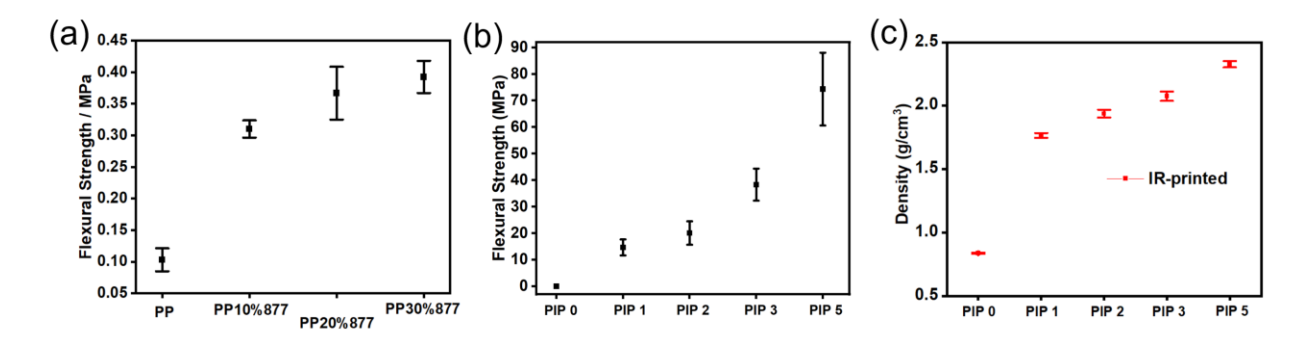


Figure 4.9. (a) Flexural strength of debinded samples with and without Si-O-C<sub>x</sub> support; (b) Flexural strength of NIR-printed *PP877* samples; (c) Density of *PP877* samples throughout different PIP cycles.

Figure 4.9(a) shows the strength of the porous preforms with and without the Si-O-C<sub>x</sub> support, where PP has no support, and PP877 has the Si-O-C<sub>x</sub> support formed during debinding. (detailed compositions are shown in Table 4.1). Amorphous Si-O-C<sub>x</sub>, formed by adding 10 wt% PCP to the printing resin, enhances the flexural strength of the porous preform by as much as 138 %. Figure 4.9(b) illustrates the relationship between the flexural strength of the samples and increased PIP cycles. Each subsequent PIP cycle increases the density and flexural strength of the Composite ceramics by filling pores and other defects. PIP increases the density of a highly porous debinded sample (PIP 0), where after 5 PIP cycles, the density of the sample reaches 2.31 g/cm<sup>3</sup> (Figure 4.9(c)). SEM micrographs (Figure 4.8) showed 5 PIP cycles completely densifying the sample. The flexural strength of the samples after 5 PIP cycles reaches 74.3  $\pm$  13.7 MPa.

Lattices can have advantages over traditional solid materials <sup>159</sup>, as these cellular structures are more efficient in achieving excellent mechanical properties with reduced weight. <sup>160</sup> Vertical stress will lead to a parallel binding force for a solid material to maintain continuous deformation during compression. This derived binding force will press the material parallelly and cause premature material failure. <sup>161</sup> Meanwhile, forces redistribute within the structure for lattice material with hollow structures, making the stress more homogeneous <sup>160</sup>. The unit cell topology, pattern design, lattice structure, and stress-relieving structures will all affect the compressive strength of the lattice. <sup>159,160</sup> While there has been research on how lattice properties affect compressive strength, there are still limited methods (e.g., finite element analysis <sup>159,160</sup>) for determining the best lattice designs.

Performance index P<sub>I</sub> can be derived from eq. 4.2:

$$\omega = LP\left(\frac{\rho}{\sigma}\right) \tag{4.2}$$

where  $\omega$ , L,  $\rho$ , and  $\sigma$  represent the sample's weight, length, density, and compressive strength. P stands for the pressure applied to the sample upon failure.

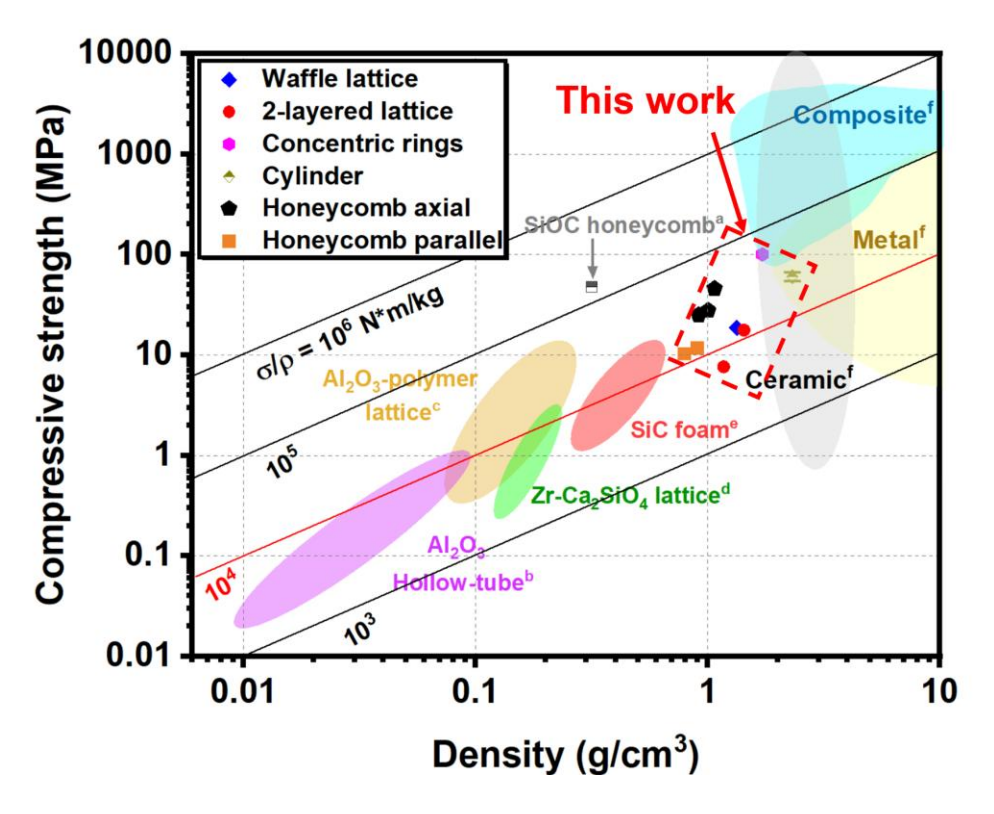


Figure 4.10. Ashby plot of compressive strength versus effective density for lattice ( $a^{50}$ ,  $b^{107}$ ,  $c^{83}$ ,  $d^{44}$ ,  $e^{162}$ ,  $f^{163}$ ).

Figure 4.10 is an Ashby plot of compressive strength versus effective density, including porous ceramic materials, as-printed lattices in this report, and solid samples. Porous ceramic materials with different densities will have their characteristic compressive strength. Lattice design will also affect the compressive strength of the samples, where different material designs with the same effective density will have different mechanical properties. A series of lattices, from honeycomb and concentric rings to layered lattices, were tested in this report, where the compressive strength of honeycomb lattices is the highest,  $32.8 \pm 11.2$  MPa. The performance index in the Ashby plot is the straight line intersecting the plot, which defines the compressive strength performance under specific densities. Figure 4.10 shows that the lattices printed in this

work have acceptable compressive performance, whereas honeycomb and concentric rings exhibit higher performance above the  $P_I$  line (highlighted line  $\sigma/\rho = 10^4$  N·m/kg).

#### 4.5. Conclusions

A new NIR thermal SLA fabrication technique has been demonstrated in this report. It is shown that with appropriate layer-by-layer adhesion and resin recoating, 2.5D-structured high-resolution samples can be made through a NIR thermal SLA printer. This technology can potentially revolutionize the additive manufacturing of PDCs, circumventing the limitations of traditional UV-based SLA. While only a few reports used thermal curing systems with NIR or IR lasers to print PCP materials, 125,164 This paper proposes a highly versatile NIR thermal SLA printer for the additive manufacturing of 2.5D structures. The printed structures showed reasonable resolution and smoothness. The introduction of the NIR laser makes it possible to process PCP with high particle loadings and UV-opaque resin compositions. It also has more potential for curing different resins like epoxy, polyurethane, PCP, and silicone.

Furthermore, introducing a percolating Si-O-C<sub>x</sub> network in the SiC matrix helps the green body keep its shape after debinding, introducing fewer defects and cracks in the samples. After 5 cycles of PIP, the samples demonstrate enhanced mechanical properties, where the flexural strength of the NIR-printed samples reaches  $74.3 \pm 13.7$  MPa. The compressive strength of honeycomb lattices was  $32.8 \pm 11.2$  MPa. The compressive strength of lattices printed with NIR laser lies above the general porous ceramic performance index line (P<sub>I</sub> =  $10^4$ ). Thus, this report's NIR thermal SLA technique effectively fabricates lightweight PDC composites with enhanced mechanical properties.

# CHAPTER 5: ADVANCING HIGH-PERFORMANCE CRYSTALLINE REACTION-BONDED PDCS THROUGH THERMAL SLA

Parts of this work are adapted from the work of Evelyn Wang and Michael A. Hickner under editing. This is the version of the article before peer review or editing as submitted by the authors for publication. The publisher is not responsible for any errors or omissions in this version of the manuscript, or any version derived from it.

#### 5.1. Abstract

This report introduces a NIR SLA method for producing highly crystalline PDCs with refined resolution. Incorporating silicon nanoparticles into the resin composition facilitates reaction bonding, neutralizing *in-situ* grown carbon from PCPs pyrolysis and yields highly crystalline ( $80.7 \pm 0.6 \%$ ) SiC-composite ceramics with large crystallites ( $4.47 \pm 1.92 \mu m$ ). This thermal SLA method allows the 3D printing of large configurations ( $30 \text{ cm}^3$  in volume, 5 mm skeleton thickness) and highly loaded resins (up to 40 wt% particles) with UV-opaque and large RI mismatch fillers, which is unachievable with traditional UV SLA printing. This approach enhances mechanical properties ( $89.6 \pm 32.3 \text{ MPa}$ ) and eliminates carbon impurities, suitable for applications requiring high crystallinity and performance. The optimized printing system equipped with active cooling methods helps improve the thermal printing resolution, enabling precise manipulation up to sub-millimeter level resolution ( $0.72 \pm 0.03 \text{ mm}$ ). These results advance the PDC additive manufacturing process, optimizing for carbon-free, highly crystalline SiC-based composite ceramics.

## 5.2. Introduction

The growing demand for developing advanced material systems in modern aerospace<sup>165</sup>, semiconductor<sup>166</sup>, wastewater treatment<sup>167</sup>, and medical applications<sup>167</sup> has placed stringent requirements on material properties. As a non-oxide ceramic, SiC is an important technical ceramic due to its excellent mechanical, thermal, and optical properties 165. SiC-based composite ceramics have gained attraction in various applications due to their superior strength, high thermal stability, oxidation resistance, and hardness<sup>168</sup>. While shaping these types of materials with traditional ceramic processing is difficult, processing methods afforded by PCPs<sup>169</sup> has ushered new opportunities for fabricating SiC and SiC composite ceramic components, making it possible to shape ceramics into pre-defined structures with tunable properties. <sup>170</sup> There are three steps in PCP processing: shaping, crosslinking, and ceramic transformation<sup>171</sup>. During the shaping stage, the polymeric nature of the PCPs enables different shaping techniques, such as molding and AM. Crosslinking during the second stage ensures the parts retain their shape during pyrolysis, increasing the overall ceramic yield. Finally, the highly crosslinked PCPs undergo a pyrolysis process, where amorphous ceramics are obtained at lower temperature <sup>172</sup> (800 – 1200 °C) pyrolysis, while annealing (> 1400 °C) of the samples facilitates the phase separation and crystallization of the PDC parts<sup>173</sup>.

3D printing has introduced new potential for the fabrication of PDC-based components. FFF, SLA, DLP, two-photon polymerization (TPP), SLS, and LOM<sup>171</sup> have all been demonstrated with PCP materials. Among these techniques, SLA and DLP<sup>174</sup> stand out as the most popular methods of fabricating 3D PCP parts due to their fast prototyping of high-fidelity,

accurate parts. Several studies have reported SLA/DLP of PDC parts with high resolution, including SiOC, SiC, and SiO<sub>2</sub> components, demonstrated in 3D structures/lattices<sup>175–178</sup>.

3D printing of monolithic ceramics with large critical dimensions has been a challenge for the use of PCPs in AM<sup>179</sup>. The high shrinkage during the PCP pyrolysis stage will often lead to fracture of the samples<sup>179</sup>, and samples that survive pyrolysis tend to have low ceramic yield and low density. During resin pyrolysis, the gas released from the polymer will lead to porosities in the matrix, and the gas-releasing channels in the samples will cause uneven shrinkage of the samples during pyrolysis, which leads to sample curling<sup>180</sup>. Fillers and additives are necessary to maintain the high density and fidelity of ceramic parts from PCPs<sup>176</sup>. The significant shrinkage originates from the fact that when turning polymers into ceramics, the materials condense from low-density polymers (around 1 g/cm<sup>3</sup>) into high-density ceramics (2-3 g/cm<sup>3</sup>)<sup>174</sup>. This inevitable shrinkage will lead to cracking and deformation of the samples, limiting the scale of the printed PDC parts<sup>175</sup>. Many methods have been developed to combat shrinkage and porosity in PDCs, including PIP, melt infiltration, CVI, and reaction bonding<sup>167,181</sup>.

Due to their limited compositional range, organosilicon PCPs suffer from low crystallinity and excess carbon residuals after pyrolysis. The excess carbon originates from PCPs and crosslinkers in the green body. Due to the difficulty of producing and maintaining stoichiometry in the precursor material and pyrolysis phase of the process, residual carbon nearly always remains in the samples<sup>179</sup>. The *in-situ* grown carbon<sup>173</sup> in PDCs is detrimental<sup>182</sup> in several ways: carbon is susceptible to oxidation (at temperatures as low as 450 °C), which significantly lowers the oxidation resistance of PDCs<sup>173</sup>; carbon facilitates the decomposition of PDCs by carbothermal reduction<sup>183</sup>, and can form nanodomains or clusters, which act as

secondary phases/boundaries that lowers the strength of PDCs<sup>184</sup>. For example, silicon oxycarbide (Si<sub>1-x-y</sub>O<sub>x</sub>C<sub>y</sub>) or silica (SiO<sub>2</sub>) do not co-exist with carbon inclusions at steady-state operation because these ceramics will decompose at elevated temperatures (1500 °C) through carbothermal reduction into gaseous species (SiO and CO) <sup>185</sup>.

Various processing strategies have been pursued to minimize residual carbon in PDCs.

One strategy is adding crystalline ceramic particles in the resin mixture during 3D printing<sup>186</sup>, yielding particle-based composite ceramics<sup>187</sup>. In this approach, the crystalline ceramic particles do not melt or reorganize during pyrolysis, which prevents shrinkage of the samples and yields a porous body after firing<sup>188</sup>. The second tactic for limiting carbon in PDCs is carbothermal reduction<sup>189</sup>, which generates SiC by eliminating excess oxygen and carbon in the samples at high temperature<sup>185</sup>. However, this method gives lower ceramic yield and leaves excess oxygen and carbon in the sample, as it is challenging to tune the atom stoichiometry throughout the entire pyrolysis process <sup>185</sup>.

Another way of fabricating dense SiC involves liquid silicon infiltration (LSI), which infiltrates silicon into the pores/channels of a carbon matrix to yield a dense siliconized SiC part<sup>190</sup>. This reaction bonding method can provide an energy-efficient pathway for obtaining crystalline SiC, as the traditional re-crystallization method will require temperatures up to 2200 °C<sup>182</sup>. During a typical LSI process, a porous carbon/carbon fiber matrix is infiltrated with liquid silicon by capillary force to siliconize the carbon-rich body<sup>191</sup>. However, this method has several drawbacks: (1) liquid silicon erodes the SiC/C fibers<sup>192</sup> which lowers the overall strength of the composites; (2) while silicon wets carbon and infiltrates into the carbon body rapidly, the infiltration efficiency<sup>193</sup> significantly lowers after SiC layers formed through reaction bonding, as

dissolution-growth of SiC crystals dominates; (3) control over the carbon microstructures is vital for LSI, as high porosity will lead to highly siliconized SiC that is easily eroded and fractured, while low porosity in the carbon preform will lead to choking<sup>190</sup> of the infiltrating liquid silicon that prevent further siliconization and leaves large carbon-rich regions<sup>194</sup>. Therefore, while LSI removes the excess carbon in the preform and bridges them together by reaction bonding and dissolution-growth mechanisms, it has strict requirements on the microstructure of the carbon preform and infiltration conditions<sup>195</sup>.

This work aims to mitigate the issues inherent in 3D printing of SiC particle-based composite ceramics composite ceramics using a novel in-situ reaction bonding method combined with NIR thermal SLA technology, which makes it possible 179 to print silicon-based, highly loaded resins. Additionally, active cooling was adopted during the thermal SLA process to improve printing resolution. This report combines the advantages of reaction bonding and PCPs, utilizing silicon nanoparticles as active/meltable fillers to react and bond excess carbon from PCP pyrolysis 174 to yield highly crystalline SiC-based composite ceramics.

# 5.3. Experimental

## 5.3.1. Materials

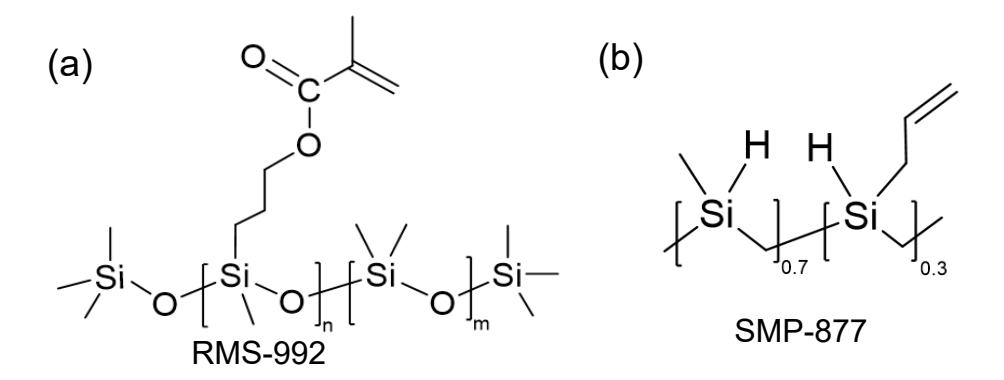


Figure 5.1. Chemical structure of (a) RMS-992; (b) SMP-877 resin.

The starting materials used in this work are shown in Figure 5.1, where acrylate-modified siloxane RMS-992 ((methacryloxypropyl)methylsiloxane, 95 - 100%, Gelest, Morrisville, PA) was selected as both crosslinker and PCP, SMP-877 (Starfire Systems, Glenville, NY) resin was chosen as the main PCP, and dicumyl peroxide (Sigma-Aldrich, 98%, St. Louis, MO) was the thermal initiator. Silicon nanoparticles (500 nm, US nano, Houston, TX) were homogeneously blended into the resins with a FlackTek Speed Mixer (Greenville, SC, DAC 1200-300 VAC) with a two-step mixing procedure. First, the resin and nanoparticles are mixed under ambient pressure with a spinning speed of 1000 RPM for 1 min. The mixture was then mixed under a 6.7 kPa vacuum at a speed of 2000 RPM for 3 min. The resin compositions are listed in Table 5.2.

The pyrolysis procedures of all the samples were identical, where the furnace conditions and steps are detailed in Table 5.1.

Table 5.1. Tube furnace pyrolysis procedure.

Seg.	1	2	3	4	5	6	7	8	9	10
Option	R	D	R	D	R	D	R	D	R	R
Temp.	300	0.5 h	500	30	600	30	1500	2 h	300	RT
	°C		°C	min	°C	min	°C		°C	
Ramp	5 °C		2 °C		1 °C		1 °C		1 °C	2 °C
Rate	/min		/min		/min		/min		/min	/min

Note: R stands for ramp, D means dwell.

Three vacuum-purge cycles were applied before the pyrolysis procedure to eliminate as much oxygen in the tube furnace as possible. During a typical vacuum-purge cycle, the tube furnace was first connected to the vacuum, lowering the pressure to 5.0 kPa. Subsequently, the

furnace was disconnected from the vacuum and purged with ultra-high purity (UHP) argon. This practice ensures the pyrolysis procedure is conducted in an oxygen-free environment.

During the pyrolysis process, the argon flow was kept at 50 cm<sup>3</sup>/min to maintain positive pressure in the tube furnace chamber, where the inert gas flow can carry away the combustion gas from polymer decomposition and reactions.

Table 5.2. Resin compositions.

Components	GRR	MSR	SRR	877 RMS	877
RMS-992 / wt%	34.88	32.39	29.91	49.75	0
SMP-877 / wt%	34.88	32.39	29.91	49.75	99.01
Dicumyl peroxide / wt%	0.35	0.32	0.30	0.50	0.99
Silicon (500 nm) / wt%	29.90	34.89	39.88	0	0

Note: GRR: graphite-rich resin (lowest silicon content); MSR: medium silicon resin (medium silicon content); SRR: silicon-rich resin (high silicon content); 877 RMS: resin composition without silicon content; 877: pure PCP without crosslinkers and silicon.

# 5.3.2. NIR thermal printer setup

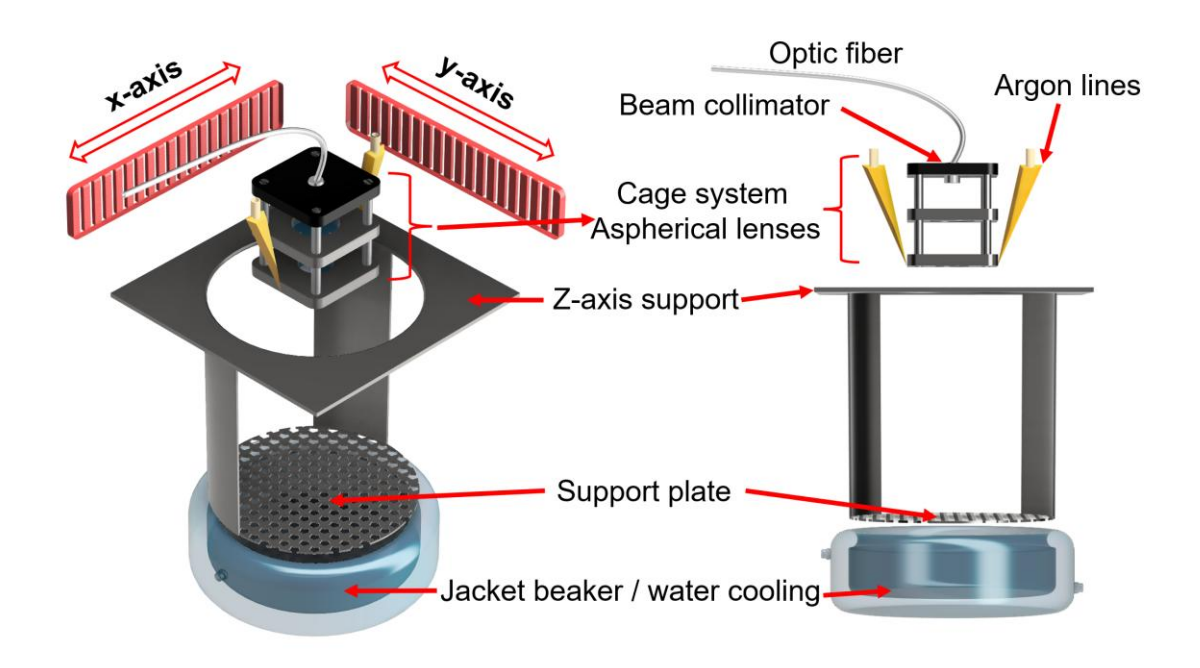


Figure 5.2. 3D view and front view of the NIR thermal SLA printer.

In the NIR thermal SLA printer, an 808 nm NIR laser (Lumics Inc., Berlin, Germany) is guided with an optic fiber and then integrated into an optical cage system with two aspherical lenses and a beam collimator (Figure 5.2, Thorlabs Inc., Newton, NJ). The two aspherical lenses refocus the collimated beam onto the resin surface. The optical cage system is mounted on an x-y gantry system, allowing the NIR laser to move and project localized thermal energy onto specific planar coordinates. Two separate tactics are employed for cooling during printing to minimize overcure due to thermal diffusion. Two lines of flowing argon connected to the optical cage provide targeted forced convection, rapidly cooling the resin surface. The resin vat is also placed in a water-cooled jacketed beaker maintained at 25 °C, providing coolant circulation that rapidly removes excess heat from the resin pool area (which will be discussed in Chapter 7). After the printing of each layer, the z-axis support moves down, submerging the support plate into the

resin pool to create new layers. This layer-by-layer process constructs the 3D structures from designed models onto the support plate.

### 5.3.3. Characterization

All the characterization methods are the same as mentioned in section 3.3.6, except for SEM, Raman, mechanical testing, and thermal measurements. SEM (Tescan Mira, Brno, Czech Republic) was used to observe the pyrolyzed samples' microstructure and capture micrographs. Raman spectroscopy (Horiba LabRAM ARAMIS, Kyoto, Japan) with a 532 nm laser and 5x objective is used for conducting Raman analysis on pyrolyzed samples. Mechanical properties were obtained with United Testing Systems (UTS, Warren, MI) SFM-20 load frame equipped with a 3-point bend fixture for flexural strength measurement (ASTM C1341-13). Thermal images are taken with a thermal camera (Teledyne FLIR E5, Wilsonville, OR). All the crystallite sizes are measured using the CCD (circumscribed circle diameter) method from SEM micrographs and analyzed with ImageJ software.

## 5.4. Results and Discussion

This work demonstrates a method that utilizes Si reaction bonding to react excess graphitic carbon species with silicon in composite ceramics and convert these materials into a crystalline SiC phase. Instead of crystalline ceramic particles, silicon metal nanoparticles (with some surface oxide) are added to the resin before 3D printing. During the first heating stage (below the melting of silicon nanoparticles), the PCPs decompose and transform into ceramics with residual carbon, where most of the polymeric decomposition and shrinkage occurs during this stage<sup>196</sup>. During the second stage, the embedded silicon nanoparticles start to melt in the samples, and the residual carbon will react and bond with the melting silicon to yield SiC<sup>182</sup>.

Apart from this, the melting silicon will act as a binder that bridges the crystallites in the samples. As an active filler<sup>197</sup>, silicon will react and bond with the surrounding carbon and yield β-SiC; as a meltable filler, silicon will melt to fill the existing pores/channels and relieve the stress in the pyrolyzed PDCs<sup>171</sup>. This *in-situ* reaction bonding process can yield a dense 3D-printed sample with high crystallinity and large crystallites. By tuning the carbon-to-silicon ratio, SiC-based composite ceramics were demonstrated with a minimal amount of excess carbon/silicon in the pyrolyzed samples, which showed excellent mechanical properties.

Additively manufactured components were fabricated from NIR thermal SLA using the steps described in the NIR thermal SLA experimental setup. 3D-printed configurations with overhang structures were constructed and subsequently pyrolyzed into ceramics, where the dimensional accuracy and structural integrity were maintained after firing.

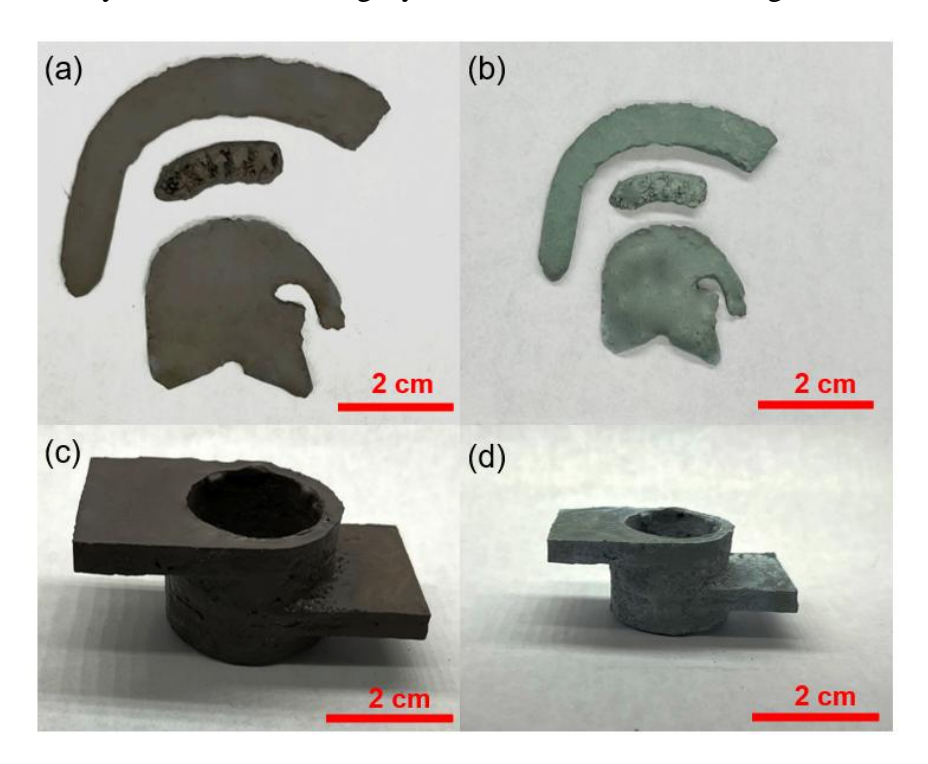


Figure 5.3. (a, c) As-printed 2D and 3D structures before pyrolysis; (b, d) the samples after pyrolysis.

The resolution of the printed components was  $0.72 \pm 0.03$  mm, which was achieved with active cooling methods during printing. The print size in Figure 5.3(d) is about 30 cm<sup>3</sup> (53 mm × 27 mm × 21 mm), and the wall thickness is 5 mm. The NIR-printed samples were transferred into a vented oven for post-curing at 200 °C for 30 min, which is the same curing procedure for oven-cured samples. The post-cured green bodies were transferred to a tube furnace and pyrolyzed under conditions listed in Table 5.1.

XRD analysis was conducted on samples with different silicon loadings (*GRR*, *MSR*, and *SRR*, Figure 5.5). Where the crystalline phases (Figure 5.5), crystallinity (Figure 5.4, eq. 5.2), and crystallite sizes (Scherrer equation<sup>166</sup>, eq. 5.1) were analyzed and revealed. All the XRD samples were pyrolyzed using the procedure mentioned in Table 5.1.

The crystallite sizes were calculated from Scherrer equation, eq. 5.1, where pyrolyzed 877 has an average size of  $5.86 \pm 0.03$  nm and pyrolyzed 877 RMS has an average size of  $6.04 \pm 0.03$  nm.

$$D = \frac{k\lambda}{\beta\cos\theta} \tag{5.1}$$

Where D is the average size of the crystallites, k stands for the shape factor (which was chosen as 0.9 in this report),  $\lambda$  represents the wavelength of X-rays,  $\beta$  denotes the full width at half maximum (FWHM), and  $\theta$  means Bragg angle.

The crystallinity indexes<sup>198</sup> of the pyrolyzed samples are calculated from eq. 5.2:

$$I = \frac{I_c}{I_c + I_a} \times 100\% \tag{5.2}$$

where I represents the crystallinity index,  $I_c$  stands for the percentage of crystalline materials, and  $I_a$  is the percentage of amorphous materials. The calculated crystallinity indexes are plotted in Figure 5.4.

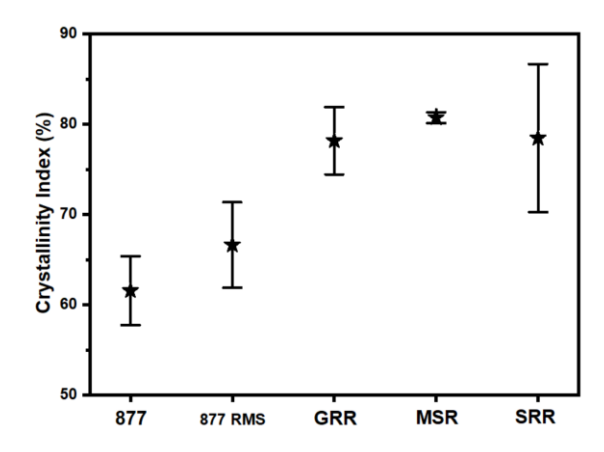


Figure 5.4. Crystallinity indexes of the pyrolyzed samples.

While Eq. 5.1 only considers the phases shown in the XRD patterns, graphitic carbon peaks do not show in the XRD pattern. As a result, the crystallinity of samples in Figure 5.4 only demonstrates the amount of material that crystallizes among all the non-graphitic carbon species. The crystallinity index reaches  $80.7 \pm 0.6$  % for pyrolyzed MSR.

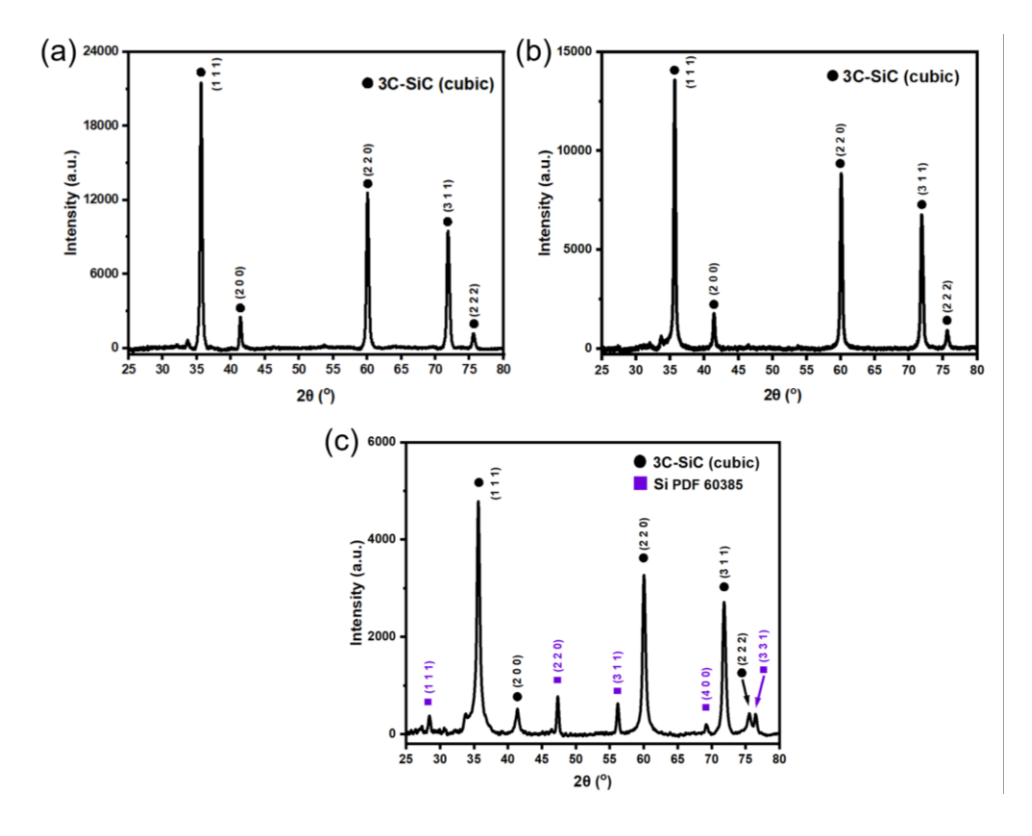


Figure 5.5. XRD pattern of pyrolyzed (a) GRR, (b) MSR, and (c) SRR.

The XRD pattern of pyrolyzed *GRR* and *MSR* show peaks at identical locations, where peaks at 35.7°, 41.4°, 60.1°, 71.9°, and 75.6° correspond to (1 1 1), (2 0 0), (2 2 0), (3 1 1) and (2 2 2) planes for cubic 3C-SiC<sup>199</sup>, respectively. The XRD pattern of the pyrolyzed *SRR* sample show the same cubic 3C-SiC peaks, with additional peaks at 24.9°, 47.3°, 56.2°, 69.2°, and 76.4° are (1 1 1), (2 2 0), (3 1 1), (4 0 0) and (3 3 1) silicon planes (PDF 60385).

The XRD pattern shown in Figure 5.5 demonstrate that a higher amount of silicon nanoparticles in the resin composition will tune the samples from a carbon-rich ceramic to a silicon-rich composite. While the XRD of PCPs without silicon addition does not show clear peaks, and limited crystallinity (61.6 % to 66.6 %)/crystallite sizes (5.86  $\pm$  0.03 nm for pyrolyzed 877 and 6.04  $\pm$  0.03 nm for pyrolyzed 877 RMS). The results from Figure 5.5 demonstrate that adding nanosized silicon will facilitate the growth of crystalline 3C-SiC and increase the crystallinity (80.7 % for pyrolyzed MSR).

Raman spectroscopy was performed on the same set of samples with silicon (*GRR*, *MSR*, and *SRR*, Figure 5.6) to obtain additional structural information from the pyrolyzed samples. All the Raman samples were pyrolyzed under the same procedure detailed in Table 5.1.

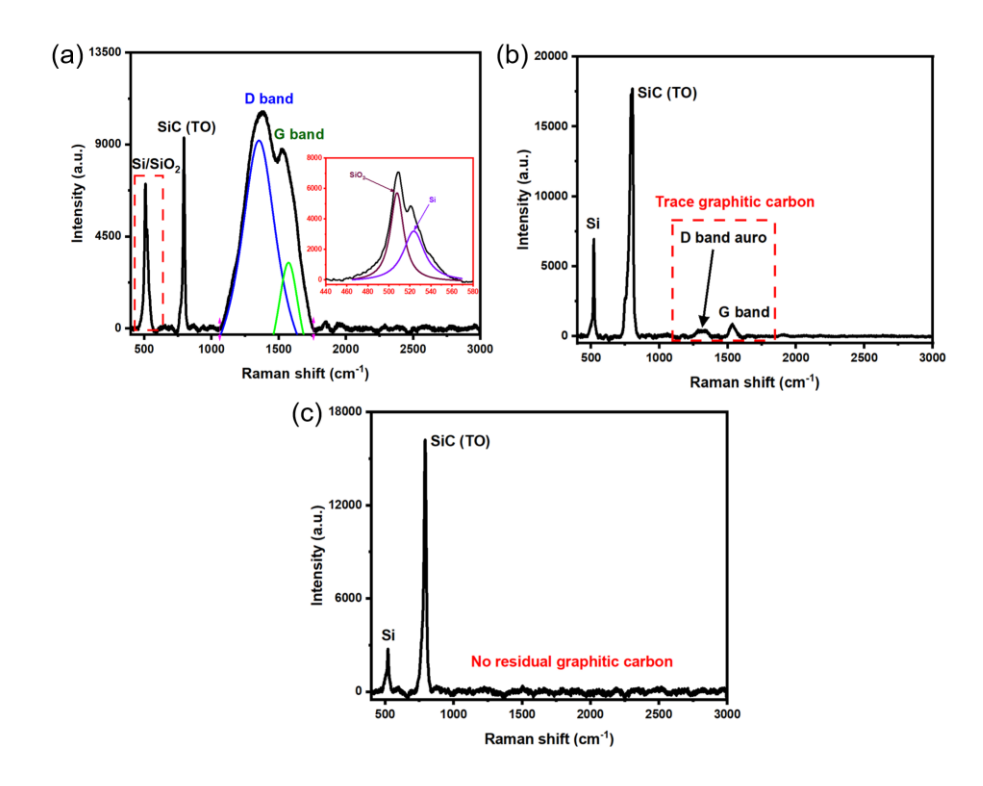


Figure 5.6. The Raman spectrum of pyrolyzed (a) GRR, (b) MSR, and (c) SRR.

From Figure 5.6(a), the peaks at 508 cm<sup>-1</sup>, 524 cm<sup>-1</sup>, 795 cm<sup>-1</sup>, 1355 cm<sup>-1</sup>, and 1571 cm<sup>-1</sup> correspond to SiO<sub>2</sub>, Si, SiC (transverse optical mode, TO), D, and G band (deconvolution of the peaks are performed with Gaussian fitting). Figure 5.6(b) shows that the peaks at 520 cm<sup>-1</sup>, 793 cm<sup>-1</sup>, 1320 cm<sup>-1</sup>, and 1535 cm<sup>-1</sup> are Si, SiC (TO)<sup>194</sup>, D band auro, and G band, respectively. Finally, the 520 cm<sup>-1</sup> and 792 cm<sup>-1</sup> peaks from Figure 5.6(c) demonstrate only Si and SiC (TO mode) present in the pyrolyzed *SRR* samples. This data shows that the pyrolyzed sample transforms from a graphitic carbon-rich ceramic composite to a silicon-rich siliconized SiC ceramic when increasing the amount of silicon nanoparticles in the resin composition – where *GRR* yields a graphitic carbon-rich body after pyrolysis, *MSR* gives a sample with a small amount of graphite and silicon, and *SRR* generates a body with excess silicon. On the contrary, Raman spectra of samples without silicon addition after pyrolysis do not show any characteristic

peaks except for graphitic carbon, which acts as secondary phases in the PDCs that lower the purity and mechanical properties of PDCs<sup>173</sup>. XPS analysis was conducted on all the samples with and without silicon inclusion to complement the results from XRD and Raman; XPS carbon spectra and silicon spectra were analyzed to show the evolution of carbon and silicon species in the samples. The XPS spectra of 877 RMS and MSR are shown in Figure 5.7, while the rest of the spectra (877, GRR, SSR) are displayed in Figure 5.8. All samples for XPS analysis are pyrolyzed using the same procedure listed in Table 5.1.

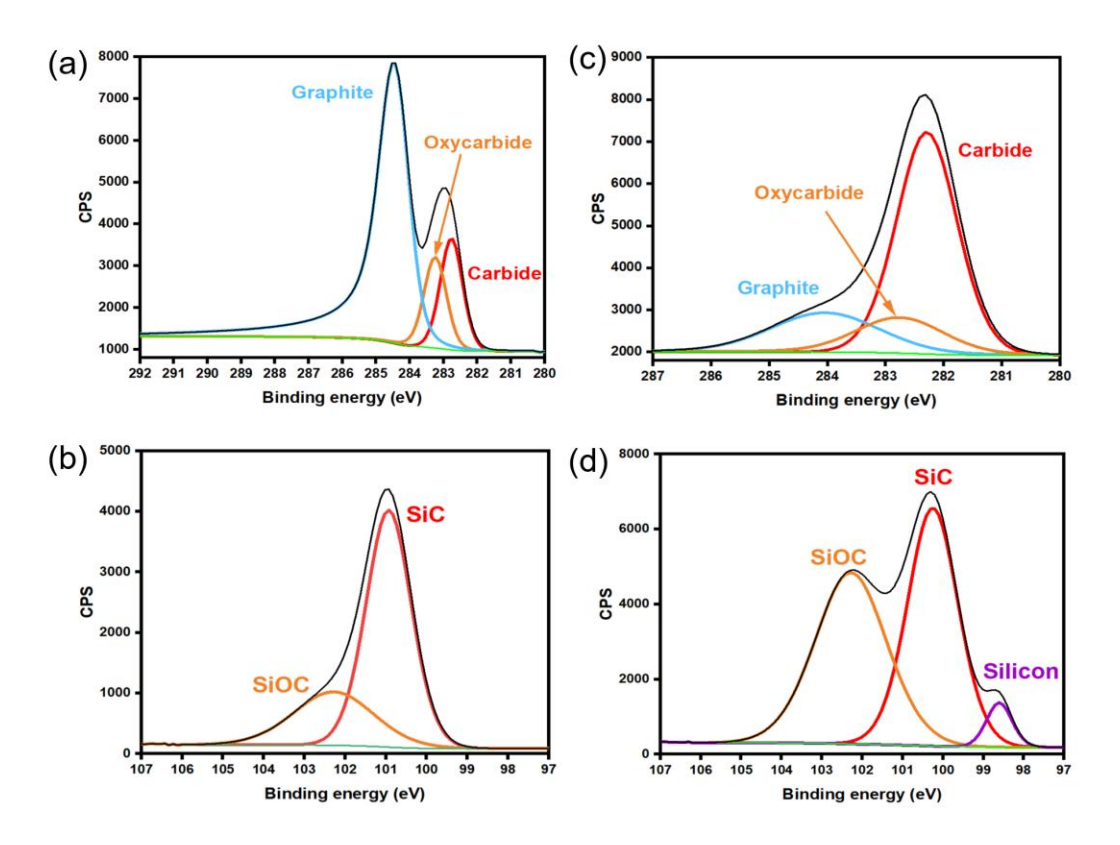


Figure 5.7. XPS spectra of pyrolyzed (a) 877 RMS C 1s; (b) 877 RMS Si 2p; (c) MSR C 1s; (d)

MSR Si 2p.

The deconvolution of the XPS peaks was performed with Gaussian (the rest of the peaks) and Lorentzian fitting (graphite and oxycarbide in C 1s). For C 1s spectra, Figure 5.7(a) and (c)

show three peaks at the same position with different peak intensities, where the peaks at 282.3 - 282.7 eV, 282.8 - 283.2 eV, and 284.1 - 284.4 eV represent carbide, oxycarbide, and graphite, respectively. For Si 2p spectra, Figure 5.7(b) and (d) share two identical peaks at 102.3 eV (SiOC) and 100.2 - 100.9 eV (SiC), while Figure 5.7(d) has an additional silicon peak at 98.7 eV. It can be concluded from Figure 5.7(a, b) that printing resin without any silicon nanoparticles (877 RMS) yields a large amount of graphitic carbon, while there is only a minimal amount of SiC with a small amount of SiOC in the pyrolyzed samples. For MSR resin after pyrolysis, Figure 5.7(b) and (d) illustrate that a substantial number of carbide species are growing in the samples, while graphitic carbon is largely diminished in the pyrolyzed samples.

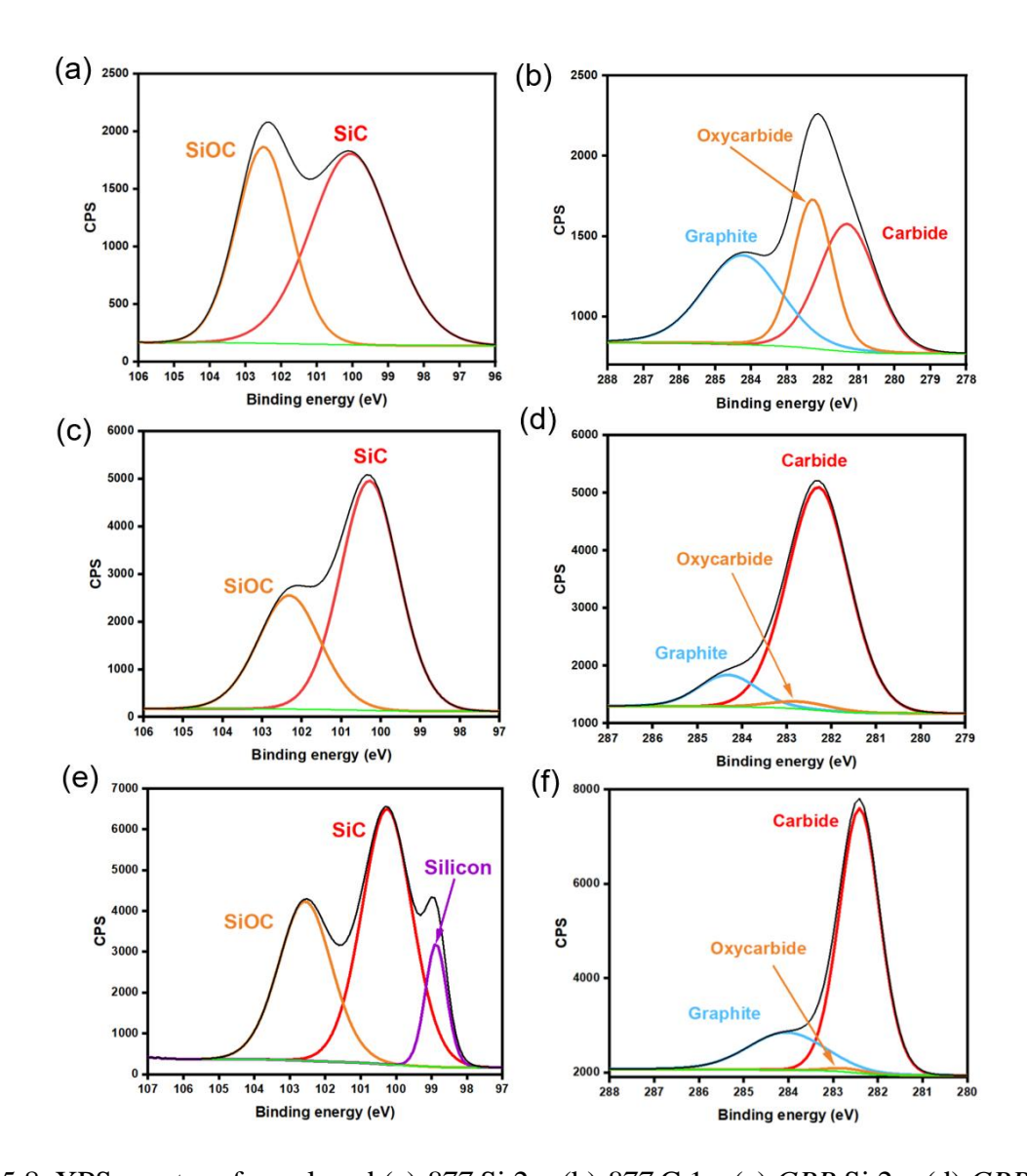


Figure 5.8. XPS spectra of pyrolyzed (a) 877 Si 2p; (b) 877 C 1s; (c) *GRR* Si 2p; (d) *GRR* C 1s; (e) *SRR* Si 2p; (f) *SRR* C 1s.

Figure 5.8(a, c, e) share the same two peaks – SiOC at around 102.3 eV - 102.4 eV and SiC at around 100.1 eV - 100.3 eV. There is an additional silicon peak at 98.8 eV, as shown in Figure 5.8(e). Figure 5.8(b, d, f) features all the same peaks with different abundance – graphite (C=C) peak at around 284.1 eV - 284.3 eV; oxycarbide peak at around 282.8 eV - 283.3 eV; and carbide peak at around 281.3 eV - 282.9 eV.

Figure 5.8(b) reveals a high concentration of graphitic carbon species in the pyrolyzed pure polycarbosilanes (877). Furthermore, Figures 5.8(c, e) and Figure 5.8(d) demonstrate a correlation between increasing silicon content in the samples (from *GRR* to *SRR*) and the amount of residual silicon present after pyrolysis. Furthermore, when compared to Figures 5.8(b), Figures 5.8(d,f) and Figure 5.8(c) demonstrate that the addition of silicon effectively reduces the amount of graphitic carbon and increases the amount of carbide in the sample.

When combined with the results from XPS data, a conclusion can be drawn that PCPs without silicon addition will yield a graphitic carbon-rich body with a limited amount of SiC and SiOC after pyrolysis. Meanwhile, crosslinkers (RMS-992) in the resin (877 RMS) will lead to more carbon residual in the pyrolyzed green body. All three characterization methods (Raman, XRD, and XPS) point to the same conclusion that with silicon inclusion in the PCPs, SiC will grow at the cost of excess *in-situ* grown carbon species in the pyrolyzed samples. More silicon inclusion in PCPs will result in residual silicon being left behind in the final composite ceramic (Si-SiC). The pyrolyzed *GRR*, *MSR*, and *SRR* are mainly composed of SiC, with a small amount of SiOC and residual carbon/silicon. The pyrolyzed *MSR* sample has the least residual free graphitic carbon and excess silicon among the three resin compositions.

SEM micrographs of all the samples with and without silicon addition are displayed in Figure 5.9, where the microstructures and crystalline structures are clearly visualized. These microstructures reveal the evolution of graphitic carbon and reaction-bonded SiC, as evidenced by the changes shown in the micrographs. All the SEM samples are pyrolyzed using the same procedure discussed in Table 5.1.

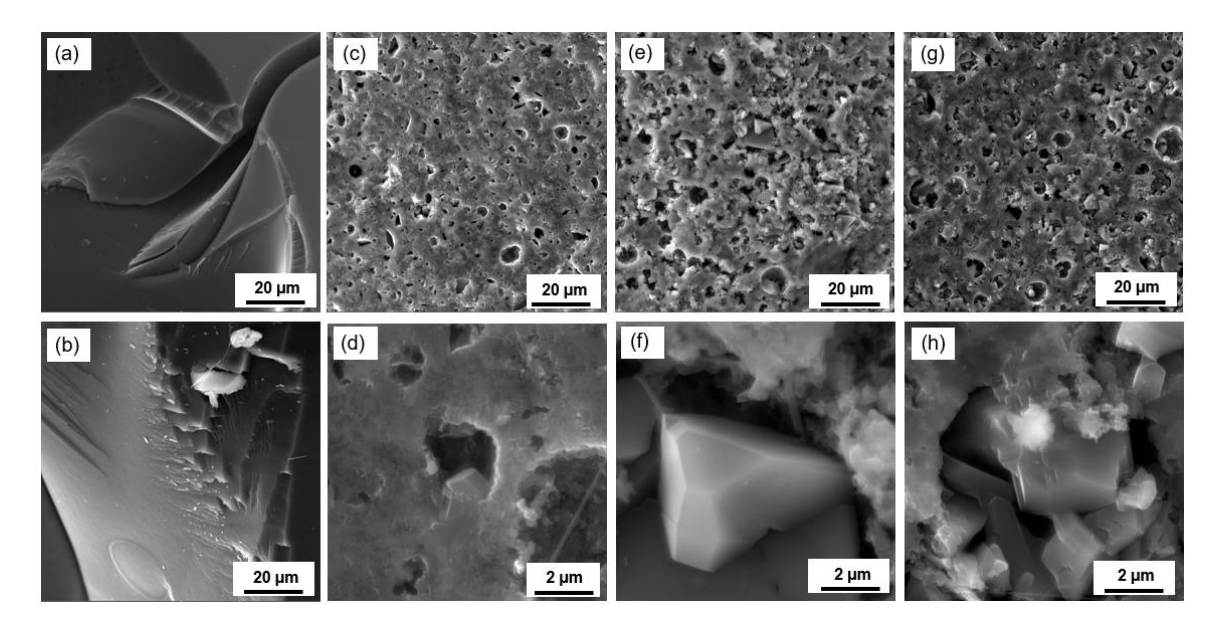


Figure 5.9. SEM micrographs of pyrolyzed (a) 877; (b) 877 RMS; (c, d) GRR; (e,f) MSR; (g,h) SRR.

From the SEM micrographs, detailed microscopic information about pyrolyzed samples can be extracted; Figure 5.9(a,b) shows no visible crystallites in the pyrolyzed PDCs, indicating that the crystallites are extremely small. This observation is consistent with the crystallite size analysis presented in Figure 5.4, where calculations based on the Scherrer equation  $^{166}$  (eq. 5.1) confirm the presence of only nanosized crystallites in the pyrolyzed PCPs without any fillers or particles. It can be concluded from Figure 5.9(d,f,h) that crystallites grow with silicon nanoparticles added to the resin compositions. These SEM micrographs demonstrate that when there is an excess amount of graphitic carbon in the sample, only small crystals  $(1.97 \pm 1.32 \ \mu m)$  with low abundance are grown in the pyrolyzed *GRR*. In contrast, many larger crystals are grown in samples with more silicon content  $-4.47 \pm 1.92 \ \mu m$  for *MSR* and  $4.17 \pm 1.72 \ \mu m$  for *SRR* (calculated with CCD, ImageJ).

From Figure 5.9(c, e, g), it can be concluded that after pyrolysis, the samples still have some enclosed pores. However, the melted silicon connects all the pores and crystallites because the silicon in the samples melts and reacts with the surrounding graphitic carbon. The SEM micrographs demonstrate that silicon acts as an excellent active/meltable filler that bonds with excess carbon and flows into pores, which relieves stress<sup>197</sup>. It is clearly shown that the SiC crystals are tightly bonded into a composite ceramic structure, contributing to the integrity and strength of the sample.

The flexural strength of the samples with different silicon loading was tested with three-point bending. The flexural strength is displayed in Figure 5.10, and the Weibull distribution of the strength is plotted in Figure 5.11. The clustering and distribution of different samples' strengths are clearly visualized. All the mechanical testing samples were pyrolyzed using the procedure detailed in Table 5.1.

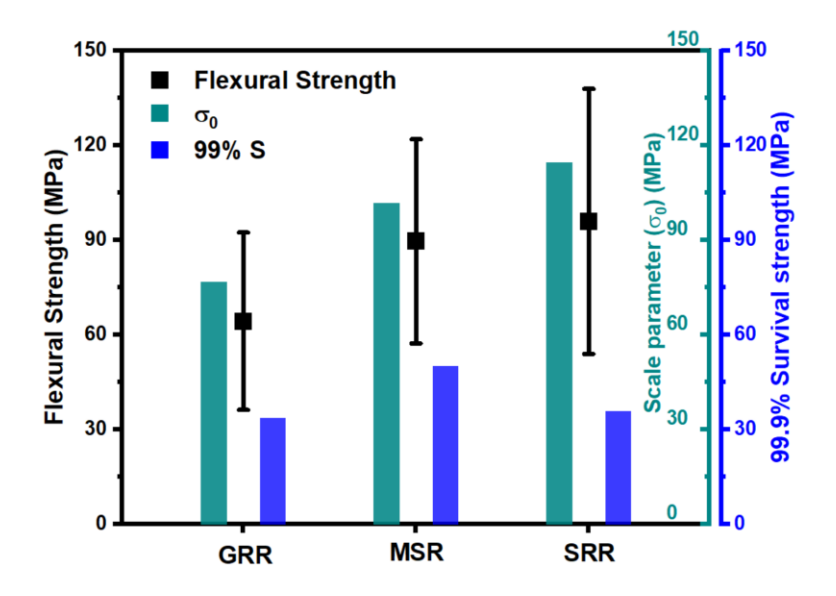


Figure 5.10. Flexural strengths of NIR-printed samples with different silicon loadings. High densities  $(2.43 \pm 0.05 \text{ to } 2.55 \pm 0.10 \text{ g/cm}^3)$  and high crystallinity  $(78.18 \pm 3.72 \text{ to } 80.74 \pm 0.61 \%)$  in the final samples contribute to the enhanced mechanical performance of these

materials. The density reported here is close to that reported for high temperature (2330 – 2430 °C) LSI parts (2.62 - 2.82 g/cm<sup>3</sup>) <sup>200</sup>.

Figure 5.11 shows a Weibull distribution plot for the samples' flexural strengths, which implements the data in Figure 5.10. The clustering and distribution of different samples are visualized in Figure 5.11, where the Weibull modulus and survival probability can be determined. All the samples for flexural strength testing were pyrolyzed using the same procedure discussed in Table 5.1.

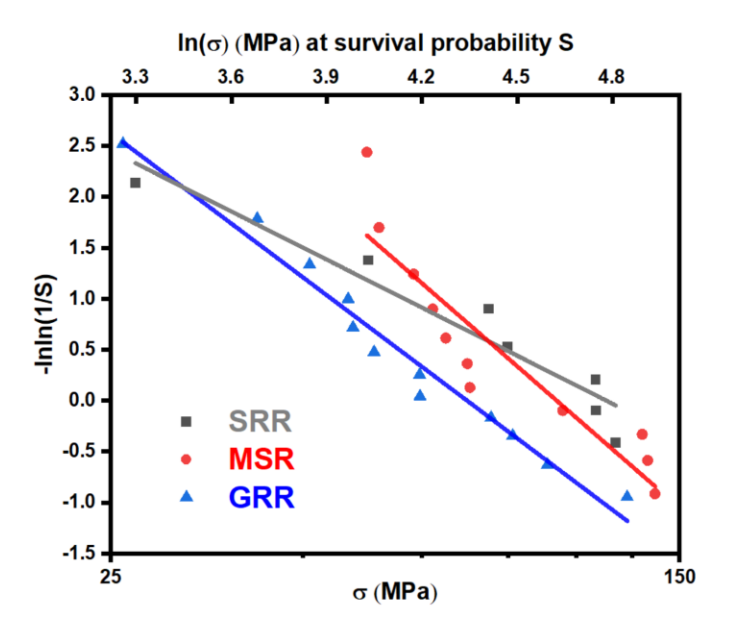


Figure 5.11. Weibull distribution fitting of pyrolyzed NIR-printed samples.

Figure 5.11 shows the Weibull distribution fitting for the flexural strength of pyrolyzed samples with different silicon loadings (eq. 5.3 and eq. 5.4).

$$\ln \ln \frac{1}{S} = m \ln \sigma - m \ln \sigma_0 \tag{5.3}$$

$$S = \exp\left[-\left(\frac{\sigma}{\sigma_0}\right)^{m}\right] \tag{5.4}$$

Where S is the survival probability, m stands for the shape factor of Weibull distribution,  $\sigma$  represents the failure stress, and  $\sigma_0$  denotes a normalizing factor. The fitted equation for Figure 5.11 (a) is y = -2.3495x + 10.1964, Figure 5.11 (b) is y = -2.7157x + 12.5569, Figure 5.11 (c) is y = -1.661x + 7.8741, from which the Weibull modulus m and scale parameter (characteristic life)  $\sigma_0$  can be extracted.

The flexural strength of the samples is measured with three-point bending and plotted in Figure 5.10. It can be concluded that pyrolyzed *GRR* has the lowest flexural strength (64.3  $\pm$  28.1 MPa) among all the samples tested, whereas pyrolyzed *MSR* samples show a flexural strength of 89.6  $\pm$  32.3 MPa and pyrolyzed *SRR* samples demonstrate strength of 95.9  $\pm$  42.0 MPa. The clustering and strength distribution is easily visualized in Figure 5.11, which shows that the Weibull moduli of the pyrolyzed *GRR*, *MSR*, and *SRR* are 2.350 (mg), 2.716 (mm), and 1.661 (ms), individually. Since larger Weibull modulus m denotes a sharper distribution, SRR yields ceramics with a wider distribution of mechanical properties and, therefore, are less reliable for practical application (Figure S6). Pyrolyzed *MSR* samples have a slightly lower characteristic life  $\sigma_0$  (101.9 MPa, 36.8% survival probability) but a much higher 99.9% survival strength (50.0 MPa, 99.9% survival probability), indicating that pyrolyzed *MSR* samples have a narrower distribution and are more reliable under loads.

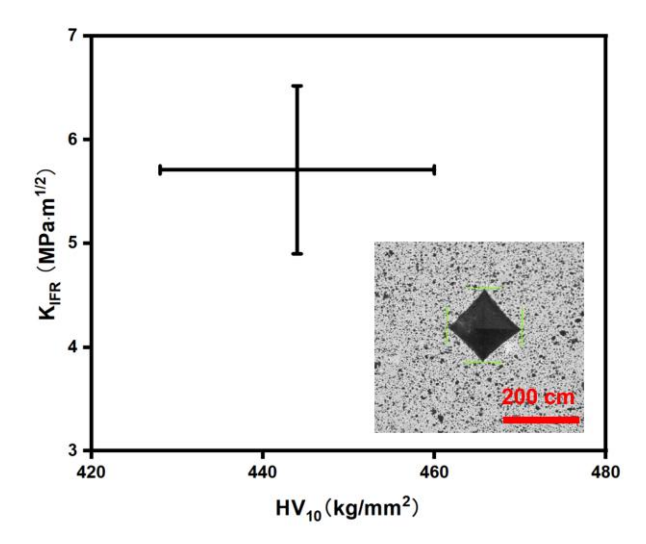


Figure 5.12. Flexural strengths of NIR-printed samples with different silicon loadings.

Vickers microindentation (Qness Q60 A+, QATM, Austria) was employed on the polished cross-sections of mounted bar samples. An applied load of 10 kgf (n = 5 per sample) was utilized to measure these ceramic materials' hardness and fracture resistance. The indentation fracture toughness (K<sub>IFR</sub>) was calculated using the eq. 5.5 given by Anstis et al. <sup>134,135</sup> and the assumed elastic modulus of silicon carbide (Voigt-Reuss-Hill average, 434 GPa<sup>33</sup>). The crack lengths were measured using the average of five parallel lines (as described in Quinn's method <sup>136</sup>) for horizontal and vertical diagonals with image analysis software (ImageJ, Figure 5.12).

Fracture toughness Kifr is given by eq. 5.5:

$$K_{IFR} = 0.016 \sqrt{\frac{E}{H}} \frac{P}{c^{3/2}}$$
 (5.5)

where E and H are the elastic modulus and hardness of the sample, respectively, P is the peak load, and c is the crack length.

## 5.5. Conclusions

This report presents a thermal SLA method for constructing PCP resins with high RI mismatch -1.4 to 1.6 for polymers,  $^{201}$  and 5.4 for elemental silicon  $^{202}$ . Characterization methods, including XRD, FTIR, Raman, SEM, and XPS, confirmed the chemical compositions and structures of the 3D-printed composite ceramics. The addition of silicon nanoparticles in the resin neutralizes excess *in-situ* grown graphitic carbon from polymer pyrolysis through reaction bonding. The resulting material (pyrolyzed *MSR*) is highly crystalline (80.7  $\pm$  0.6 %) SiC-Composite ceramics with large 3C-SiC crystallites (4.47  $\pm$  1.92  $\mu$ m) and minimal excess graphitic carbon, elemental silicon, and SiOC.

3D printed SiC-based composite ceramic parts with high resolution (0.72  $\pm$  0.03 mm) were demonstrated using this method and were macroscopically crack-free with large dimensions (53 mm  $\times$  27 mm  $\times$  21 mm, wall thickness 5 mm), which is a large improvement from literature values of wall thickness 2 mm<sup>177–179</sup>. The improved high-resolution and high-fidelity 3D-printed structures were attributed to the thermal SLA process design with active cooling methods, which rapidly remove the excess heat and prevent it from over-curing the resin. The printed parts with *MSR* composition also demonstrate improved flexural strength (89.6  $\pm$  32.3 MPa) with narrow distributions (Weibull modulus  $m_{\rm M} = 2.716$ ).

In summary, the as-fabricated SiC composite ceramics demonstrate precise printing with intricate structures, and the improved mechanical properties enhance their applicability for applications in industries such as automotive and aerospace.

# CHAPTER 6: *IN-SITU* RAMAN CHARACTERIZATION FOR POLYMER-TO-CERAMIC TRANSITION AND REACTION KINETICS

Parts of this work are adapted from the work of Evelyn Wang and Michael A. Hickner in preparation. This is the version of the article before peer review or editing as submitted by the authors for publication. The publisher is not responsible for any errors or omissions in this version of the manuscript, or any version derived from it.

### 6.1. Abstract

Raman spectroscopy, a powerful and convenient technique for vibrational spectroscopic analysis of materials, has been widely adopted in PDC characterization. However, *in-situ* characterization of the polymer-to-ceramic conversion process has not been emphasized in the literature. This report focuses on *in-situ* characterization of PDCs, which illustrates the real-time reaction and chemical structural changes of PDCs during the polymer-to-ceramic transitions. The reaction kinetics were also measured *in-situ* for PDCs at lower temperatures (up to 1200 °C). While at high temperatures in the final pyrolysis step, the reaction kinetics were measured with the *ex-situ* method, as blackbody radiation completely masked the signals at temperatures higher than 1200 °C. This report clearly illustrates how PCPs change at different temperature ranges up to 1500 °C and reports kinetic data for the chemical structure changes take place during temperature ramps, giving insights into detailed pyrolysis procedures for PDCs and potential structural/compositional evolution throughout the polymer-to-ceramic transition.

### 6.2. Introduction

PDCs have attracted attention since being introduced due to their exceptional processability and excellent properties<sup>23,203,204</sup>. These engineered polymers enable a unique

manufacturing route – initially as highly processable polymers with active side groups for crosslinking, which can be transformed into highly versatile oxide/non-oxide ceramics with exceptional performance upon pyrolysis<sup>73</sup>. The polymeric nature of PCPs enables a bottom-up additive approach for ceramics manufacturing instead of traditional top-down ceramics processing<sup>205</sup>. Furthermore, PCPs also allow engineers unprecedented precise manipulation of ceramics' chemical compositions, crystallinity, physical/chemical properties, and microstructures<sup>23</sup>. However, several steps involving polymeric deposition, ceramic formation, and crystallization are required in a long thermal process to affect the materials transformation<sup>131</sup>. Therefore, in order to fully utilize and unlock the full potential of PDCs, a thorough kinetic and thermodynamic study for understanding their structural changes is indispensable<sup>64,206,207</sup>.

During the pyrolysis procedure, the PCPs undergo multiple compositional and structural transforming stages – from polymerization, shaping, crosslinking, pyrolysis, and high-temperature annealing<sup>208</sup>. The PCPs transform from complex-shaped greenbodies to amorphous ceramics, and subsequently into crystalline ceramics at increasing temperatures. During the first stage below 400 – 500 °C, reactions such as transamination, dehydrogenation, hydrosilylation, and vinyl polymerization take place<sup>208</sup>, which shapes the PCPs, yielding the debinded green body for pyrolysis. Then, at higher temperature ranges (600 – 1000 °C), the initial pyrolysis process of PCPs takes place by thermolysis and organic moiety release, which transform the PCPs into amorphous covalent ceramics. In the final stage of pyrolysis, the amorphous ceramic is transformed into a glassy ceramic by bond rearrangement and crystalline ceramics by sintering<sup>209</sup>. The application of solid-state NMR, TGA, SEM/EDS, FTIR, and Raman has

revealed how these three stages occur from an ex-situ perspective<sup>210,211</sup>. From these characterizations, gas evolution, structural changes, and graphitization can be roughly assigned to specific heating ranges<sup>210</sup>.

While an abundant amount of *ex-situ* characterization of PDCs has been conducted on these three stages, little is known about the detailed structural changes at specific times and temperatures, which is the key to obtaining defect-free ceramics<sup>212,213</sup>. While the literature has gathered a plethora of *ex-situ* measurements of PCPs after pyrolysis at different temperatures and times, there are two major issues with the *ex-situ* methods reported – there is no systematic standard for the heating procedure, and materials are often heated differently under different conditions; *ex-situ* samples have to go through the elongated heating and cooling cycle, which largely affect the composition and structural of the materials<sup>49,214</sup>. Raman spectroscopy, as a powerful characterization tool<sup>215</sup> for measuring the composition and structures of the materials, has only so far been focusing on carbon species<sup>216</sup> and cluster sizes<sup>213</sup> derived from pyrolysis.

In-situ characterization helps<sup>214,217</sup> to unravel the real-time polymer-to-ceramic transitions with molecular-level insights, especially since the decomposition, polymer-to-ceramic transitions<sup>218</sup> and carbothermal reduction<sup>213</sup> are strong functions of the heating rate and time<sup>219</sup>. Monitoring the vibrational mode evolution changes throughout the heating process makes it possible to track the chemical changes of material during the heating process. Laser-based spectroscopy, like Raman<sup>214</sup>, can pinpoint and identify the formation and disappearance of new phases and structures in the samples, giving insights into the transitional temperature and phase stability<sup>220</sup>. Also, the shift and alterations in the peaks can also reveal the real-time compositional changes in the sample<sup>211</sup>. Additionally, reaction kinetics can also be extracted from a series of

time-dependent Raman spectroscopy measurements<sup>221</sup>, which gives valuable insights into how to conduct pyrolysis of PCPs and how fast to conduct the pyrolysis for optimal polymer-to-ceramics transition. It has been reported that, from TGA measurements, the decomposition of polyborazine can be fitted with different kinetic models like first-order kinetics<sup>64</sup>, which helps predict experimental data for pyrolysis.

In the current study, we designed an *in-situ* Raman characterization setup to analyze the real-time polymer-to-ceramic structural/compositional changes. The spectra during measurements are calibrated with an external reference light source, and the peaks at high temperatures are subtracted from blackbody radiation with an algorithm developed in this report. Additionally, the reaction kinetics of PDCs were captured *in situ* for reactions under 1200 °C, where the entire decomposition curve and structural changes were captured and characterized. Above 1200 °C, due to the significant amount of blackbody radiation, the reaction kinetics were only measured for *ex-situ* experimental data. The kinetics of ceramics transformation was subsequently fitted with first-order kinetics to show the impacts of temperature, time, and active fillers on the polymer to ceramic conversion process.

### 6.3. *In-situ* Raman characterization

### 6.3.1. Materials

Chapter 5 discussed the starting materials and resin compositions (session 5.3.1). This report chooses two resins, 877 and *MSR*, for conducting *in-situ* and *ex-situ* experiments. The resins are cured in a silicone mold in a tube furnace under UHP argon flow. The furnace is heated from room temperature to 200 °C with a ramp rate of 5 °C/min, held for 0.5 h, and then cooled down to room temperature with the same ramp rate.

# 6.3.2. Characterization and experimental setup

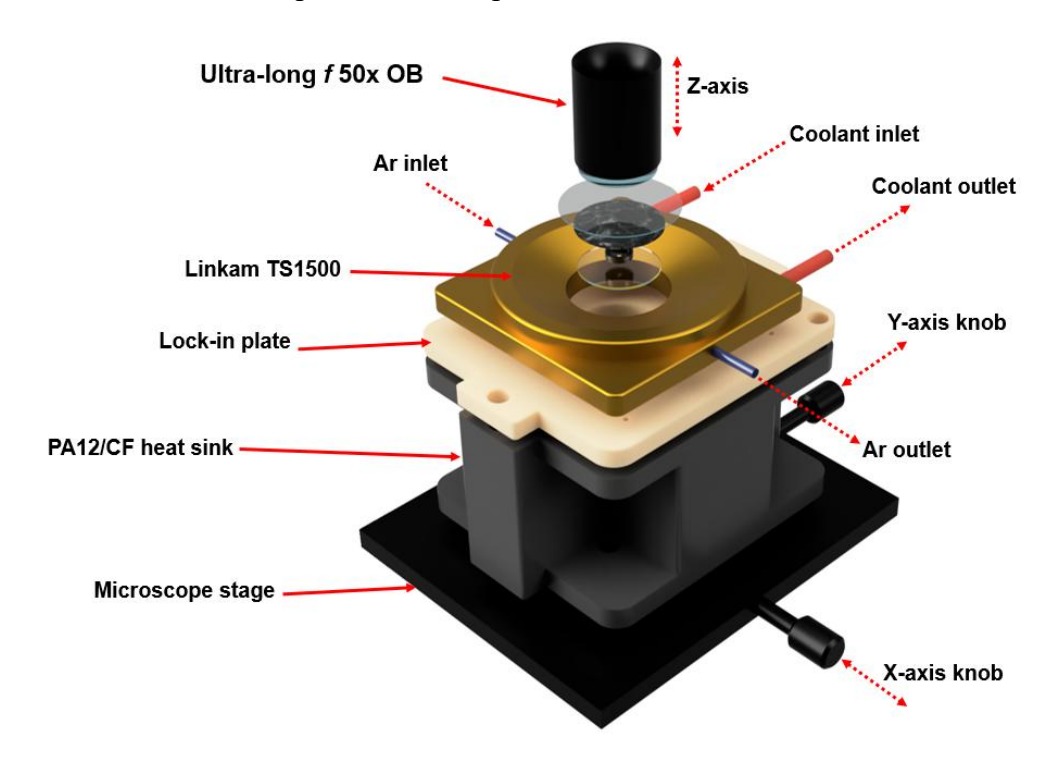


Figure 6.1. *In-situ* Raman characterization setup.

In-situ Raman spectroscopy was conducted using a Horiba SMS core iHR320 FS-FS ML Raman system. This highly customizable system was integrated with a Linkam TS1500 high-temperature reaction cell for precise temperature control (Figure 6.1). To facilitate heat dissipation during high-temperature experiments (up to 1500 °C), the reaction cell was mounted on a PA12/CF heat sink. The hollow design of the heat sink (shown in Figures 6.2 and 6.3) effectively contains extreme temperatures within the spectroscopic region. The TS1500 cell was fixed onto the heat sink with a lock-in plate, which locks the cell into place and dampens the sample vibration during measurements.

The microscope stage provided precise x-y positioning of the entire system with a resolution of 10 µm, while the z-axis was controlled by adjusting the position of the Raman

objective. Before each measurement, fine adjustments were made to the x, y, and z positions to ensure optimal alignment of the Raman laser, objective, and pinholes within the TS1500 cell. During the sample pyrolysis process, the laser was focused on the sample surface to acquire the *in-situ* Raman spectra.

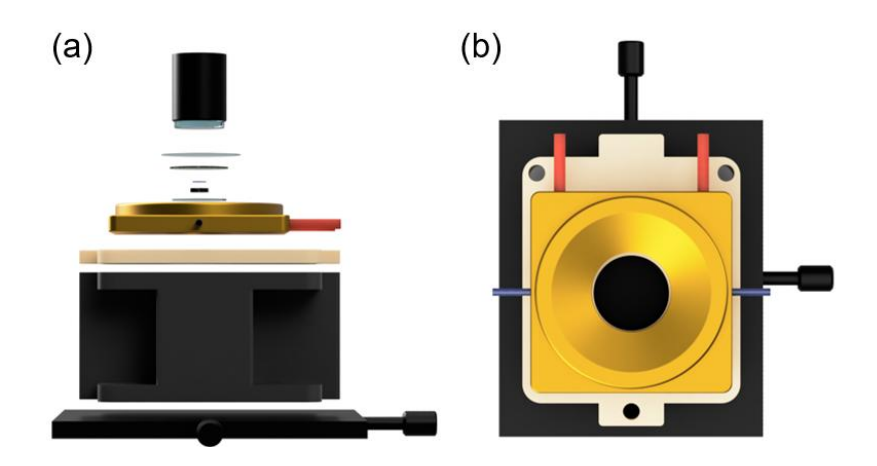


Figure 6.2. CAD design of *in-situ* Raman system for polymer-to-ceramic transition (a) front view; (b) top view.

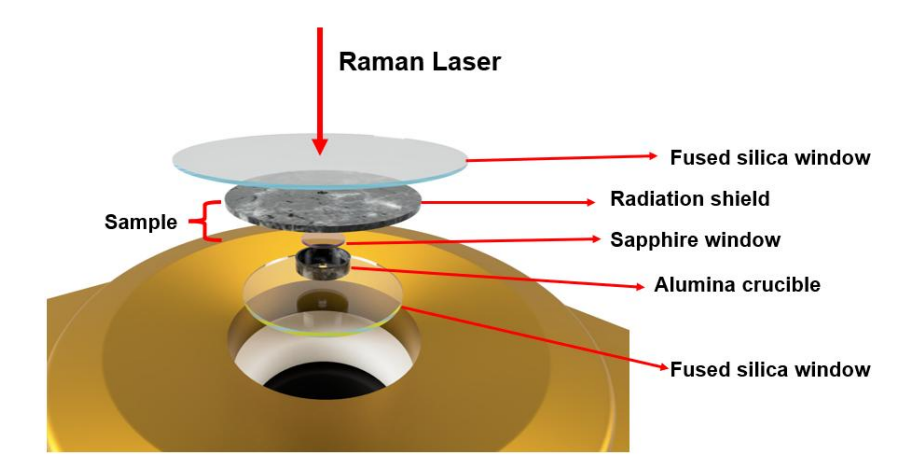


Figure 6.3. Linkam TS1500 cell CAD design for *in-situ* characterization.

The TS1500 cell consists of multiple layers (Figure 6.3). Top and bottom fused silica windows contain the reaction within an inert environment. An alumina radiation shield prevents excessive heat loss and blocks thermal radiation from reaching the Raman detector, while a

central pinhole allows the laser and Raman signal to pass through. The sample, placed in an alumina crucible, rests on a sapphire window within the cell. To maximize signal intensity, the laser was precisely focused on the sample surface through the windows and the pinhole in the radiation shield.

Before each experiment, the TS1500 cell was purged with ultra-high purity (UHP) argon for 20 minutes at a 30 cm<sup>3</sup>/min flow rate, then kept at 15 cm<sup>3</sup>/min throughout the heating process. During the reaction, coolant water circulation maintained a stable temperature within the crucible, preventing damage to the reaction cell.

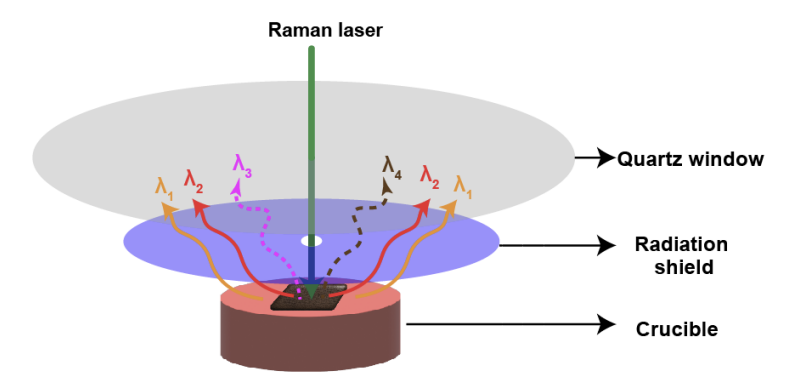


Figure 6.4. Laser enters the Linkam TS1500 cell, and light is emitted from the sample.

During Raman measurements, the laser is focused on the sample, emitting multiple signals. As depicted in Figure 6.4,  $\lambda_3$  represents the Raman signal of interest, including Stokes, anti-Stokes scattering, and Rayleigh scattering. Apart from this,  $\lambda_4$  denotes fluorescence,  $\lambda_2$  represents blackbody radiation from the sample, and  $\lambda_1$  illustrates blackbody radiation from the crucible. The radiation shield effectively blocks  $\lambda_1$  and attenuates  $\lambda_2$ .

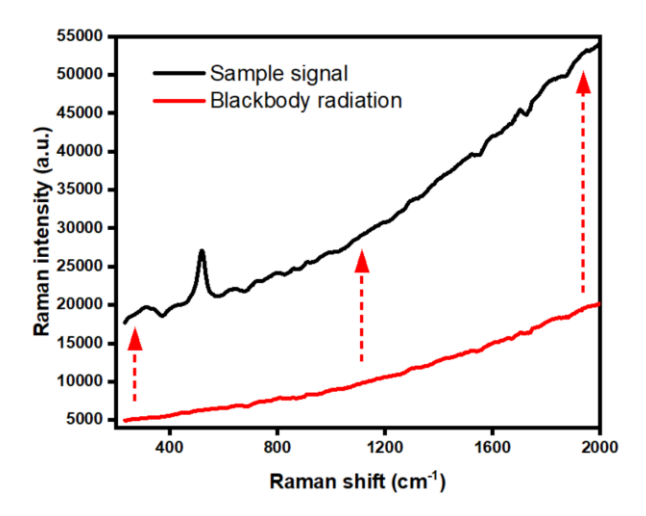


Figure 6.5. Normalizing peak and subtracting blackbody radiation. The sample is silicon-based (MSR) heating in-situ at 1100 °C for 0 min.

Since there are no peaks at the minimum and maximum values, the blackbody radiation was normalized to the sample signal, so the minimum and maximum are the same as the sample signal. After normalization, the sample signal was deducted from the blackbody radiation to show the actual peaks hidden in the blackbody radiation at elevated temperatures (Figure 6.5)<sup>222</sup>.

$$B_{v}(v,T) = \frac{2hv^{3}}{c^{2}} \times \frac{1}{\exp(\frac{hv}{kT})-1}$$
 (6.1)

Blackbody radiation is shown in eq. 6.1, where  $B_v(v,T)$  is spectral radiance, h stands for Planck constant, v means the frequency of electromagnetic radiation, c denotes the speed of light in a vacuum, k represents the Boltzmann constant, and T is defined as the body's absolute temperature.

Blackbody radiation from the sample ( $\lambda_2$ ) was measured separately and subtracted from the signal spectrum using an algorithm (Figure 6.5). *In-situ* measurements after 1000 °C demonstrate a significant amount of blackbody radiation, which was normalized with the aforementioned method to maximize the signal-to-noise ratio. To minimize fluorescence ( $\lambda_4$ ), a

longer wavelength laser (785 nm) was employed. Furthermore, fluorescence quenching techniques were implemented, where the chromophores were photo-bleached with a 785 nm laser for 5 mins before measurement.

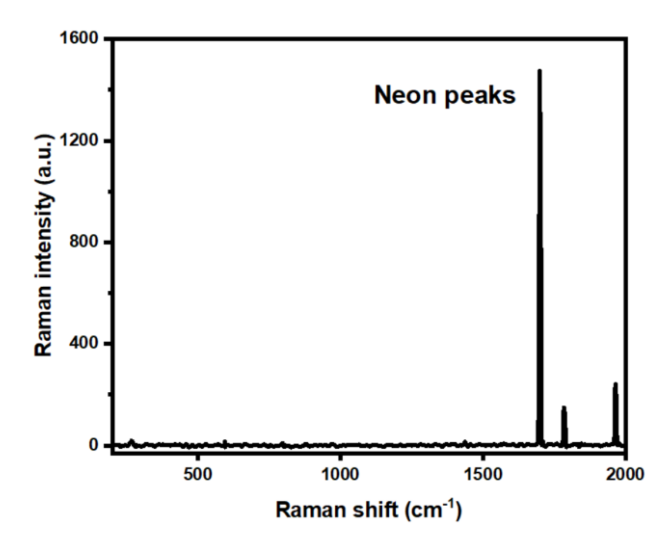


Figure 6.6. Peak calibration during measurement with neon light (for 532 nm Raman laser).

During extended measurement, the spectral shift will become more severe during the Raman measurement<sup>214</sup>, which causes peak shifting during measurements. Also, during measurement, blackbody radiation from high-temperature regions and fluorescence from low-temperature regions will cause significant noise. This noise will also induce spectral shifts as peaks are buried in the noises. In order to counter the spectral shifts, a 585 nm neon gas LED was placed in the detector pathway to compensate for the peak shift<sup>214</sup>. The neon LED will have three characteristic peaks from 200 cm<sup>-1</sup> to 2000 cm<sup>-1</sup> – 1698.5, 1784.0 and 1963.8 cm<sup>-1</sup>. Since the wavelength of neon light will never change, these three sharp peaks will also not alter their positions in the Raman spectra. All measured spectra are calibrated with neon light peaks, as shown in Figure 6.6.

### 6.3.3. Results and Discussion

All the Raman spectra peaks are referred to as listed in the literature<sup>223</sup>.

The *ex-situ* samples were heated to the desired temperature with a rate of 5 °C/min, held for 1 hour, and then cooled to room temperature at 5 °C/min. In contrast, the *in-situ* samples were heated at a rate of 100 °C/min. All samples were heated under ultra-high purity (UHP) argon flow (50 cm<sup>3</sup>/min for *ex-situ* and 15 cm<sup>3</sup>/min for *in-situ*).

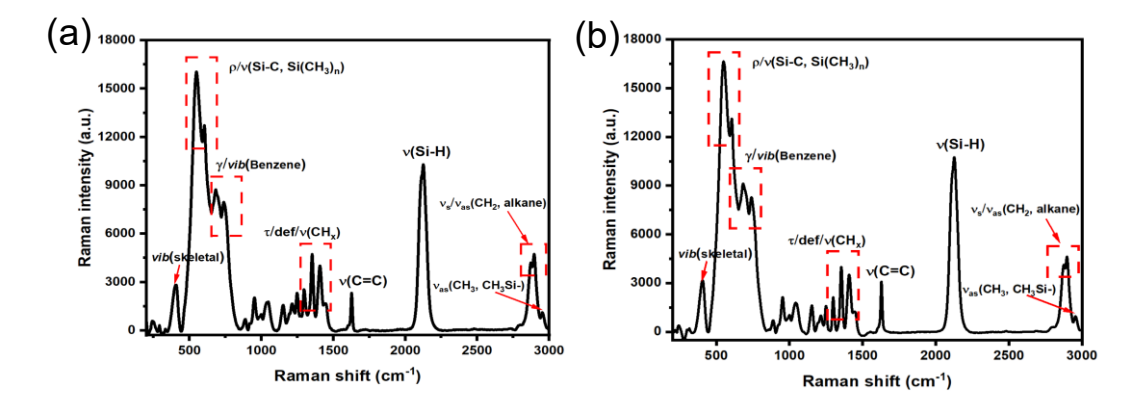


Figure 6.7 Room temperature spectra of cured SMP877 (a) *in-situ*; (b) *ex-situ*.

No differences were observed between *in-situ* and *ex-situ* samples at room temperature apart from a slightly weaker Raman signal in the former spectrum (Figure 6.7). This indicates that the *in-situ* cell does not introduce additional peaks or significantly attenuate the signal. Additionally, we notice the sharp stretching peak of v(Si-H) at 2125 cm<sup>-1</sup>, originating from the Si-H side chain from SMP-877. The v(C=C) peak at around 1627 cm<sup>-1</sup> shows the uncrosslinked double bond in the polymer, which originated from the allyl group on the SMP-877 resin. The rocking and stretching peak of  $\rho/v(Si-C, Si(CH_3)_n)$  at around 548 – 605 cm<sup>-1</sup> denotes the backbone of the polycarbosilane structure. The stretching peak  $v_s/v_{as}(CH_2, alkane)$  at 2872 – 2896 cm<sup>-1</sup> and asymmetric stretching peak  $v_{as}(CH_3, CH_3Si-)$  at around 2953 cm<sup>-1</sup> stands for alkane groups attached and not attached to silicon backbone. Finally, the peaks around 681 – 738

cm<sup>-1</sup> are bending band  $\gamma$ (Benzene) and vibrational band vib(Benzene), which originates from the thermal initiator dicumyl peroxide.

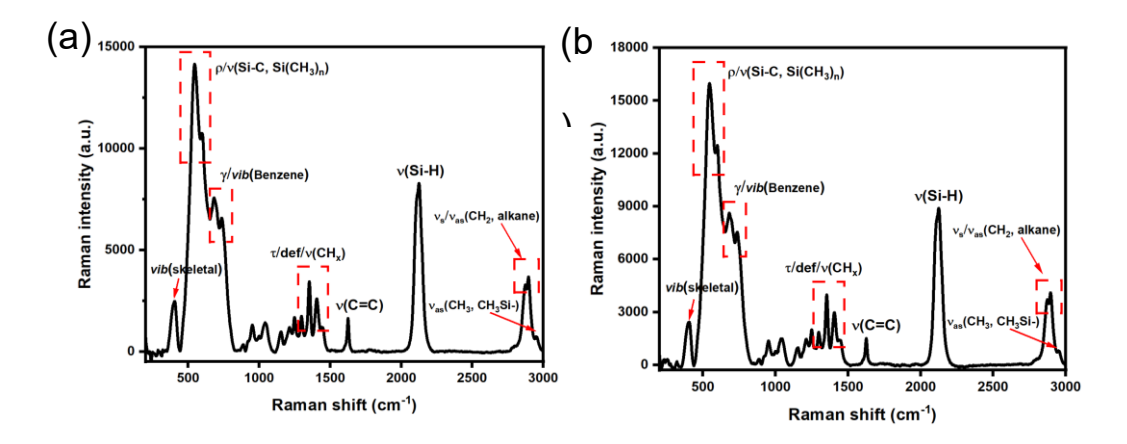


Figure 6.8. Spectra taken at 200 °C in-situ for SMP877 heating for (a) 0 min; (b) 30 min.

At 200 °C, there are minimal differences in peak position and strength from room-temperature measurements (Figure 6.8). However, after heating the sample *in situ* at 200 °C for 30 min, a decrease in the  $\nu$ (C=C) peak intensity at approximately 1627 cm<sup>-1</sup> was observed. This attenuation indicates that the polycarbosilane SMP-877 begins to crosslink at this temperature, consistent with the observation that the samples harden at 200 °C under the employed curing conditions.

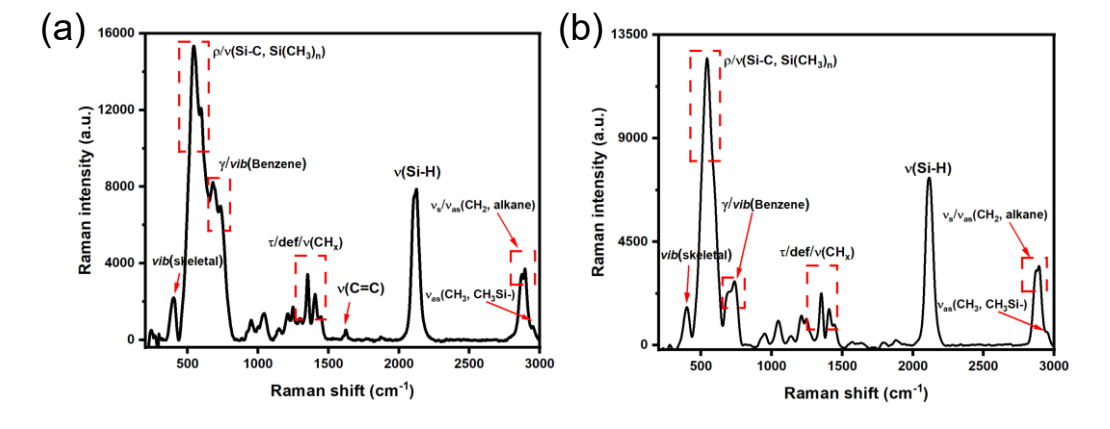


Figure 6.9. Spectra taken at 300 °C in-situ for SMP877 heating for (a) 0 min; (b) 30 min.

At 300 °C, rapid crosslinking happens during this heating stage (Figure 6.9). Even at 0 min, the v(C=C) peak at around 1627 cm<sup>-1</sup> significantly shrank, while at 30 min, this peak completely disappeared. This observation signifies the crosslinking process completes heating at 300 °C for 30 min.

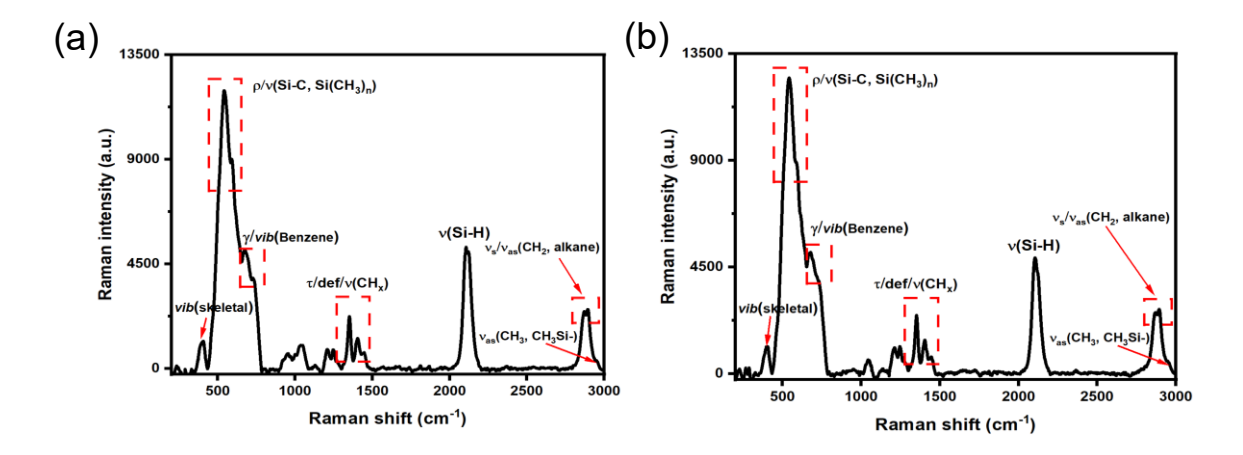


Figure 6.10. Spectra taken at 400 °C in-situ for SMP877 heating for (a) 0 min; (b) 30 min.

At 400 °C, the  $\nu(Si-H)$  peak at approximately 2125 cm<sup>-1</sup> decreased in intensity compared to the spectra at 300 °C, indicating the onset of dehydrogenation. Furthermore, an additional decrease in the Si-H peak intensity was observed upon heating from 0 to 30 min, suggesting further dehydrogenation (Figure 6.10).

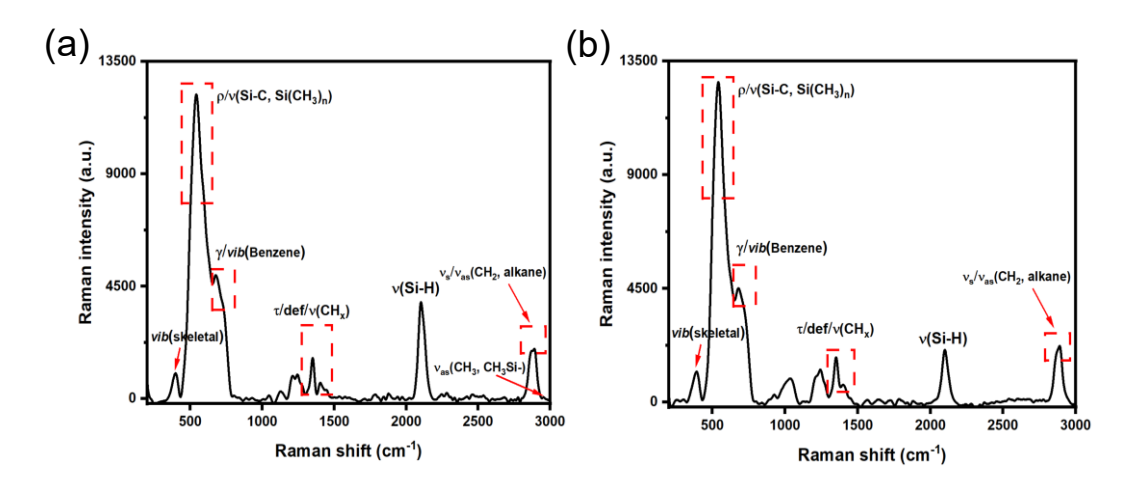


Figure 6.11. Spectra taken at 500 °C in-situ for SMP877 heating for (a) 0 min; (b) 30 min.

At 500 °C, significant dehydrogenation occurs, as evidenced by the sharp drop in intensity of the v(Si-H) peak at approximately 2125 cm<sup>-1</sup>. This dehydrogenation is particularly pronounced after 30 min of heating, where a substantial reduction in the v(Si-H) peak is observed (Figure 6.11). Moreover, the decrease in intensity of the twisting/deformation/stretching  $\tau/def/v(CH_x)$  peak at 1353 - 1447 cm<sup>-1</sup> indicates the initial breakdown of alkane side chains. The disappearance of the  $\nu_{as}(CH_3, CH_3Si-)$  peak at approximately 2953 cm<sup>-1</sup> after 30 min suggests the initial cleavage of silicon-based side chains.

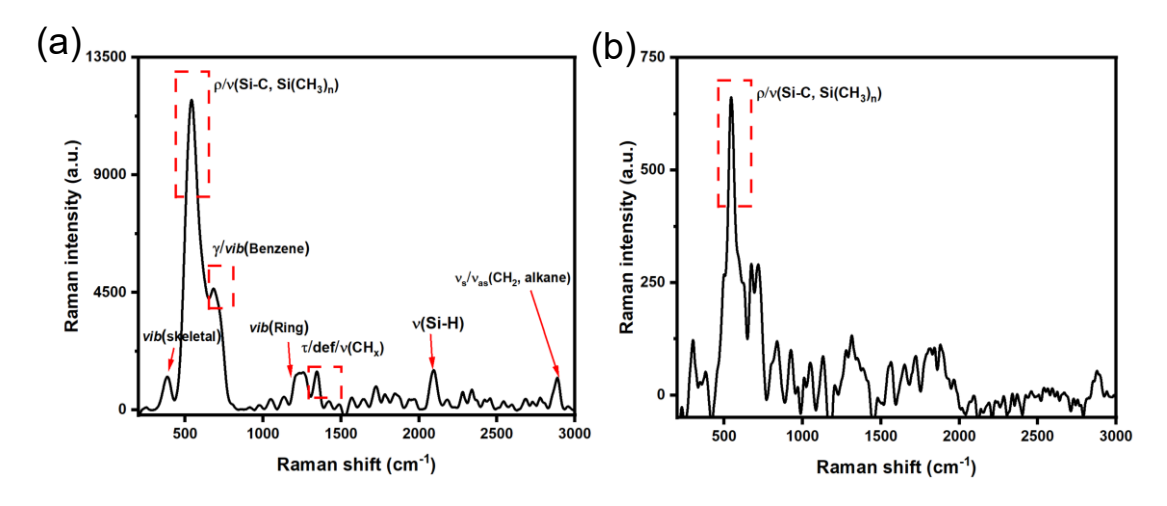


Figure 6.12. Spectra taken at 600 °C in-situ for SMP877 heating for (a) 0 min; (b) 30 min.

At 600 °C (Figure 6.12), significant dehydrogenation occurs immediately upon heating (0 min). Additionally, a significant decrease in the intensity of the  $\tau/\text{def/v}(\text{CH}_x)$  peak at 1353-1447 cm<sup>-1</sup> indicates the breakdown of alkane side chains. Notably, significant fluorescence is observed after heating for 30 min, and only the backbone  $\rho/\nu(\text{Si-C}, \text{Si}(\text{CH}_3)_n)$  peak survived at approximately 548-605 cm<sup>-1</sup>. This suggests the formation of aromatic species and the onset of polymer backbone rearrangement.

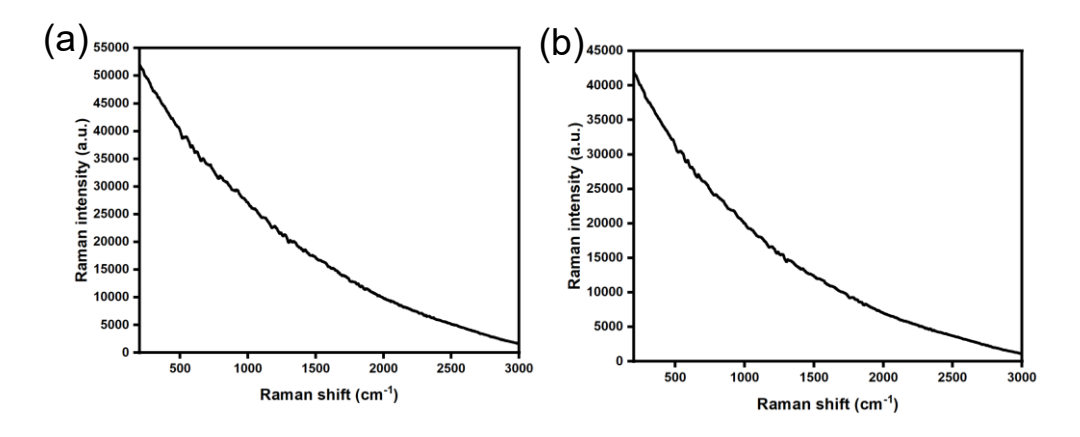


Figure 6.13. Spectra taken at 700 °C in-situ for SMP877 heating for (a) 0 min; (b) 30 min.

Significant fluorescence occurs when the temperature rises to 700 °C, completely masking the peaks and rendering these spectra unprocessable and no interpretation was possible. The fluorescence is likely due to organic ring compounds.

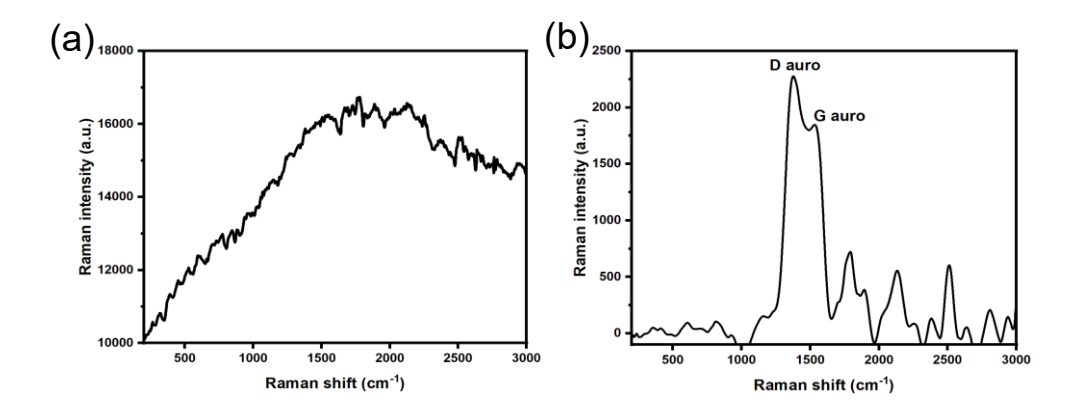


Figure 6.14. Spectra taken at 800 °C in-situ for SMP877 heating for (a) 0 min; (b) 30 min.

Upon initial heating to 800 °C, a significant decrease in fluorescence was observed (Figure 6.14). This reduction is likely due to the elevated temperature accelerating the decomposition of organic compounds. The spectral profile also changed at this stage, suggesting alterations in the fluorophore compositions. After 30 min of heating at 800 °C, the fluorescence further diminished, revealing a broad peak at approximately  $1200 - 1600 \, \text{cm}^{-1}$ . This peak, characteristic of the G band in Raman spectra, indicates the onset of graphitization<sup>224</sup>.

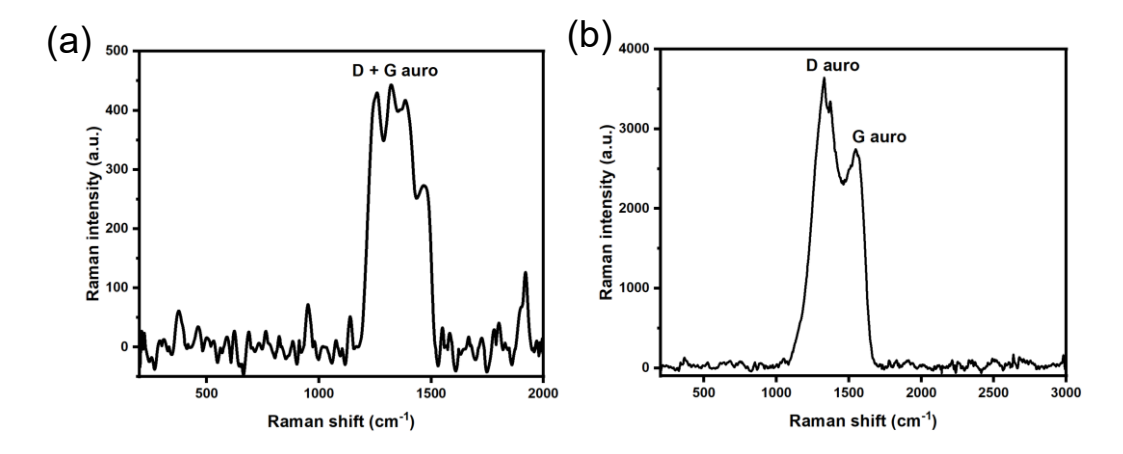


Figure 6.15. Spectra taken for SMP877 (a) *in-situ* heating at 1000 °C for 0 min; (b) *ex-situ* room temperature measurement heated at 1000 °C.

At 1000 °C, fluorescence attenuates as more organic species decompose, and blackbody radiation becomes the dominant noise source at this heating stage (Figure 6.15). Figure 15(a) concludes that D and G auro start to differentiate more from background noise. The *ex-situ* data (Figure 15(b)) backs up the *in-situ* (Figure 15(a)) data. D and G band auro at 1329 cm<sup>-1</sup> and 1543 cm<sup>-1</sup> denote graphitization.

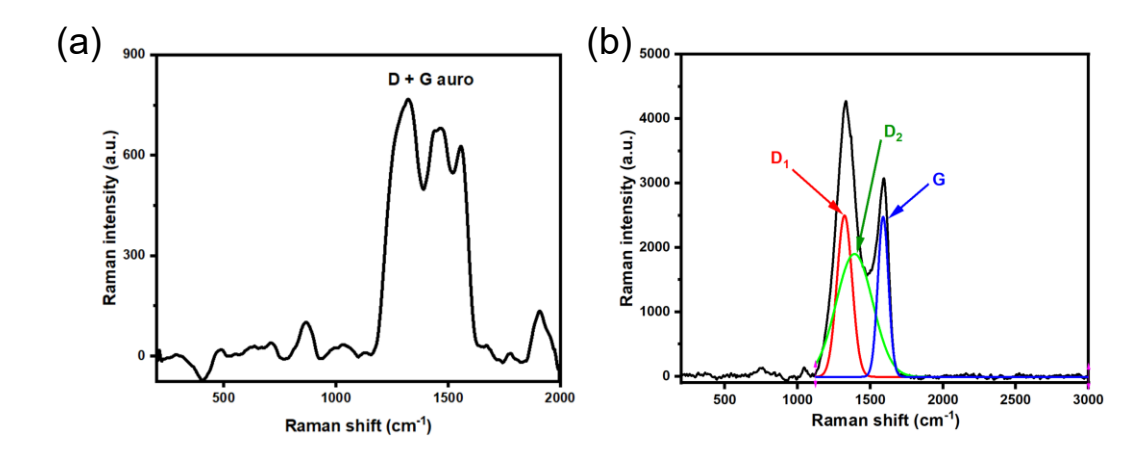


Figure 6.16. Spectra taken for SMP877 (a) *in-situ* heating at 1200 °C for 0 min; (b) *ex-situ* room temperature measurement for SMP877 heated at 1200 °C.

At 1200 °C, blackbody radiation intensifies, increasing noise and hindering data processing (Figure 6.16). However, the increased temperature leads to further suppression of fluorescence due to the decomposition of organic compounds, allowing for clearer observation of the D and G bands. The *ex-situ* data (Figure 16(b)) support the findings from the *in-situ* data (Figure 16(a)), showing distinct D and G bands. Peak deconvolution using Gaussian fitting reveals the D<sub>1</sub> (1321 cm<sup>-1</sup>), D<sub>2</sub> (1392 cm<sup>-1</sup>), and G (1588 cm<sup>-1</sup>) bands, indicative of more complete graphitization<sup>225</sup>.

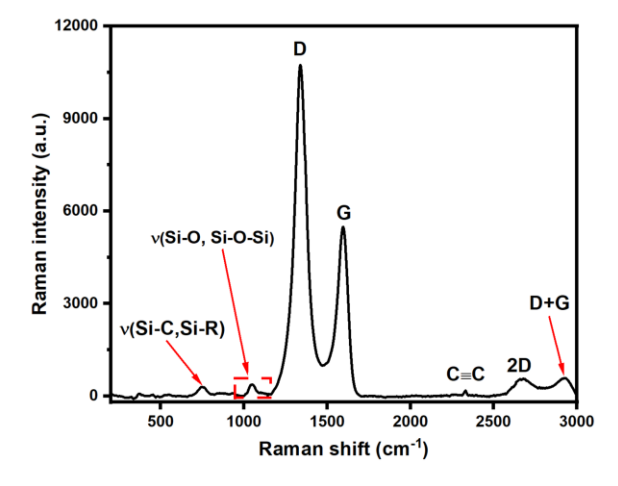


Figure 6.17. The *ex-situ* spectrum taken at room temperature for SMP877 and heated at 1400 °C.

At 1400 °C, blackbody radiation overwhelms the Raman signal, making *in-situ* peak extraction impossible. Therefore, *ex-situ* experiments (Figure 16.17) provide valuable insights into the transformations occurring at this temperature. The D and G bands are fully resolved, and the large D/G ratio indicates a highly disordered graphitic structure.

A weak v(Si-C, Si-R) peak is observed around 750 cm<sup>-1</sup>, and a weak v(Si-O, Si-O-Si) stretching peak at approximately 1046 cm<sup>-1</sup> represents residual silica species<sup>104</sup>, suggesting the presence of excess oxygen. The weak  $C \equiv C$  peak indicates negligible alkyne species at approximately 2250 cm<sup>-1</sup>. The broad 2D overtone band at 2675 cm<sup>-1</sup> suggests the presence of few-layer graphene, while the D + G combination band at 2922 cm<sup>-1</sup> confirms the presence of defects in the graphene structure.

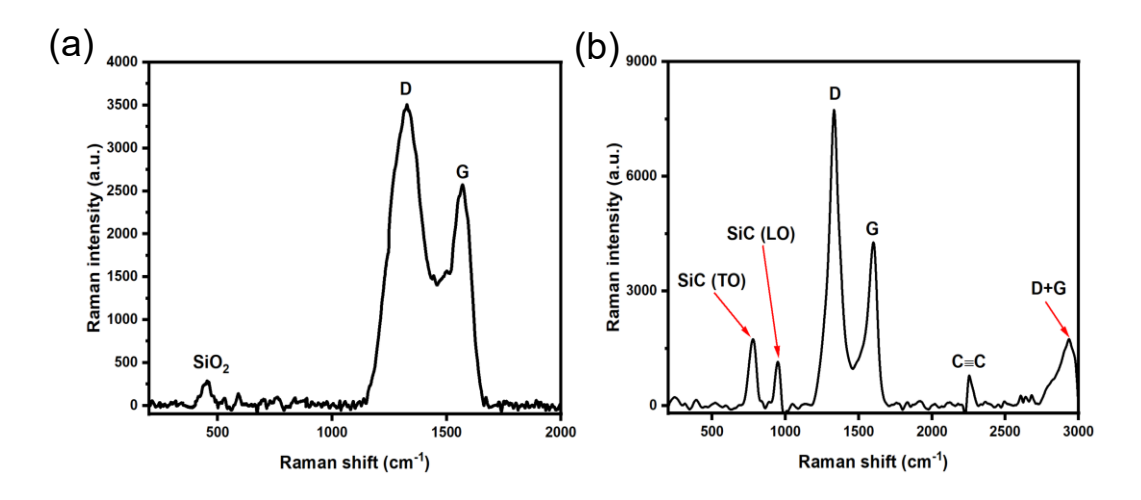


Figure 6.18. Spectra taken at room temperature for SMP877 (a) heated in the *in-situ* cell for 30 min at 1500 °C; (b) *ex-situ* room temperature measurement for SMP877 heated at 1500 °C.

Due to the intense blackbody radiation at 1500 °C, which hinders *in-situ* Raman analysis, the sample was cooled to room temperature within the *in-situ* cell for spectral acquisition (Figure 18(a)). The D and G bands are fully resolved, and a weak SiO<sub>2</sub> band is observed around 460 cm<sup>-</sup>

<sup>1</sup>. *Ex-situ* measurements provide further insights into the structural evolution at 1500 °C. The D and G bands are fully resolved, and the large D/G ratio indicates a highly disordered graphitic structure. The SiC (TO) band at approximately 780 cm<sup>-1</sup>, and the SiC (LO) band<sup>226,227</sup> at approximately 945 cm<sup>-1</sup> show increased intensity. Compared to 1400 °C, the increase in carbide species at the expense of silica species at 1500 °C suggests that carbothermal reduction occurs at this temperature. Both the alkyne peak at approximately 2250 cm<sup>-1</sup> and the D + G combination<sup>228</sup> band at approximately 2930 cm<sup>-1</sup> also exhibits growth.

### 6.4. Ex-situ kinetics study

Besides *in-situ* characterizations, *ex-situ* experiments give us more insights into when and how fast the carbothermal reduction of silica/carbon and reaction bonding of silicon/carbon happens. The Raman peaks are extracted and fitted with Gaussian equations; their intensities are taken to estimate different species' relative content and reaction kinetics.

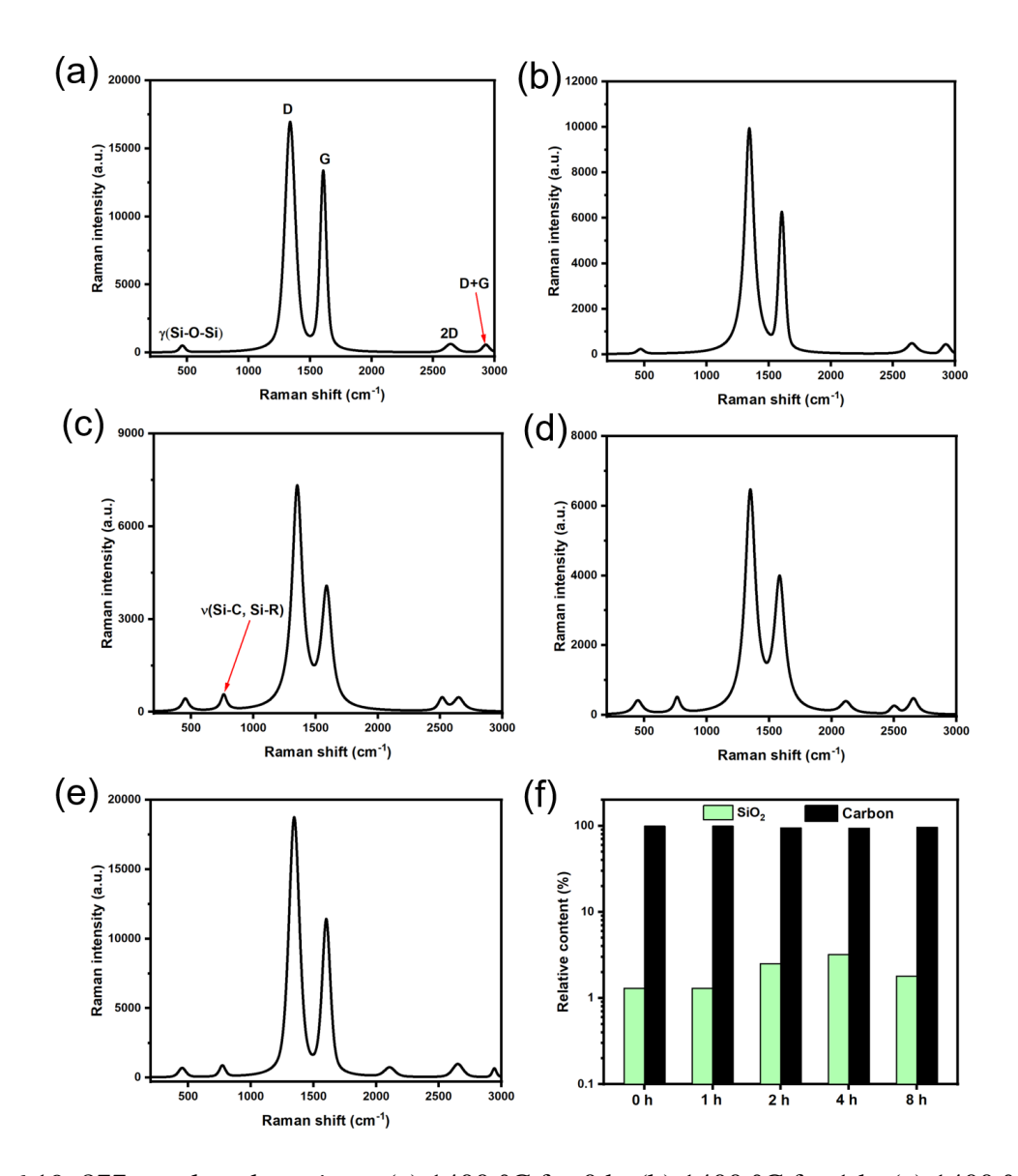


Figure 6.19. 877 pyrolyzed *ex-situ* at (a) 1400 °C for 0 h; (b) 1400 °C for 1 h; (c) 1400 °C for 2 h; (d) 1400 °C for 4 h; (e) 1400 °C for 8 h; (f) relative content of different species variation with time.

It can be concluded from Figure 6.19 that for pure PCPs like polycarbosilanes SMP877, pyrolysis under 1400 °C only yields graphitic carbon and SiO<sub>2</sub>, with no effect of reaction duration. Longer pyrolysis times at 1400 °C does not significantly alter the composition of the samples. After heating at 1400 °C for 1 h, it is noted that a very small Si-R stretching v(Si-C, Si-

R) at around 750 cm<sup>-1</sup>, which is derived from either a high concentration of stacking faults or the confinement of phonons within sub-nanometer regions<sup>229</sup> of crystalline beta-silicon carbide<sup>229</sup>. These results indicate that a very small amount of carbothermal reduction occurred at 1400 °C with a very slow speed, yielding negligible nanocrystalline amorphous Si-C structures.

While pure polycarbosilane 877 heating at 1400  $^{\circ}$ C shows no signs of compositional shift or carbothermal reduction (Figure 6.20), the peaks start to differentiate and show signs of carbothermal reduction at 1500  $^{\circ}$ C.

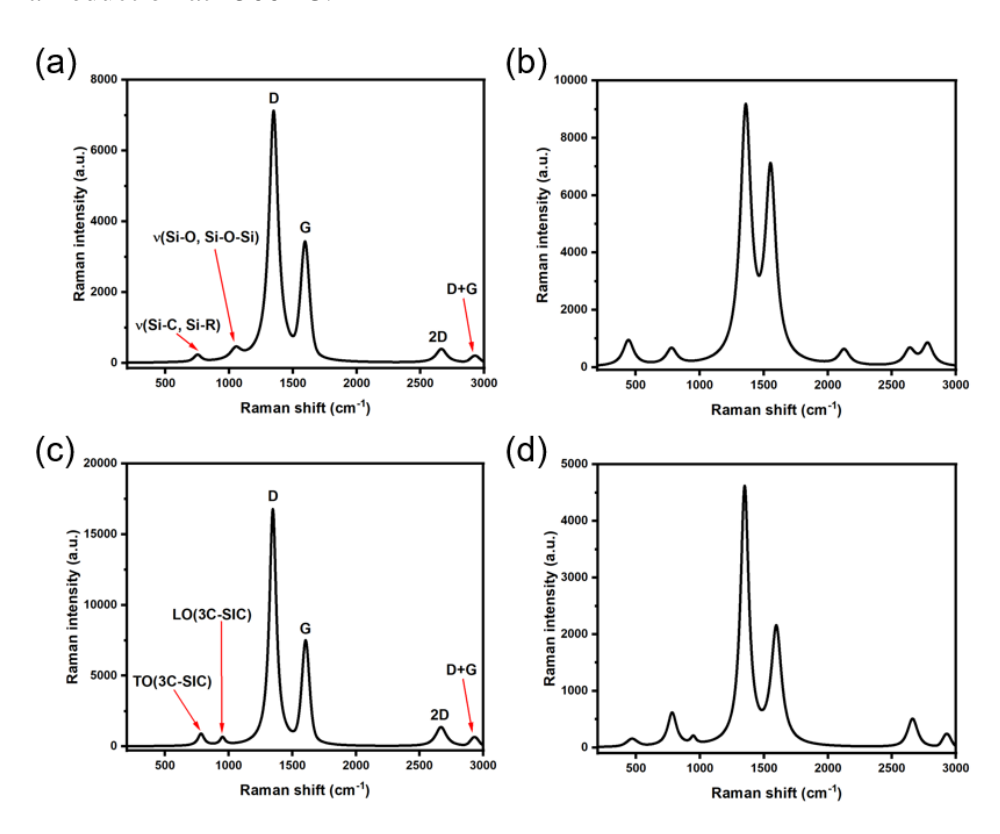


Figure 6.20. 877 pyrolyzed *ex-situ* at (a) 1500 °C for 0 h; (b) 1500 °C for 0.5 h; (c) 1500 °C for 1 h; (d) 1500 °C for 2 h.

When heated at elevated temperatures, SiC slowly grows at the cost of carbon and silica through carbothermal reduction, which is detailed in Figure 6.21(a). Furthermore, Figure 6.21(b) summarizes how different species evolve and the first-order kinetics of carbothermal reduction.

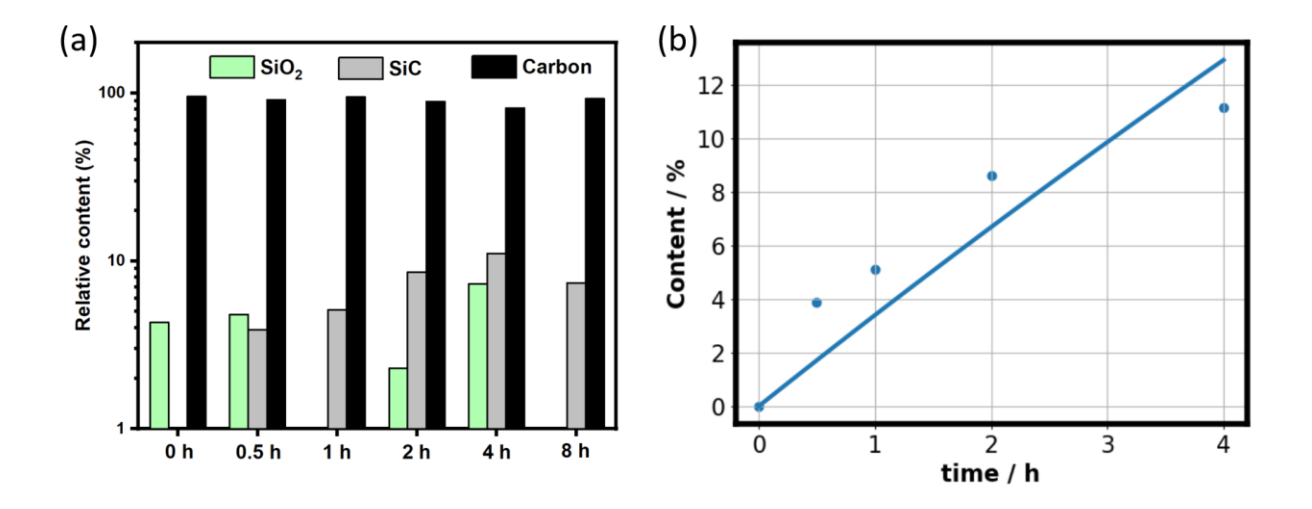


Figure 6.21. (a) evolution of relative content of different species with time; (b) first-order kinetics fitting of SiC. The 877 samples are pyrolyzed at 1500 °C.

Different species generated throughout the pyrolysis process are recorded with Raman spectroscopy (Figure 6.21), where the relative content of the SiC species grows with longer pyrolysis time as the carbothermal reaction takes place at 1500 °C, and the relative content is fitted with first-order kinetics (eq. 6.2):

$$In[A] = -kt + In[A]_0 \tag{6.2}$$

$$C = \frac{A}{A_0} = (1 - e^{-0.0346t}) \times 100\%$$
 (6.3)

where [A] stands for the concentration of the species of interest, k is the rate constant, t means time, [A]<sub>0</sub> represents the initial concentration of the species of interest, and C denotes relative concentration.

Figure 6.21 (b) plots the relative concentration C of SiC changing with time, and the kinetics equation is derived in eq. 6.3. It can be concluded that the speed of SiC generation is very slow and trending toward even slower. The reaction has a kinetics rate of 0.0346 (k<sub>1</sub>).

Figure 6.22 illustrates 877 and MSR compositional, morphological evolution throughout the heating process.

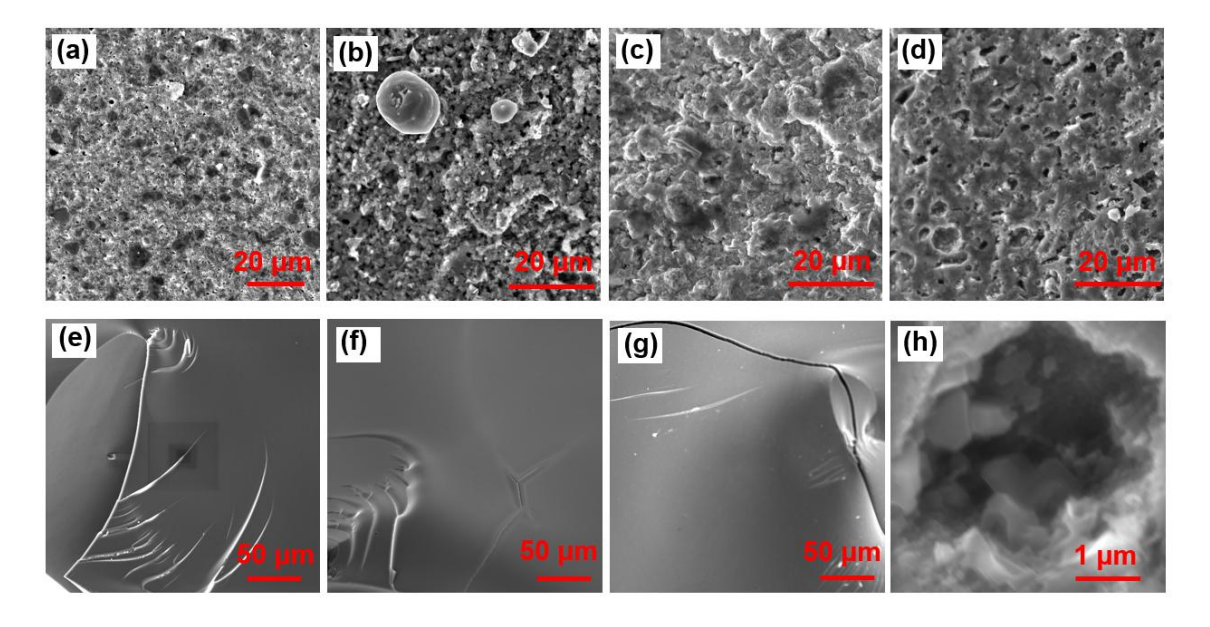


Figure 6.22. SEM micrographs of *MSR* heated at 1400 °C for (a) 0 h; (b) 1 h; (c) 4 h; (d,h) 8 h. 877 heated at 1400 °C for (e) 0 h; (f) 8 h. 877 heated at 1500 °C for (g) 2 h.

The SEM micrographs in Figure 6.22 (e,f,g) show that despite the heating time (0 – 8 h) and heating temperature (1400 - 1500 °C), pure polycarbosilanes SMP-877 does not yield any crystalline structures. Instead, there are only amorphous phases with cracks presented in the samples, resulting from shrinkage associated with turning polymers into ceramics. Elemental silicon has a melting temperature of 1414 °C, which denotes that the silicon nanoparticles will not melt at this temperature, and reaction bonding will only happen at the silicon-carbon boundary. This is illustrated in Figure 6.24(a) Raman spectra, where a small amount of SiC is generated while a large amount of graphitic carbon still resides in the *MSR* sample. This is also made clear in Figure 6.22 (a-c), where the clear boundaries of two phases are presented in the sample, and there are no crystalline structures. Up to 4 h of heating at 1400 °C, no visual growth

of SiC was noted in the sample. Only after 8 h, sub-micron sizes SiC were observed in the samples (Figure 6.22 (d,h)), which is also evidenced by the sudden growth of SiC in the Raman peak (Figure 6.24(a))

Ex-situ experiments were also conducted on silicon-based resin MSR to study when and how fast reaction bonding between silicon and carbon occurs in the samples during firing; the results are shown in Figure 6.23 to 6.26. Due to the limited amount of silicon species in pure polycarbosilane, the reaction speed of carbothermal reduction is extremely slow ( $k_1 = 0.0346$ ). This is the main reason for PDC impurity – low ceramic yield SiC and excess carbon. While amorphous SiOC in the sample binds the sample together, the graphitic carbon still acts as a secondary phase that separates the continuous phase and weakens the samples. In order to solve this issue, silicon was added to the resin composition as an active filler (as discussed in Chapter 5).

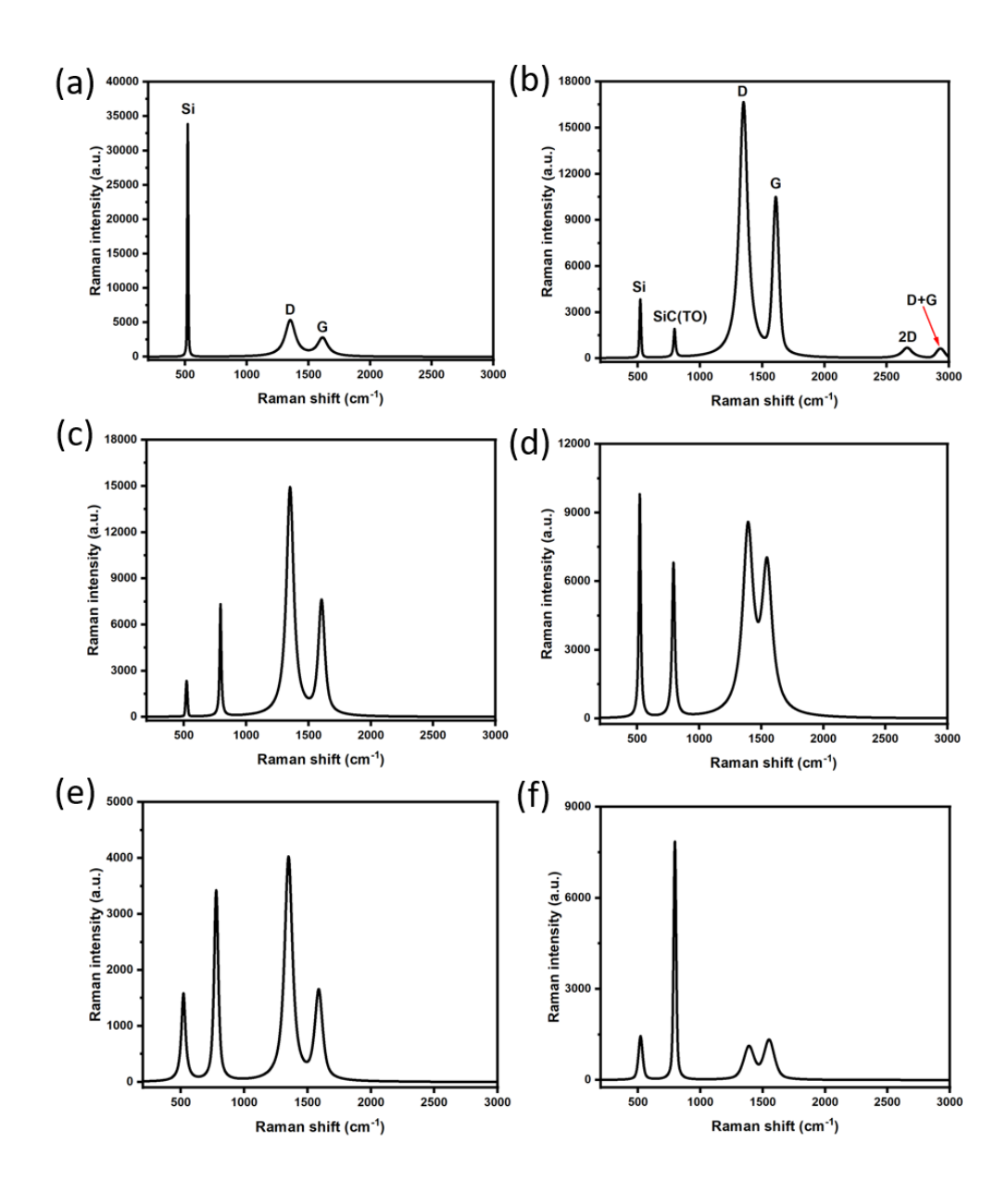


Figure 6.23. *MSR* pyrolyzed *ex-situ* at (a) 1400 °C for 0 h; (b) 1400 °C for 0.5 h; (c) 1400 °C for 1 h; (d) 1400 °C for 2 h; (e) 1400 °C for 4 h; (f) 1400 °C for 8 h.

From Figure 6.23, it can be concluded that the addition of silicon in polycarbosilane significantly speeds up the reaction kinetics of SiC, where reaction bonding helps neutralize the excess carbon in the sample. At 1400 °C, silicon does not yet melt, which also confines the reaction bonding to adjacent areas where silicon impinges graphitic carbon (as shown in SEM

micrographs). With a longer heating time at 1400 °C (Figure 6.23(a-f)), it is clear that SiC species grow at the cost of both silicon and carbon, which denotes the reaction bonding of SiC.

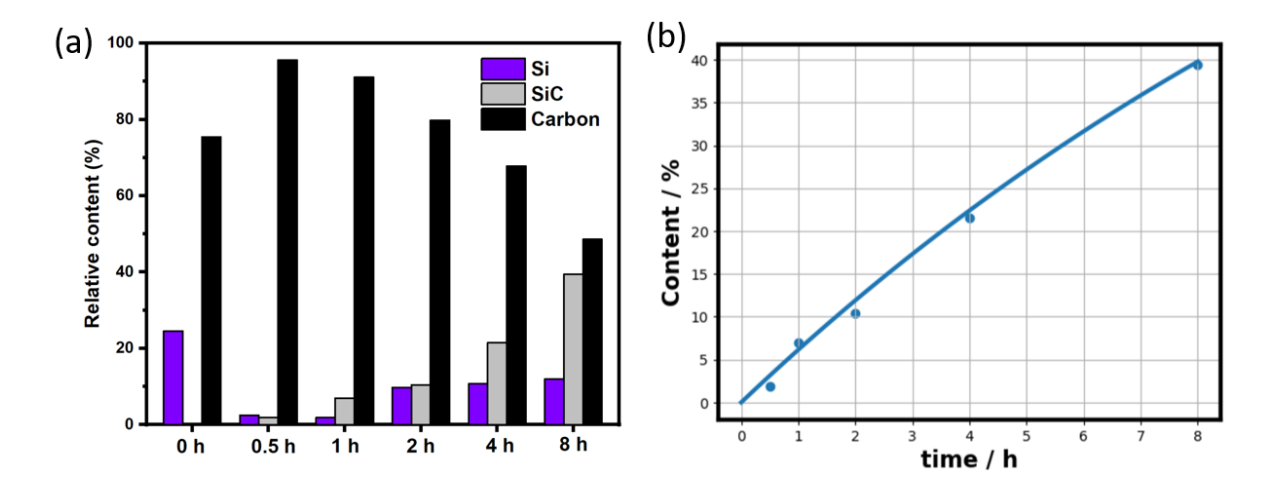


Figure 6.24 (a) evolution of relative content of different species with time; (b) first-order kinetics fitting of SiC. The *MSR* samples are pyrolyzed at 1400 °C.

$$C = \frac{A}{A_0} = (1 - e^{-0.0634t}) \times 100\%$$
 (6.4)

The evolution of Si, SiC, and carbon species heating at 1400 °C throughout the entire heating process is recorded in Figure 6.24(a), where the SiC species grows at 0.5 h of heating time and progresses to increase with longer heating time. This process effectively consumes the graphitic carbon in the samples. The relative content of SiC was fitted with a first-order kinetic expression and shown in Figure 6.24(b) and eq. 6.4, the reaction shows a moderate kinetic rate constant of 0.0634 (k<sub>2</sub>). The slow reaction bonding reaction kinetics can be explained by silicon not melting at this temperature and only reacting with adjacent carbon (Figure 6.22 (a-d)).

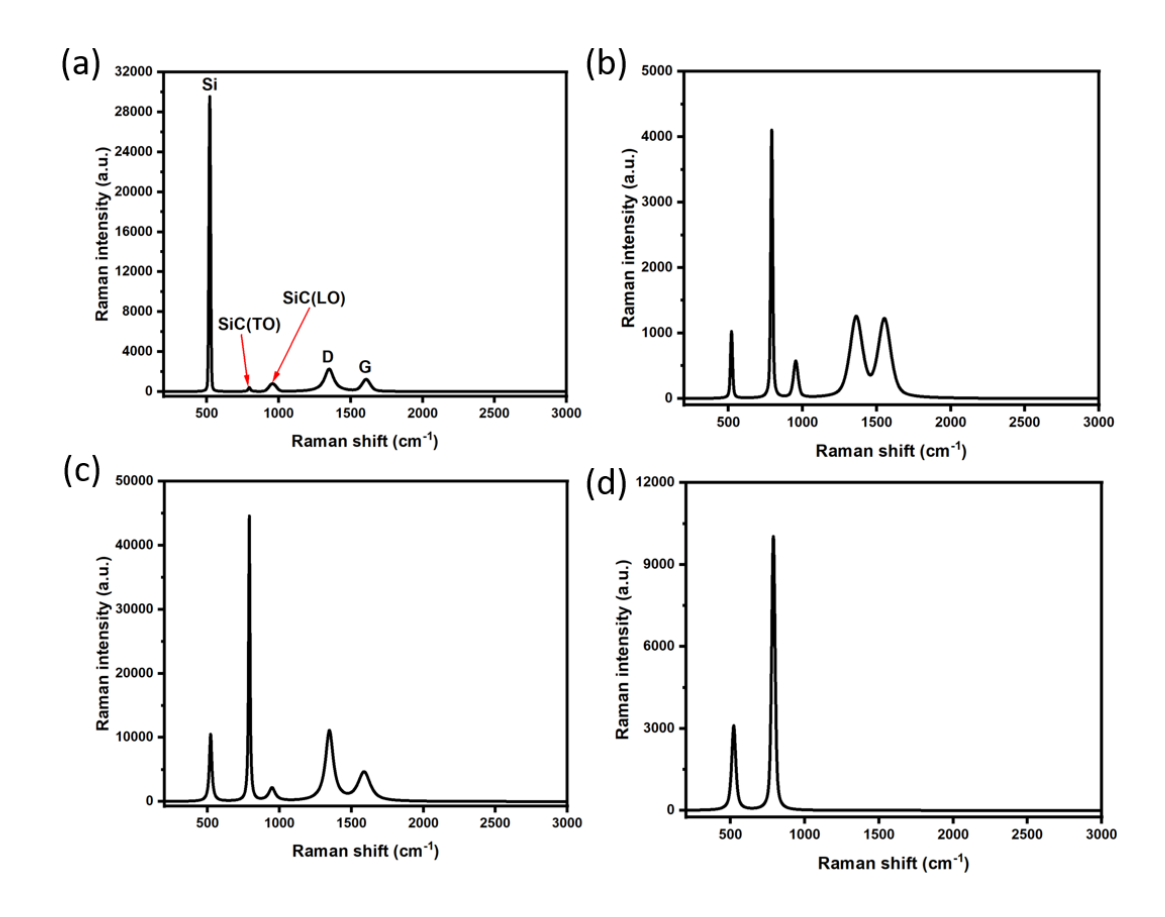


Figure 6.25. *MSR* pyrolyzed *ex-situ* at (a) 1500 °C for 0 h; (b) 1500 °C for 0.5 h; (c) 1500 °C for 1 h; (d) 1500 °C for 2 h.

Figure 6.25 records Raman measurements on *MSR* samples after heating at 1500 °C for different time intervals. The reaction kinetics of the pyrolysis of *MSR* samples was recorded and fitted with first-order kinetics, where the evolution of different species in the samples throughout the heating process was recorded and shown in Figure 6.26.

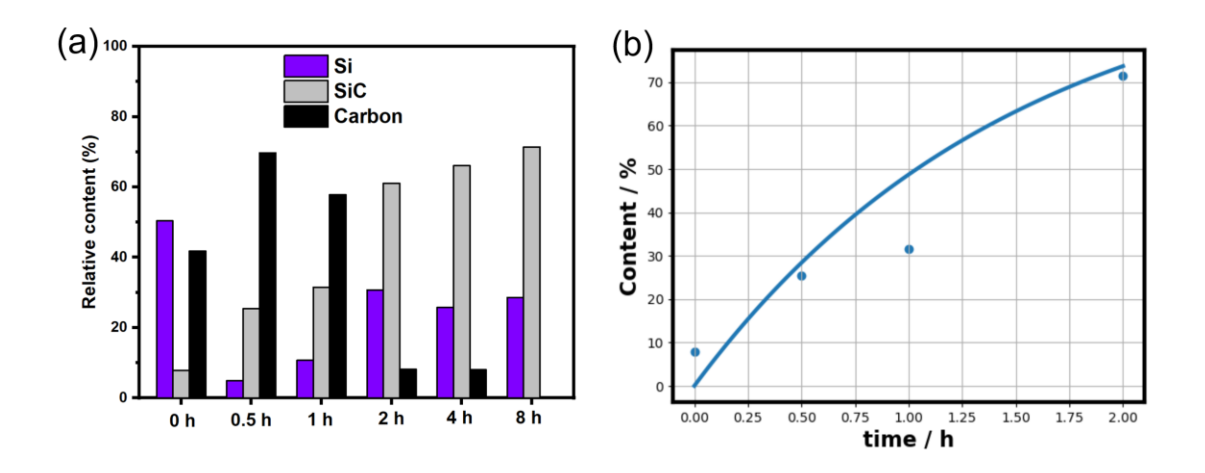


Figure 6.26. (a) Evolution of relative content of different species with time; (b) first-order kinetics fitting of SiC. The *MSR* samples are pyrolyzed at 1500 °C.

$$C = \frac{A}{A_0} = (1 - e^{-0.6677t}) \times 100\%$$
 (6.5)

The evolution of all the species in silicon-based MSR heating at 1500 °C is plotted in Figure 6.26(a), where significant changes in their content are noticed – SiC rapidly grows at the cost of graphitic carbon species, which is evidenced by the high kinetic rate at this temperature ( $k_3 = 0.6677$ ). Eq. 6.5 was a fitting of the relative content of SiC with the first-order kinetic equation, which is plotted in Figure 6.26 (b). Compared to MSR samples heated at 1400 °C, the growth of SiC through reaction bonding is phenomenally more rapid – with more than 10 times higher kinetic rate.

SEM micrographs were taken for *MSR* heated at 1500 °C to investigate reaction bonding and SiC crystal growth (Figure 6.27).

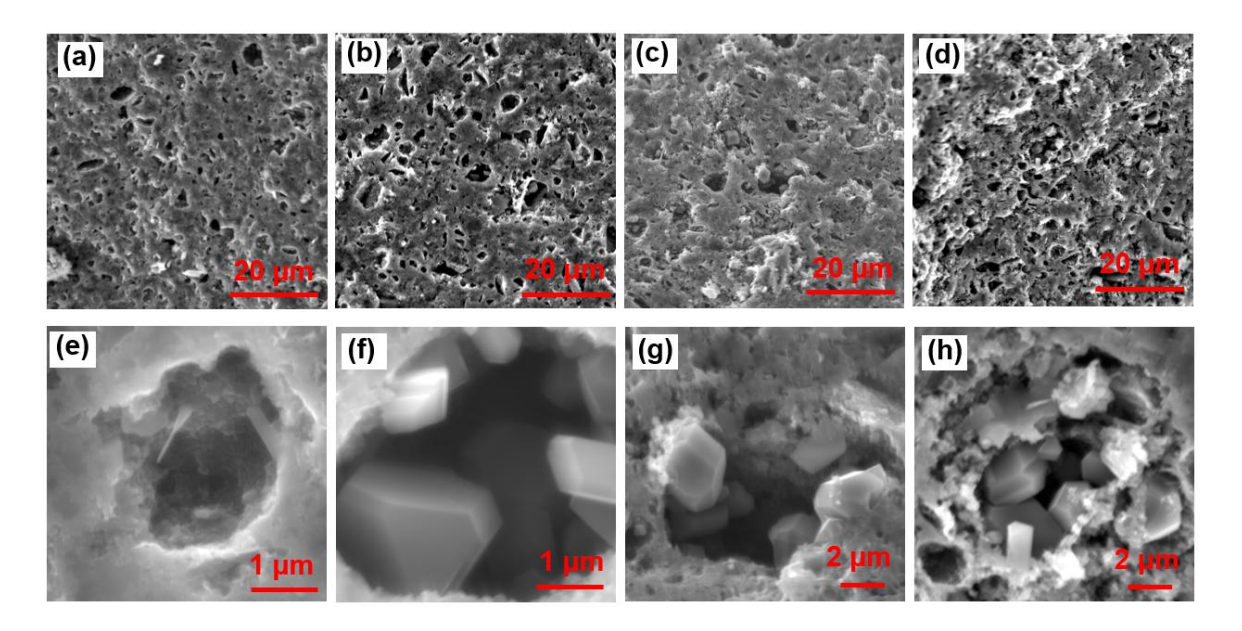


Figure 6.27. SEM micrographs of *MSR* heated at 1500 °C for (a,e) 0 h; (b,f) 0.5 h; (c,g) 1 h; (d,h) 2 h.

From Figure 6.27 (a-d), it can be concluded that pores are being closed when heating for a longer time, and from Figure 6.27 (e-h), it is clear that crystals are generated even at 0 h of heating, and they grow in size upon a longer heating time. The SEM micrographs are good evidence of how fast the reaction bonding is taking place in the sample, and the importance of incorporating silicon nanoparticles into the resin is evident with these micrographs.

#### 6.5. Conclusions

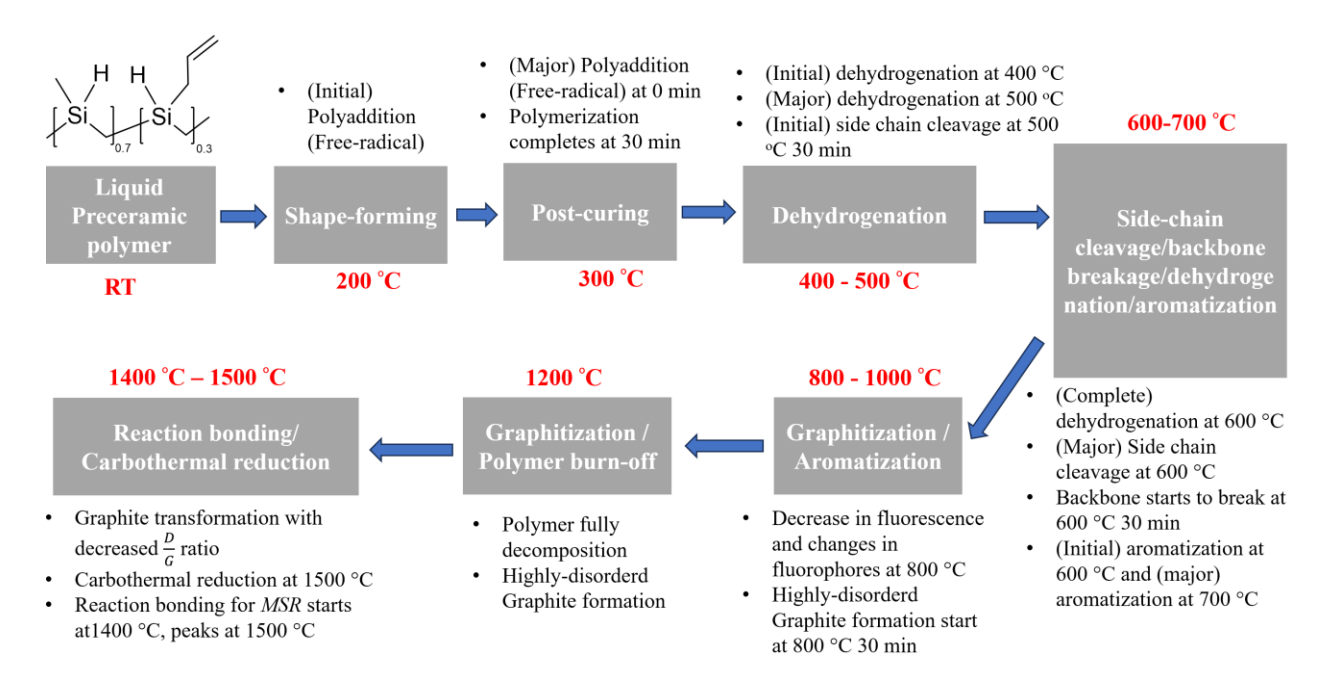


Figure 6.28. Summary of the polymer-to-ceramic transition process.

This study underscores the complementary roles of *in-situ* and *ex-situ* methodologies in comprehensively characterizing the polymer-to-ceramic pyrolysis process. *In-situ* experimentation proved indispensable for elucidating the intricate structural and compositional transformations occurring during this crossover transition. The real-time monitoring capability of this technique effectively fills in the blanks in conventional *ex-situ* methods, which are limited by their prolonged heating and cooling cycles. The innovation of *in-situ* experiments allowed for the detailed observation of sequential transformations, including shape-forming, post-curing, dehydrogenation, chain-reorganization, aromatization, graphitization, and carbothermal reduction (summarized in Figure 6.28), providing a comprehensive, dynamic view of the pyrolysis process that surpasses the limitations of conventional techniques.

Complementing the *in-situ* analysis, *ex-situ* methodologies were employed to investigate the kinetic aspects of the pyrolysis process at higher temperatures when blackbody radiation completely masked the Raman signals. Specifically, carbothermal reduction and reaction bonding were examined. Kinetic analysis revealed a low reaction rate for pure polycarbosilane (PCP) at 1500 °C ( $k_1 = 0.0346$ ). However, the incorporation of a silicon-based resin (*MSR*) demonstrated a substantial catalytic effect, significantly accelerating the carbothermal reduction process. Notably, rate constants of  $k_2 = 0.0634$  at 1400 °C and  $k_3 = 0.6677$  at 1500 °C were observed, indicating a dramatic enhancement in reaction kinetics. The combination of two methods provides a powerful framework for understanding and optimizing PCP pyrolysis by utilizing *in-situ* techniques for detailed structural analysis and *ex-situ* methodologies for kinetic studies at higher temperatures.

This research demonstrates the synergistic potential of combining *in-situ* and *ex-situ* characterization methods. *In-situ* analysis provides detailed, real-time insights into the structural and compositional evolution, while *ex-situ* studies enable the precise quantification of reaction kinetics at elevated temperatures. This combined approach represents a significant advancement in the development of tailored PDC materials, facilitating the control of microstructure and properties through pyrolysis process optimization.

#### CHAPTER 7: ENGINEERING THE PRINTING RESOLUTION OF THERMAL SLA

Parts of this work are adapted from the work of Evelyn Wang and Michael A. Hickner in preparation. This is the version of the article before peer review or editing as submitted by the authors for publication. The publisher is not responsible for any errors or omissions in this version of the manuscript, or any version derived from it.

#### 7.1. Abstract

A significant challenge in thermal SLA is achieving high resolution, as thermal diffusion broadly impacts thermal energy distribution and curing kinetics. This study investigates the influence of resin composition and thermal management on printing resolution in NIR thermal SLA. We analyze the impact of key resin properties, including density, heat capacity, and thermal diffusivity, on the resulting resolution. Furthermore, we examine the effects of laser heating time and active cooling strategies, including convective cooling and resin bed cooling, on mitigating thermal diffusion. Based on the transient heat diffusion equation, a finite element analysis (FEA) model was developed and validated with experimental data. This combined approach allows for a comprehensive analysis of how resin thermal properties and active thermal management influence the printing resolution of the NIR thermal SLA process. The results demonstrate that effective thermal management yielded a resolution of 0.72 mm on the custom-designed thermal SLA printer and a resolution below 100 μm on a modified 3DCeram, Sinto C101 Easy Fab printer.

#### 7.2. Introduction

Tuning the printing resolution is critically important during the thermal SLA process<sup>124,152</sup>. Especially because, unlike the more industrialized UV-based SLA, it is difficult to

confine the thermal energy of high-intensity lasers to a small region<sup>124</sup>. Thermal SLA printing suffers from low printing resolution and lower resin stability due to intrinsic limitations stemming from its 2-3 orders of magnitude higher energy density than UV-based printing<sup>124,153</sup>. This concentrated thermal energy in localized spots reduces resolution, a stark contrast to conventional UV-based SLA technology, where most printers have an energy density of 1 mJ/cm<sup>2</sup> to 10 mJ/cm<sup>2</sup>, which dissipates efficiently during the entire printing process<sup>90,230</sup>. Furthermore, the absence of thermal initiators in UV-based resins enhances their resistance to high local temperatures and thermal diffusion<sup>231</sup>. This thermal diffusion and high local temperature pose a major challenge to high-resolution thermal SLA because the high energy density is difficult to manage, and thermal initiators in the resin exacerbate over-curing by facilitating the polymerization process, further reducing resolution<sup>232</sup>.

Currently, thermal SLA achieves only millimeter-level accuracy (Chapter 3-5), while UV-based methods already achieve micron-sized resolutions. UV light scattering is the primary factor affecting the printing resolution during the UV-SLA process<sup>38,86</sup>. Thermal SLA resolution is limited by thermal diffusion. This impacts overall accuracy and fidelity because fewer methods exist to control thermal diffusion in the laser-projected area<sup>124</sup>. Therefore, effective methods to improve thermal printing resolution are of utmost importance. This report investigates three methods to control thermal diffusion: tuning the resin's thermal conductivity (k), convective cooling with forced argon flow, and coolant circulation to maintain the resin pool temperature. The first method involves adjusting resin composition, while the latter two focus on active cooling of the resin pool and printed structures. After projecting the laser onto the printing media, the light absorbers in the resin will absorb the thermal energy and use the energy to start

polymerization. While excess heat will escape the printing region, thermal temperature management is critical in confining that excessive heat in localized regions, which helps determine the final part's fidelity and resolution.

Thermal conductivity is crucial in SLA printing resins because it directly influences thermal diffusion within the resin during the printing process<sup>233</sup>. The phonon mean free path primarily determines the thermal conductivity, as heat capacity and sound velocity are relatively fixed intrinsic material properties<sup>234</sup>. Polymers inherently have a small phonon mean free path due to their amorphous structure, making it difficult for phonons to travel through the material. While some high-k polymer fibers exist, they are impractical for 3D printing resins. Therefore, thermally conductive particles are often added to the resin to enhance thermal conductivity and control thermal diffusion<sup>235</sup>. The rule of mixture indicates that a higher concentration of these particles, such as the silicon nanoparticles used in this research, creates more phonon-conducting pathways<sup>236</sup> (Figure 7.1), leading to a higher overall k of the composite and, thus, more precise control over thermal energy spread<sup>213</sup>.

Thermal conductivities are controlled and affected by the phonon scattering in the sample, eq.  $7.1^{234}$ :

$$k = \frac{1}{3} c_{v} \cdot v \cdot l \tag{7.1}$$

where  $c_{\nu}$  stands for volumetric heat capacity, l is the mean free path of phonons in the sample, and  $\nu$  denotes the speed of sound.

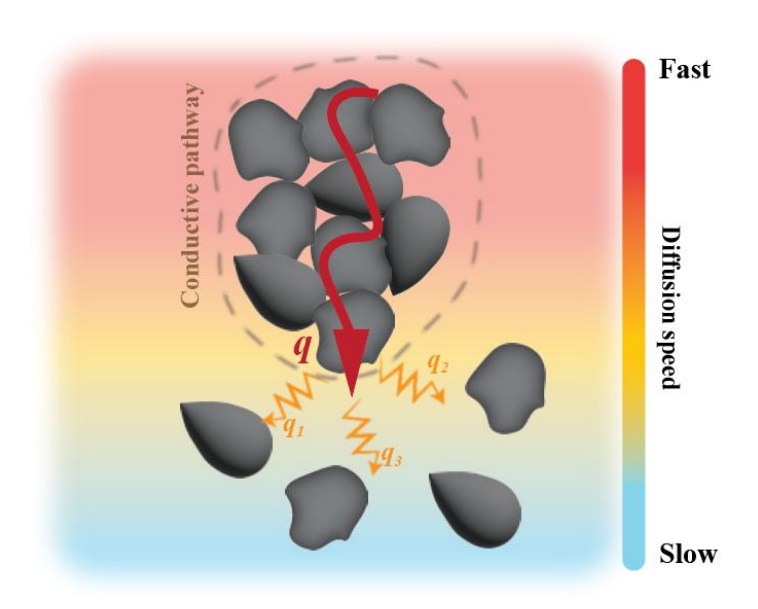


Figure 7.1. Phonon transport in polymer composite.

FEA offers a powerful and efficient computational approach for optimizing 3D printing processes like SLA<sup>237</sup> and SLS<sup>238</sup>. FEA provides critical insights into thermal management, which is crucial for controlling the printing process and enhancing resolution. By simulating heat transfer, the material's thermal response, and the cooling process, FEA models enable precise control over the thermal aspects of printing<sup>238</sup>. Key parameters, including laser settings (power, speed), cooling effects, material properties (k, heat capacity, density), and build platform temperatures, can be systematically investigated and optimized through the model. Data can be fitted with an analytical model to improve predictability. Consequently, FEA significantly enhances the SLA printing process by reducing the need for costly and time-consuming trial-and-error experimentation, ultimately improving print fidelity and resolution<sup>237</sup>.

This research employs a synergistic approach combining experimental measurements and analytical modeling to elucidate the critical factors governing thermal printing resolution in SLA. The analytical models, validated against experimental data, serve as predictive guides for

optimizing and interpreting the experimental design. Specifically, insights derived from the models informed the implementation of two distinct active cooling strategies to minimize thermal diffusion and thereby maximize printing resolution. Applied to our custom-built system, these strategies yielded the best resolution of 0.72 mm. Furthermore, this work is in collaboration with 3DCeram, Sinto. Utilizing their C101 Easy Fab printer and incorporating tailored thermal management techniques based on our modeling results, we achieved a significantly enhanced resolution of under 100 µm, which is approaching the resolution of UV-based SLA printers. This demonstrates the effectiveness of combining analytical insight with practical implementation to advance the precision of thermal SLA printing.

### 7.3. Experimental section

#### 7.3.1. Materials

The chemicals and materials used in this report are shown in section 5.3.1, where acrylate-modified siloxane RMS-992 ((Methacryloxypropyl)methylsiloxane, 95 - 100%, Gelest, Morrisville, PA) was added as both crosslinker and PCP, SMP-877 (Starfire Systems, Glenville, NY) resin was chosen as the main PCP and dicumyl peroxide (Sigma-Aldrich, 98%, St. Louis, MO) was mixed as the thermal initiator for thermal printing. Carbon black (1 wt%, Sigma-Aldrich, 24 nm, St. Louis, MO) was added into resin only for testing at 3DCeram, Sinto's printers. Silicon nanoparticles (500 nm, US nano, Houston, TX) were homogeneously blended into the resins with a FlackTek speed mixer (Greenville, SC) with a two-step mixing procedure. First, the resin and nanoparticles are mixed under ambient pressure with a spinning speed of 1000 RPM for 1 min. Then, the mixture is subsequently mixed under a 6.7 kPa vacuum with a spinning speed of 2000 RPM for 3 min. All the resin compositions are listed in Table 7.1.

Table 7.1 Resin compositions used in this report.

Components	GRR	MSR	SRR	HSR	877 RMS	877
RMS-992 / wt%	34.88	32.39	29.91	27.35	49.75	0
SMP-877 / wt%	34.88	32.39	29.91	27.35	49.75	99.01
Dicumyl peroxide / wt%	0.35	0.32	0.30	0.55	0.50	0.99
Silicon (500 nm) / wt%	29.90	34.89	39.88	44.75	0	0

Note: *GRR*: graphite-rich resin (lowest silicon content); *MSR*: medium silicon resin (medium silicon content); *SRR*: silicon-rich resin (high silicon content); *HSR*: high-silicon resin (highest silicon content); *877 RMS*: resin composition without silicon content; *877*: pure PCP without crosslinkers and silicon.

### 7.3.2. Characterization

DSC thermograms were taken with a DSC Q2000 (TA instrument, New Castle, DE) to analyze polymerization temperatures. Thermal measurements were taken with a C-THERM Trident systems (Fredericton, NB, Canada) equipped with a Modified Transient Plane Source (MTPS, ASTM D7984) sensor. An Archimedes density measurement setup (Mettler Toledo density kit, ASTM B962-17) was used to obtain the samples' densities after pyrolysis. The optical power of the NIR laser is measured with a thermal sensor (Thorlabs, Newton, NJ, S442C heat sink with power meter console). Thermal images are taken with a thermal camera (Teledyne FLIR E8, Wilsonville, OR).

# 7.3.3. Analytical model

In the analytical model, we consider NIR laser printing a simple 2D transient heat transfer model, where the laser moves in a line and heats that line. A temperature distribution will occur due to thermal diffusion, which is illustrated in Figure 7.2.

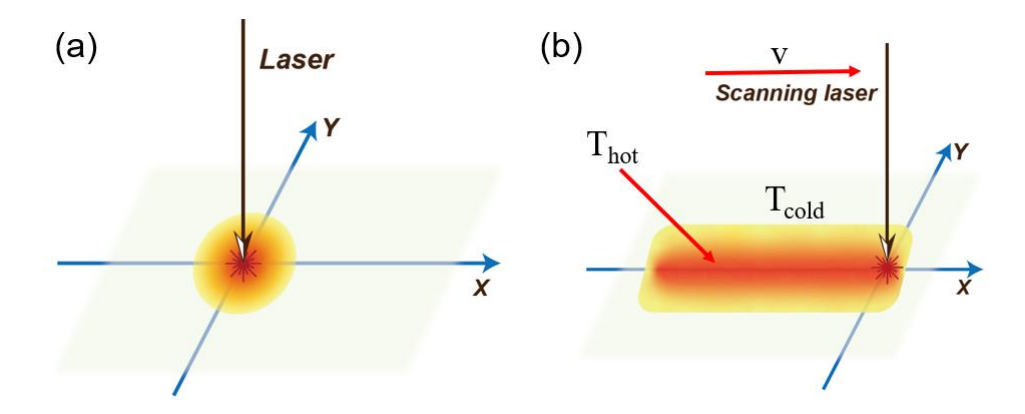


Figure 7.2. (a) NIR laser project onto resin pool; (b) NIR laser scanning through the resin pool.

The first assumption in the model is that upon the laser irradiation onto the resin surface, the laser will immediately transfer its optical power into the resin by absorption. Since thermal energy will diffuse into the surrounding area, there will be a distribution of temperature in the radial direction (Figure 7.1(a)). Scanning the laser across the resin surface will leave behind a trail of heated area (Figure 7.1(b)). The laser instantly delivers its optical power to the resin and heats up the hot center region to  $T_{hot}$  (150 °C (measured with thermal camera FLIR E8)), while the hot region diffuses heat into the cold ( $T_{cold}$ ) surrounding regions.

In order to fit this into an easy-to-understand analytical model, we can simplify the model by placing a hot area in the middle and applying the transient heat transfer equation<sup>239</sup> (eq. 7.2) to the entire region.

$$\rho C_{p} \frac{\partial T}{\partial t} = \nabla * (k \nabla T) + Q \tag{7.2}$$

Where  $\rho$ ,  $C_p$ , k, and T symbolize the density, specific heat capacity, thermal conductivity, and resin temperature; t is the time, and Q stands for the internal heat source (NIR laser).

The second assumption is that the material is homogeneous and isotropic. The second assumption for the model is that the material's thermal conductivity remains at different

temperatures. Therefore, a simplified version of the transient heat transfer equation can be expressed in eq. 7.3.

$$\rho C_{p} \frac{\partial T}{\partial t} = k \left( \frac{\partial^{2} T}{\partial x^{2}} + \frac{\partial^{2} T}{\partial y^{2}} \right) + Q$$
 (7.3)

The third assumption is that only the resin above polymerization temperature  $T_p$  will polymerize and become the "printed parts" during a thermal SLA process. The polymerization temperature is recorded with DSC, which is 97.9 °C, as shown in Figure 7.3.

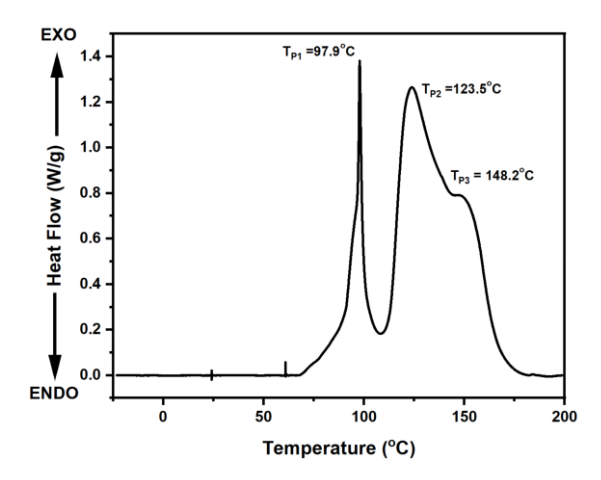


Figure 7.3. DSC spectrum of *MSR*.

The DSC curve of the resin was run under nitrogen flow (50 cm³/min), with a ramp rate of 5 °C/min from 0 °C to 200 °C. The sharp peak at around 97.9 °C (T<sub>P1</sub>) denotes the polymerization peak of acrylate groups, which indicates the resin will begin to cure above this temperature.

In the analytical model, we assume that the laser only scans through the surface of the resin in a straight line and immediately heats up the local area under NIR laser irradiation. The heated region will serve as the hot source, which diffuses heat into the surrounding regions

(uncured resin acts as a heat sink). MATLAB was used to calculate and plot the analytical model's results.

During the simulation, the input parameters are k, density and heat capacity of the resin, temperature of the hot region (which is the region from laser heating,  $T_{hot}$ ) and cold region (uncured resin as the heat sink,  $T_{cold}$ ), hot region width (which is measured as 0.5 mm), time after heating (duration of simulation, t).

# 7.3.4. Thermal printing parameters

Printing tests were done with the following parameters: 24 mm/s for wall print speed, 40 mm/s for infill speed, 1 mm line width with grid infill pattern, and test printing layers of 45 mm  $\times$  45 mm rectangular blocks.

The energy density can be calculated according to eq. 3.1. During the wall printing process (scanning speed 24 mm/s), the energy density equals 39.58 J/cm<sup>2</sup>, and during the infill printing process (scanning speed 40 mm/s), it equals 23.75 J/cm<sup>2</sup>.

The printing resolution was demonstrated with a single line printing, which was performed with laser scanning through (24 mm/s) the surface of the resin in a straight line. The cured resin was taken out of the resin pool, and the width of the resin was measured to give line width values.

#### 7.4. Discussion

The active cooling method consists of a forced argon connection for resin surface cooling and water circulation for resin pool thermal management. Convection cooling of the resin pool was first considered, and it was analyzed experimentally and analytically to determine how it affected the printing resolution.

## 7.4.1. Experimental data on active cooling

Active cooling methods during the thermal SLA affect the resolution by controlling the temperature of the resin pool and printing area; the results of these two active cooling methods are displayed in Figure 7.4. Thermal diffusion in the resin vat will affect the printing resolution as the excess resin area will be cured. Argon gas was projected at 370 kPa, and the circulating water was kept at 25 °C.

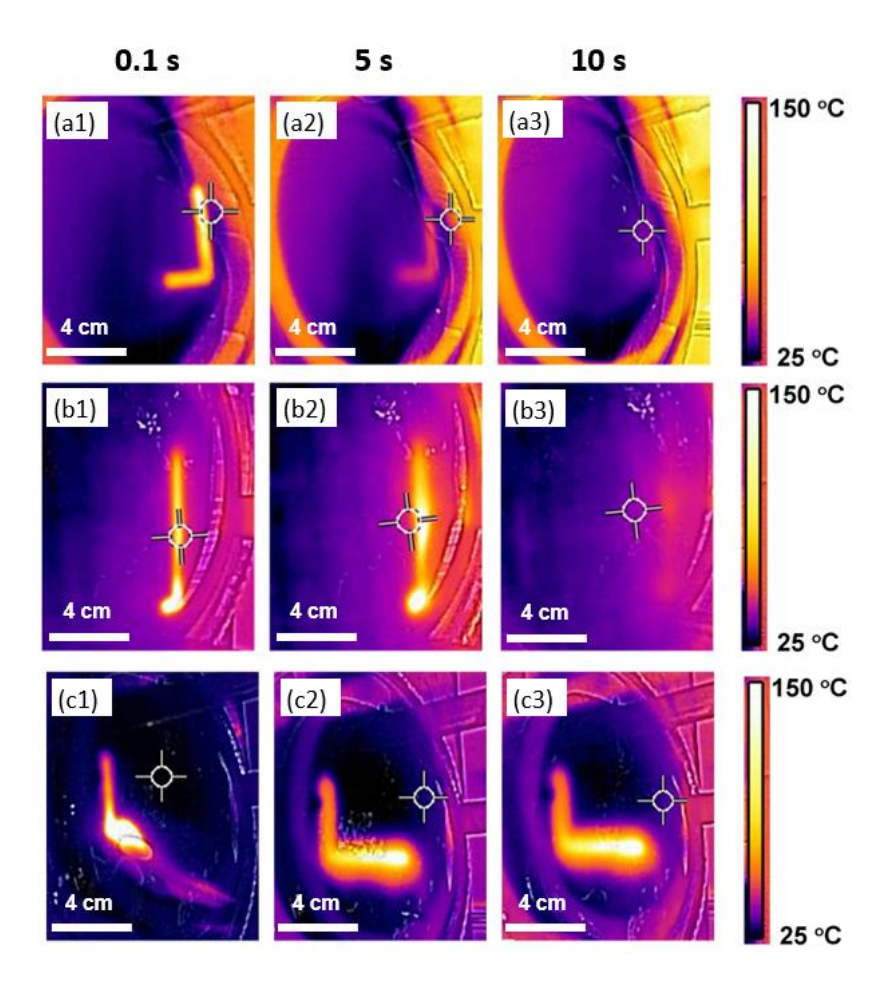


Figure 7.4. Real-time thermal images captured by FLIR E8 camera. (a1,a2,a3) are shown printing with both active cooling methods; (b1,b2,b3) are shown printing with only forced argon convection (active cooling); (c1,c2,c3) are shown printing with no cooling effects. Digital photos are taken for printing after 0.1 s (first column), 5 s (second column), and 10 s (third column).

A clear distinction between the printing with and without active cooling methods is shown in Figure 7.4, where the printing of a 45 mm  $\times$  45 mm square without infill was demonstrated (wall printing speed 24 mm/s, laser optical power 4.75 W). Figure 7.4(a1,a2,a3) shows the changes in thermal profiles after the NIR laser scan across the resin surface after different time intervals, where both active cooling methods were applied. It is clear that after 5 seconds, there is only minimal lingering heat (residual thermal energy) left in the resin pool, and no obvious heat diffusion into the non-printing area was observed. After 10 s, most of the lingering heat was removed, and there was only negligible thermal history in the resin pool. As a result of active cooling, there is a minimal amount of thermal diffusion, and the printing resolution was optimized to  $0.72 \pm 0.03$  mm. When there is only forced argon convection cooling alone, results are displayed in Figure 7.4(b1,b2,b3) – similar results are obtained compared to printing with both active cooling methods. Nevertheless, more lingering heat at 5 s and moderate thermal diffusion into non-printing areas were observed on both 5 s and 10 s. Finally, when it comes to thermal printing without any active cooling methods, significant thermal diffusion and lingering heat were observed in Figure 7.4(c1,c2,c3). The thermal diffusion into the non-printing area heated up a much larger area than the printing area, significantly lowering the resolution  $(1.98 \pm 0.08 \text{ mm}).$ 

### 7.4.2 Analytical results from active cooling

When the thermal energy is not removed in a timely fashion from the resin, the heat will continue to diffuse into the surrounding area. This lingering heat is the main culprit for lowering the thermal printing resolution. The effect of heating time was analyzed using the analytical model to determine how detrimental the lingering heat and higher k are to printing resolution.

The effect of lingering heat is plotted in Figure 7.5, and the detailed data about lingering heat effects are plotted in Figure 7.10.

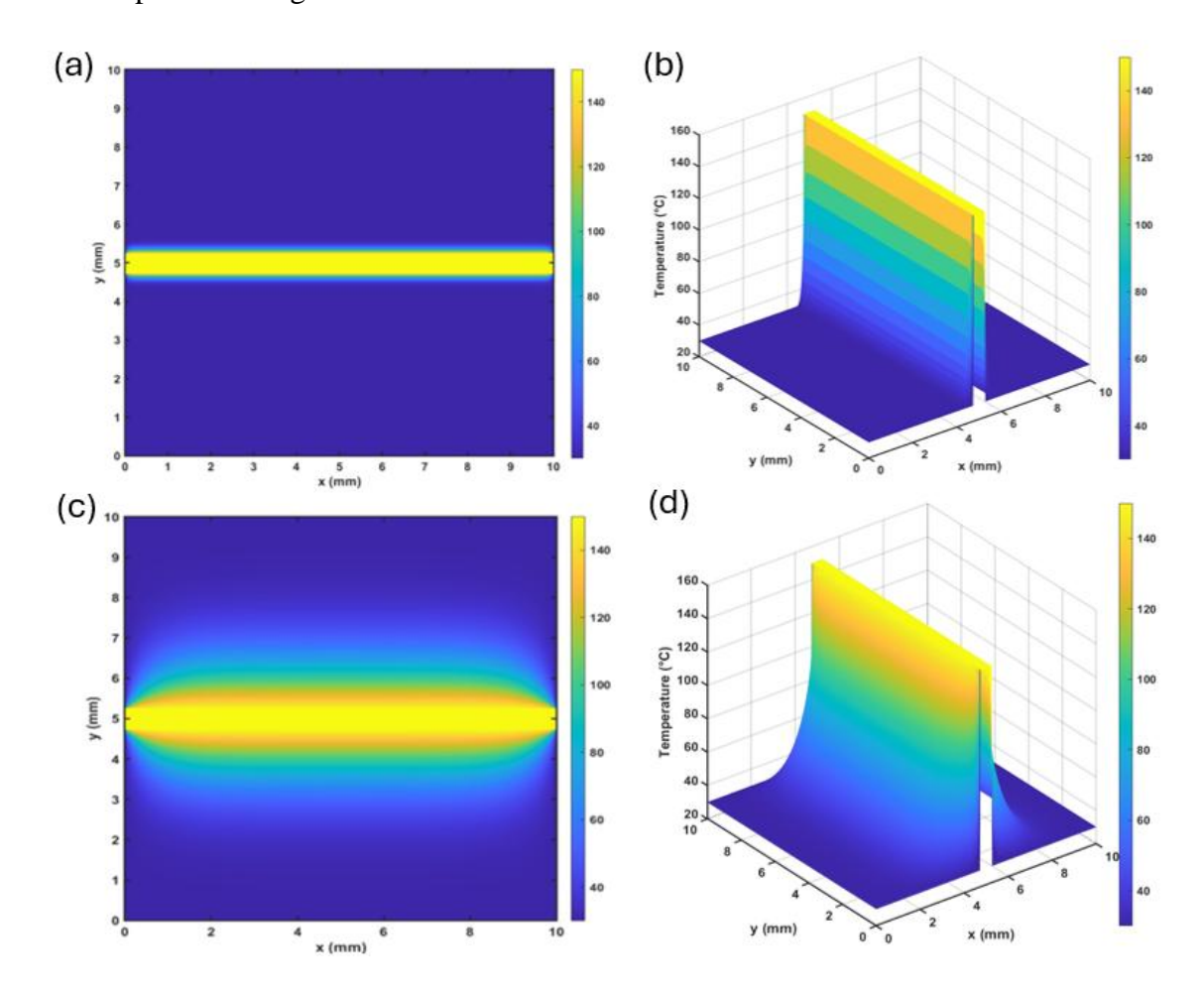


Figure 7.5. 2D and 3D view of thermal energy distribution on resin (*MSR*) surface from the analytical model after (a, b) 0.1 s; (c, d) 10s.

It can be concluded from Figure 7.5 that the longer the excess heat stays on the resin pool surface, the worse the printing resolution will be, which stays true for all resin types (Figure 7.10). When the lingering heat is not removed for up to 10 s, the line width will increase significantly (by 207.7 %) as larger areas are heated above their polymerization. The results from the analytical model again exemplify that rapidly removing the lingering heat during the thermal

printing process will notably facilitate a high-resolution process. This aligned with the observation in experiments (Figure 7.4) – forced argon convection cooling removes the residual heat and maintains a high resolution.

# 7.4.3 Experimental data on bed temperature

Resin bed temperature is crucial in controlling the thermal printing process, controlled with coolant circulation cooling for the resin pool. This is exemplified in Figure 7.6, where clear differences were observed during the printing process with and without resin pool cooling.

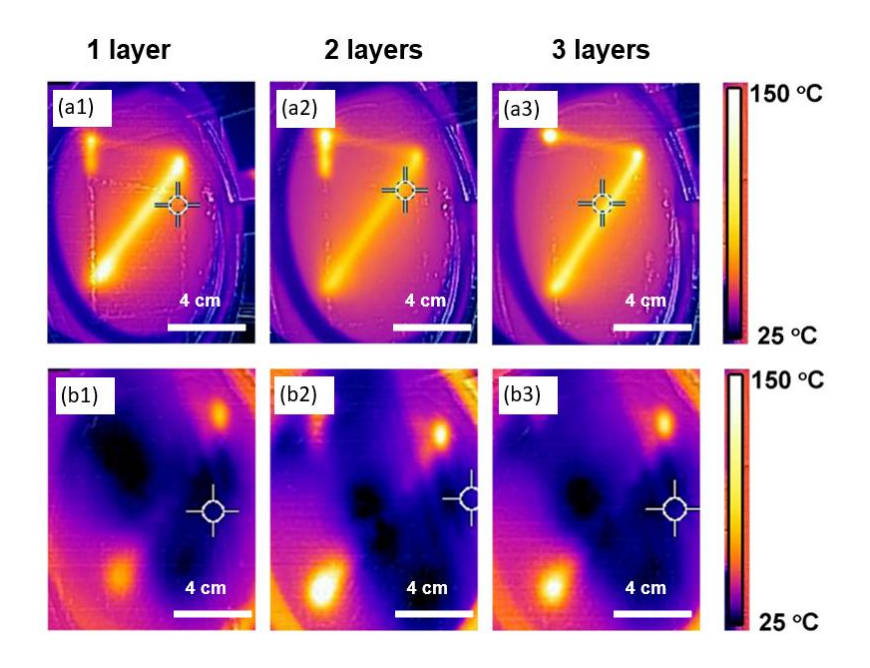


Figure 7.6. Real-time thermal images captured by FLIR E8 camera. (a1,a2,a3) are shown printing with no active bed cooling; (b1,b2,b3) are shown printing with bed cooling. Digital photos are taken 0.1 s after the printing (immediately after printing). *MSR* was demonstrated for printing.

Test printing blocks of  $45 \text{ mm} \times 45 \text{ mm}$  were printed, and 3 layers were printed to monitor the bed temperature dynamics. Printing of each layer takes 116 s, and subsequent layers are built on top of each other, where the thermal images are recorded after 0.1 s. It is also clear in

Figure 7.6(a1,a2,a3) that the resin bed temperature increases after elongated printing, and the heat is trapped inside the resin pool. On the contrary, when the resin pool is under bed cooling, the residual heat can be rapidly removed, even after multiple layers (Figure 7.6(b1,b2,b3)). After printing each layer, there is only a minor increase in the bed temperature.

After extended printing periods, the resin pool temperature will increase. The initial temperature of the resin pool is 25.0 °C, while after printing one single layer, it rises to 34.3 °C. Such a sharp increase in the resin pool temperature will lead to a lower printing resolution, as higher bed temperatures will make it easier to heat up the resin to polymerization temperature, as discussed in the following session.

## 7.4.4 Analytical results from bed temperatures

The bed temperature (heat sink temperature  $T_{cold}$ ) was chosen as input in the analytical model (with 5s lingering heat); we can get the calculated line width versus the bed temperature (Figure 7.7) for analyzing how resin temperature affects the printing resolution.

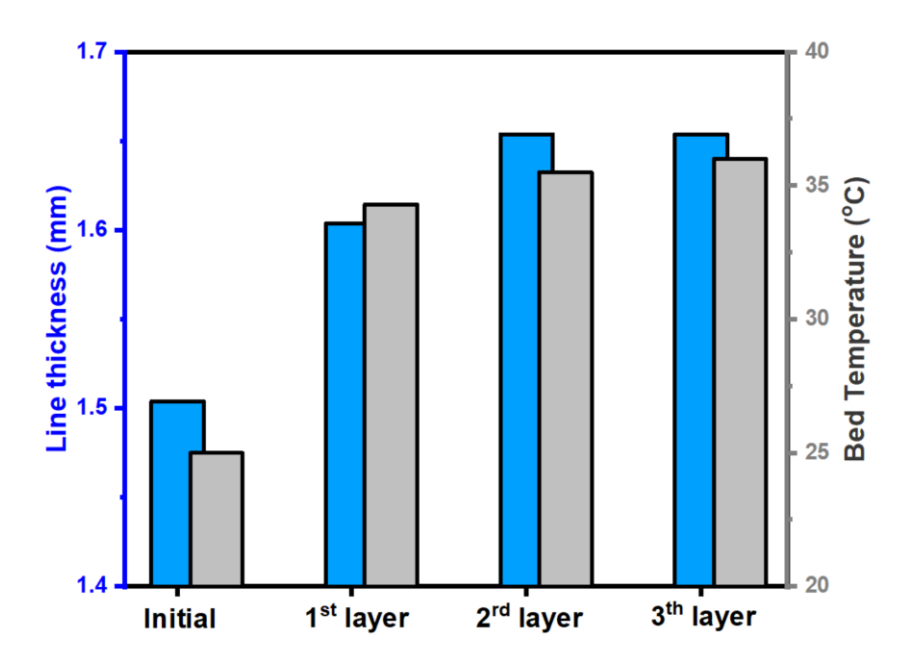


Figure 7.7. Effects of resin bed temperature on thermal printing resolution.

Figure 7.7 demonstrates that higher bed temperatures increase line width. Additionally, there is a large increase in both bed temperature and line width after printing the first layer. The results show that controlling the resin bed temperature effectively lowers thermal diffusion and optimizes printing resolution. This aligns with the results from the analytical model in Figure 7.6, which demonstrates that coolant circulation effectively removes excess heat from the resin bed and maintains consistently high printing resolution.

# 7.4.5. Resin thermal properties

After optimizing the system engineering control methods, both active cooling methods were applied during printing to analyze the influence of k. Resins with higher k are more effective at dissipating the thermal energy from the NIR laser. Since k is positively related to particle loading, a series of resins with different silicon nanoparticle content are synthesized and tested for printing resolution.

The thermal effusivity of the pyrolyzed samples is measured using the modified transient plane source (MTPS) method. The resins' heat capacity is measured using DSC at 25 °C with a ramp rate of 5 °C/min from 0 °C to 100 °C under Nitrogen flow (50 cm<sup>3</sup>/min). The densities of the pyrolyzed samples are calculated using the rule of mixture in eq. 7.5.

$$\rho_{c} = \sum_{i=1}^{n} V_{i} \rho_{i} \tag{7.5}$$

Where  $\rho_c$  stands for the density of the composite resin,  $V_i$  means the volumetric fraction of component i, and  $\rho_i$  is the individual density of component i.

Thermal conductivities are calculated from thermal effusivity values with eq. 7.6.

$$e = \sqrt{k\rho C_P} \tag{7.6}$$

Where e is thermal diffusivity,  $\rho$  means density, and  $C_P$  represents heat capacity.

# 7.5. Results

## 7.5.1. Experimental results

Resins with different silicon nanoparticle loadings were fabricated and tested with the NIR thermal printer. Figure 7.8 demonstrates the relationship among resin particle loadings, k, and printing resolution.

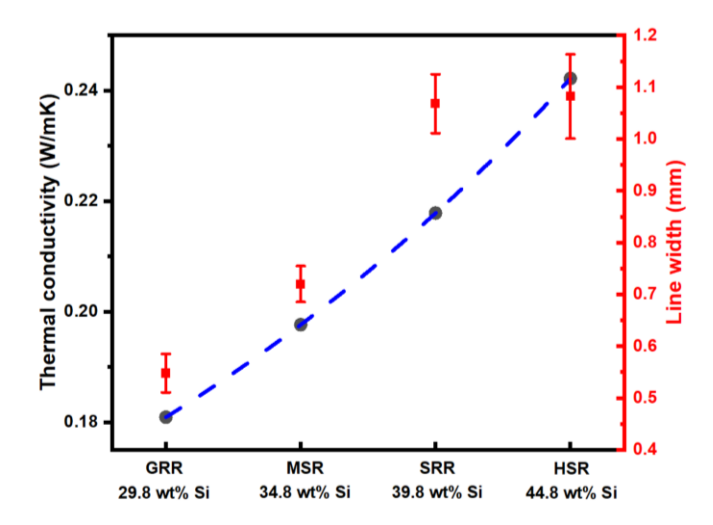


Figure 7.8. The relation between the particle loadings, k, and the printed line width.

The k of the resin composition increases from 0.18 W/mK to 0.24 W/mK from lowest to highest silicon loadings, whereas the measured line width increases from  $0.55 \pm 0.04$  mm to  $1.08 \pm 0.08$  mm. It can be concluded from Figure 7.8 that the thermal conductivity of resin increases with silicon loading, which also positively relates to the line width/printing resolution of thermal printing. There is a sharp increase in the k when the silicon solid content increases from 34.8 wt% to 44.8 wt%, denoting there is a steep increase in the phonon conduction pathways. The silicon nanoparticles in the printing resin are reaching the percolation limit, during which the interconnected silicon bridges in the resin facilitate phonon transport.

This phenomenon is aligned with the observation in the printing line width measurement – the sudden increase in the thermal conductivity from 34.8 wt% to 39.8 wt% silicon loading led to a sharp increase in the line width from  $0.72 \pm 0.03$  mm to  $1.07 \pm 0.06$  mm. Additionally, the general trend is consistent with our hypothesis that higher silicon loading will lead to higher k. Meanwhile, a higher k will subsequently cause a lower printing resolution (thicker linewidth).

Figure 7.9 displays the printed line, demonstrating the printing resolution. It clearly visualizes the line width of resins with different k.

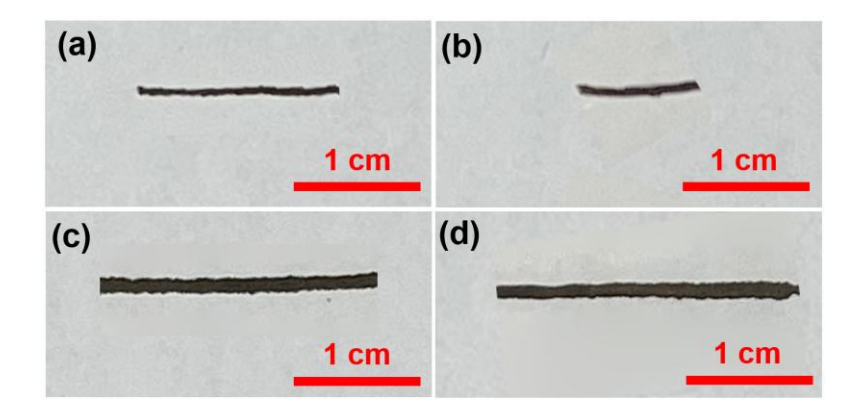


Figure 7.9. Line width resolution testing of (a) GRR; (b) MSR; (c) SRR; (d) HSR.

Figure 7.9 shows the line width of resins with different thermal conductivity, the values of which are shown in Figure 7.8. It can be concluded that a higher particle loading will lead to lower printing resolutions, especially when the particle loadings increase from 34.8 wt% (*MSR*) to 44.8 wt% (*HSR*).

### 7.5.2. Analytical model results

The heat capacity  $c_p$ , densities  $\rho$ , and k of the resin were chosen as input in the analytical model. The line thickness was tested under different simulation times, where the effect of resin thermal conductivity was quantified and plotted in Figure 7.10.

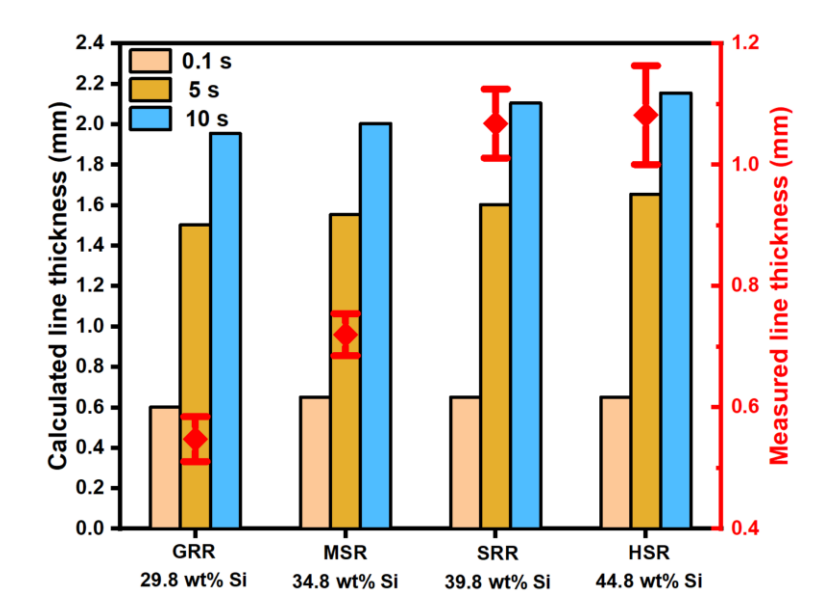


Figure 7.10. Measured line thickness and calculated line thickness from the analytical model.

Figure 7.10 illustrates that higher k leads to heat conduction and faster thermal diffusion into the surrounding regions. Additionally, longer heating time in the analytical model drastically increases the line width and thus lowers the printing resolution. Resins with higher k values result in wider printed lines for a given simulation time. This aligns with the trends observed in our analytical model and experimental results. Moreover, extended heating periods degrade printing resolution regardless of the resin used, as previously explained.

## 7.5.3. Thermal printing with 3DCeram, Sinto

The optimized resin composition was adapted and blended with 1 wt% carbon black for thermal printing at 3DCeram, Sinto (Grand Ledge, MI) with C101 Easy Fab SLA printer. The setting for the printing is  $300 \text{ mJ/cm}^2$ , 1 mm/s printing speed, 75  $\mu$ m hatch spacing, line pattern, and 25  $\mu$ m offset to counter the thermal diffusion. Only natural convective cooling is adapted as limited modification can be applied to the industrialized printer. However, the small laser spot size (50  $\mu$ m) combined with convective cooling helps maintain the high resolution (Figure 7.11).

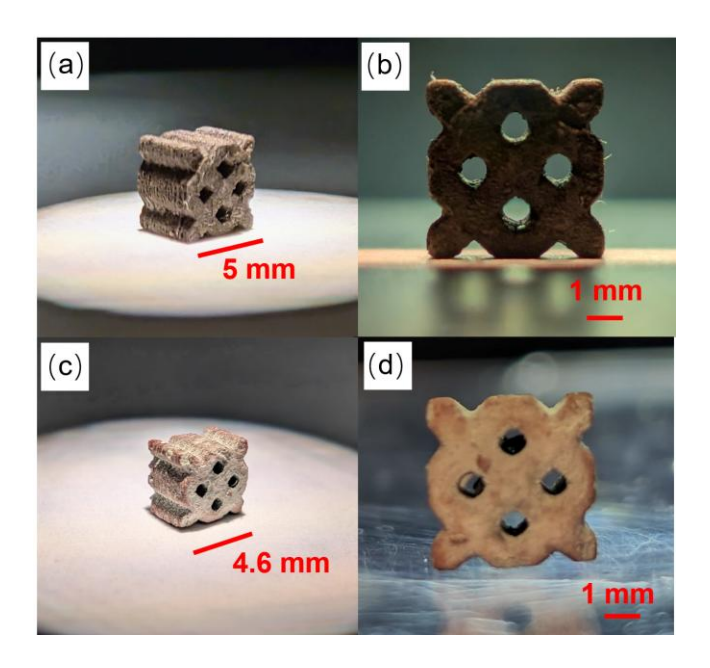


Figure 7.11. Digital picture of (a,b) thermally printed lattice, green body; (c,d) as-printed lattice after pyrolysis. The pyrolysis procedure is the same as reported in Chapter 5.

Figure 7.11 shows that the lattice after printing showed excellent layer-to-layer adhesion and dimensional fidelity. The sample, after printing, has a resolution under  $100 \mu m$ , rivaling UV-based printing for ceramics. The as-printed samples after pyrolysis demonstrate an 8% linear shrinkage, which also helps maintain the structural integrity of the lattice.

### 7.6. Conclusions

The current research combines experimental data and analytical model results to yield the best combination for optimizing thermal SLA printing resolution. The current analytical model is based on a 2D transient thermal diffusion model, which considers experimentally measured data cp,  $\rho$ , k, and laser parameters. The results of the analytical model align well with the experimental results – active cooling methods rapidly cool down the printing region and resin pool, which helps maintain high resolution; high resin k negatively affects the printing resolution by inflicting higher thermal diffusion. Finally, resin with a relatively lower k was chosen for

printing, as certain particle loading needs to be maintained to optimize the properties after pyrolysis. Two active cooling methods – forced argon convection cooling and resin pool water circulation cooling, were applied during printing to yield the best results.

However, the analytical model also has drawbacks. The current model only considers the thermal diffusion of the laser-heated area in a 2D scenario, where the thermal diffusion in the depth will also influence the resolution. Moreover, the model only takes k and active cooling into consideration. Other factors, including resin convection and laser power distribution, affect the resolution during the printing process. Finally, the assumptions that k,  $c_p$ , and  $\rho$  remain constant throughout the process will also affect the model outcome.

Overall, the current analytical model paved a clear path for determining how to control the printing resolution of thermal SLA. In the research, both inner factors (resin k) and outer factors (active cooling methods) were analyzed and optimized to obtain the best printing resolution of  $0.72 \pm 0.03$  mm in our thermal SLA printer and under 100  $\mu$ m resolution with 3DCeram, Sinto's C101 East Fab printer.

## **CHAPTER 8: CONCLUSION**

This dissertation centers around developing and progressing the thermal SLA method for AM of SiC-Composite ceramics, where the materials and 3D printing techniques are discussed in detail.

For the 3D printing technique, thermal SLA, this dissertation starts from developing thermal SLA for 2D printing, 2.5D lattice printing, 3D overhang structures printing, and micron lattice printing. Throughout the development of this technology, materials with finer structures and fidelity were achieved, where the resolution was tuned down all the way from 2mm to under 100 µm. The definition, wall thickness, overhang structures, and accuracy are significantly improved throughout the entire research, from Chapter 3 to Chapter 7. Additionally, optimization methods, including resin recoating, active cooling thermal management, and resin composition optimizations, are utilized in the current study. As a result, optimized methods were developed for our own designed thermal SLA printer, and a proof-of-concept high-resolution thermal SLA printing display was accomplished at 3DCeram, Sinto (Chapter 7).

The materials development in this dissertation has two parts: developing resin compositions for thermal SLA and densification methods for high-performance SiC-Composite ceramics, characterization of these materials, and in-situ study of the polymer-to-ceramics transition process.

For the first part of the research, resin compositions based on acrylate, siloxane, and polycarbosilanes are employed for crosslinking and making green bodies from thermal SLA. All the resin compositions have a large amount of ceramic filler (up to 50 wt%) – passive fillers like SiC directly increase the ceramic yield and properties of the resulting Composite ceramics;

active fillers like silicon nanoparticles react with excessive carbon and yield a highly crystalline ceramic composite. Two methods are proposed for the research, which is categorized by dependence on whether the polymers in the as-printed greenbodies are necessary for the final composite ceramics. If the polymers in the greenbodies are not desired, they are first debinded in the air for full and partial removal. Then, the porous samples are backfilled with PDCs after multiple PIP cycles to give ultimate strength (flexural strength up to  $74.3 \pm 13.7$  MPa, toughness up to  $4.0 \pm 0.9$  MPa·m<sup>1/2</sup> and lattice compressive strength up to  $32.8 \pm 11.2$  MPa). If the polymers in the greenbodies are desired, passive filler silicon nanoparticles are incorporated into the resins for reaction bond with excessive graphitic carbon in the samples. As a result, highly-crystalline ( $80.7 \pm 0.6$  %) SiC-Composite ceramics with large 3C-SiC crystallites ( $4.47 \pm 1.92$  µm) with the highest performance (flexural strength:  $89.6 \pm 32.3$  MPa; Weibull modulus:  $m_{\rm M} = 2.716$ ) are obtained.

The second part of the dissertation focused on the characterization of composite ceramics and the *in-situ* Raman study of polymer-to-ceramics transition. The structures of ceramics resulting from different fabrication methods are elaborated, the kinetics of ceramics formation are illustrated, and the structural/compositional evolution during the polymer-to-ceramics transition is detailed in the research. Multiple characterization methods are employed for characterizing the Composite ceramics, polymer-to-ceramic transition process, and reaction kinetics. FTIR, Raman, SEM, XPS, XRD, mechanical testing, thermal analysis, and microscopy were employed for materials characterization, where Chapter 3 and Chapter 4 reported a SiC-based ceramics composed of SiC fillers and SiOC/SiCN matrix while Chapter 4 focused on the adoption of a Si-O-C<sub>x</sub> scaffold for supporting the debinded greenbodies; Chapter 5 elaborated on

SLA of a highly crystalline SiC-Composite ceramics with large crystallites and crystallinity, the matrix binding the SiC particles are composed of Si/SiOC; Chapter 6 dived into *in-situ* Raman characterization of the entire polymer-to-ceramics transformation process and implemented *ex-situ* data for reaction kinetics; Chapter 7 combines the techniques of thermal modeling and thermal engineering together for optimizing the printed parts and resolutions.

This dissertation expanded from the basics of PDCs, their structure-properties relationship, and the entire thermal SLA development life cycle for highly loaded ceramic resins. The research pointed out a new and clear pathway for SLA of high-performance SiC-based ceramic materials and the potential industrial adoption of this technique.

## **BIBLIOGRAPHY**

- (1) *Ceramic history*. https://depts.washington.edu/matseed/mse\_resources/Webpage/Ceramics/ceramichistory.h tm (accessed 2025-03-19).
- (2) He, Z.; Chen, P.; Xuan, W.; Shao, G.; Song, H.; Wang, B.; Yang, Z.; Ren, Z. High Temperature Performance of Silica-Based Ceramic Cores by Adding (Mg0.25Co0.25Ni0.25Zn0.25)O Medium-Entropy Oxide as Mineralizer. *Ceram Int* 2025. https://doi.org/10.1016/J.CERAMINT.2025.01.454.
- (3) Dadkhah, M.; Tulliani, J. M.; Saboori, A.; Iuliano, L. Additive Manufacturing of Ceramics: Advances, Challenges, and Outlook. *J Eur Ceram Soc* 2023, *43* (15), 6635–6664. https://doi.org/10.1016/J.JEURCERAMSOC.2023.07.033.
- (4) Pirkelmann, S.; Raether, F.; Seifert, G. Top-down Material Design of Multi-Phase Ceramics. *Open Ceramics* 2022, *9*, 100211. https://doi.org/10.1016/J.OCERAM.2021.100211.
- (5) Xu, M.; Girish, Y. R.; Rakesh, K. P.; Wu, P.; Manukumar, H. M.; Byrappa, S. M.; Udayabhanu; Byrappa, K. Recent Advances and Challenges in Silicon Carbide (SiC) Ceramic Nanoarchitectures and Their Applications. *Mater Today Commun* 2021, 28, 102533. https://doi.org/10.1016/J.MTCOMM.2021.102533.
- (6) Liu, B.; Sun, J.; Guo, L.; Shi, H.; Feng, G.; Feldmann, L.; Yin, X.; Riedel, R.; Fu, Q.; Li, H. Materials Design of Silicon Based Ceramic Coatings for High Temperature Oxidation Protection. *Materials Science and Engineering: R: Reports* 2025, *163*, 100936. https://doi.org/10.1016/J.MSER.2025.100936.
- (7) Medvedovski, E. Advanced Ceramics and Coatings for Wear and Corrosion Related Applications in Modern High-Efficient Coal Production and Processing: A Technical Review. *Ceram Int* 2024, 50 (11), 19447–19487. https://doi.org/10.1016/J.CERAMINT.2024.03.187.
- (8) Roy, S. Recent Developments in Processing Techniques and Morphologies of Bulk Macroporous Ceramics for Multifunctional Applications. *Mater Today Commun* 2024, *38*, 107752. https://doi.org/10.1016/J.MTCOMM.2023.107752.
- (9) Ran, Y.; Sun, J.; Kang, R.; Dong, Z.; Bao, Y. Towards Understanding the Machining Process in Grinding of Ceramic Matrix Composites: A Review. *Compos B Eng* 2024, 284, 111657. https://doi.org/10.1016/J.COMPOSITESB.2024.111657.
- (10) Xu, Q.; Xiao, S.; Wang, Y.; Gao, H. A Review on the Grinding of SiC-Based Ceramic Matrix Composites Reinforced by Continuous Fibre: Damage Mechanisms and Evaluations. *J Manuf Process* 2024, *132* (November), 261–295. https://doi.org/10.1016/J.JMAPRO.2024.10.067.

- (11) Zhang, F.; Zhou, S.; You, H.; Zhang, G.; Yang, J.; Shi, Y. 3D Printing of Ceramic Matrix Composites: Strengthening and Toughening Strategies. *Compos B Eng* 2025, 297, 112335. https://doi.org/10.1016/J.COMPOSITESB.2025.112335.
- (12) Essmeister, J.; Altun, A. A.; Staudacher, M.; Lube, T.; Schwentenwein, M.; Konegger, T. Stereolithography-Based Additive Manufacturing of Polymer-Derived SiOC/SiC Ceramic Composites. *J Eur Ceram Soc* 2022, *42* (13), 5343–5354. https://doi.org/10.1016/J.JEURCERAMSOC.2022.06.021.
- (13) Huang, M.; Wu, Y.; Ou, J.; Huang, Y.; Wang, J.; Wu, S. 3D-Printing of Polymer-derived SiCN Ceramic Matrix Composites by Digital Light Processing. *J Eur Ceram Soc* 2022, 42 (13), 5476–5483. https://doi.org/10.1016/J.JEURCERAMSOC.2022.06.056.
- (14) Zhu, N.; Hou, Y.; Zhang, L.; Wen, G. Preparation of H-BN/SiCO Ceramic Matrix Composites with High Thermal Conductivity and Strength by Vat Photopolymerization 3D Printing. *J Eur Ceram Soc* 2024, 44 (10), 5885–5895. https://doi.org/10.1016/J.JEURCERAMSOC.2024.03.007.
- (15) Lv, X.; Ye, F.; Cheng, L.; Fan, S.; Liu, Y. Fabrication of SiC Whisker-Reinforced SiC Ceramic Matrix Composites Based on 3D Printing and Chemical Vapor Infiltration Technology. *J Eur Ceram Soc* 2019, *39* (11), 3380–3386. https://doi.org/10.1016/J.JEURCERAMSOC.2019.04.043.
- (16) Li, C.; Shen, W.; Wang, S.; Kang, J.; Zhang, Y.; Wang, G. Design and 3D Printing of Glass-Ceramic/Zirconia Composite ceramics for Dental Application. *Ceram Int* 2024, *50* (21), 42593–42606. https://doi.org/10.1016/J.CERAMINT.2024.08.103.
- (17) Liu, S.; Mo, L.; Bi, G.; Chen, S.; Yan, D.; Yang, J.; Jia, Y. G.; Ren, L. DLP 3D Printing Porous β-Tricalcium Phosphate Scaffold by the Use of Acrylate/Ceramic Composite Slurry. *Ceram Int* 2021, *47* (15), 21108–21116. https://doi.org/10.1016/J.CERAMINT.2021.04.114.
- (18) Esteves, A. V. M.; Martins, M. I.; Soares, P.; Rodrigues, M. A.; Lopes, M. A.; Santos, J. D. Additive Manufacturing of Ceramic Alumina/Calcium Phosphate Structures by DLP 3D Printing. *Mater Chem Phys* 2022, 276, 125417. https://doi.org/10.1016/J.MATCHEMPHYS.2021.125417.
- (19) Li, W. K.; Wu, J. M.; Zhou, F. L.; Deng, Z. Y.; Zhang, R. Z.; Lin, X.; Xu, H. S.; Wang, F.; Shi, Y. S. Influence of Sintering Temperature and Holding Time on the Properties of DLP-Fabricated Si3N4/SiAlON Ceramics. *Ceram Int* 2025, *51* (3), 3198–3208. https://doi.org/10.1016/J.CERAMINT.2024.11.295.
- (20) Sun, J.; Ye, D.; Zou, J.; Chen, X.; Wang, Y.; Yuan, J.; Liang, H.; Qu, H.; Binner, J.; Bai, J. A Review on Additive Manufacturing of Ceramic Matrix Composites. *J Mater Sci Technol* 2023, *138*, 1–16. https://doi.org/10.1016/J.JMST.2022.06.039.

- (21) Colombo, P.; Mera, G.; Riedel, R.; Sorarù, G. D. Polymer-Derived Ceramics: 40 Years of Research and Innovation in Advanced Ceramics. *Journal of the American Ceramic Society* 2010, 93 (7), no-no. https://doi.org/10.1111/j.1551-2916.2010.03876.x.
- (22) Young, J. C.; Brinckmann, S. A.; Fertig, R. S.; Lynch, S. P.; Frick, C. P. Influence of Layer Thickness and Exposure on Mechanical Properties of Additively Manufactured Polymer-Derived SiOC Ceramics. *Open Ceramics* 2024, *19*, 100652. https://doi.org/10.1016/J.OCERAM.2024.100652.
- Young, J. C.; Brinckmann, S. A.; Fox, A.; Fertig, R. S.; Lynch, S. P.; Frick, C. P. On Enhancing the Manufacturability and Conversion of Additively Manufactured Polymer-Derived Ceramics. *J Eur Ceram Soc* 2024, *44* (14), 116691. https://doi.org/10.1016/J.JEURCERAMSOC.2024.116691.
- (24) Franchin, G.; Elsayed, H.; Botti, R.; Huang, K.; Schmidt, J.; Giometti, G.; Zanini, A.; De Marzi, A.; D'Agostini, M.; Scanferla, P.; Feng, Y.; Colombo, P. Additive Manufacturing of Ceramics from Liquid Feedstocks. *Chinese Journal of Mechanical Engineering:*\*\*Additive Manufacturing Frontiers 2022, 1 (1), 100012.

  https://doi.org/10.1016/J.CJMEAM.2022.100012.
- (25) Shwailiya, S. A.; Hameed, M. R. Multi-Material Functionally Graded Additive Manufacturing of Zirconia Ceramic: A Systematic Review. *Open Ceramics* 2025, *21*, 100741. https://doi.org/10.1016/J.OCERAM.2025.100741.
- (26) Arshad, Q.; Saqib, M.; Arshad, M. A.; Raza, M.; Hussain, M. I.; Asghar, A.; Luo, X.; Chen, Z. Progress in Vat Photopolymerisation Additive Manufacturing of Ceramic Lattice Structures and Applications. *Thin-Walled Structures* 2025, 209, 112918. https://doi.org/10.1016/J.TWS.2025.112918.
- (27) Brinckmann, S. A.; Yao, J.; Young, J. C.; Jones, M. H.; Fertig, R. S.; Frick, C. P. Additive Manufacturing of SiCNO Polymer-Derived Ceramics via Step-Growth Polymerization. *Open Ceramics* 2023, *15*, 100414. https://doi.org/10.1016/J.OCERAM.2023.100414.
- (28) Yang, M.; Li, J.; Zhang, J.; Cao, J.; Luo, P.; Liu, J.; Gao, G.; Dong, J.; Jiang, Z. DLP-Printed SiBOC Ceramic Components from Preceramic Polymers Based on Boric Acid. *J Eur Ceram Soc* 2024, 44 (15), 116747. https://doi.org/10.1016/J.JEURCERAMSOC.2024.116747.
- (29) Sarraf, F.; Hadian, A.; Gfeller, F.; Churakov, S. V.; Clemens, F. Crosslinking and Pyrolysis of a Methyl-Silsesquioxane: Effect of Heating Rate on Fabrication of Polymer Derived Mullite Ceramics Using Thermoplastic Shaping. *Mater Des* 2024, 237, 112578. https://doi.org/10.1016/J.MATDES.2023.112578.
- (30) Hussain, M. I.; Xia, M.; Ren, X. N.; Shen, Z.; Jamil, M.; Ge, C. Recent Advances in Photopolymerization 3D Printing of Alumina-Ceramic. *Progress in Natural Science: Materials International* 2025, *35* (1), 1–30. https://doi.org/10.1016/J.PNSC.2024.07.013.

- (31) Wang, Y.; Bu, Y.; Wang, X. Advances in 3D Printing of Structural and Functional Ceramics: Technologies, Properties, and Applications. *J Eur Ceram Soc* 2024, *44* (14), 116653. https://doi.org/10.1016/J.JEURCERAMSOC.2024.05.075.
- (32) Wang, Y.; Wu, T.; Huang, G. State-of-the-Art Research Progress and Challenge of the Printing Techniques, Potential Applications for Advanced Ceramic Materials 3D Printing. *Mater Today Commun* 2024, *40*, 110001. https://doi.org/10.1016/J.MTCOMM.2024.110001.
- (33) Hagelüken, L.; Sasikumar, P. V. W.; Lee, H. Y.; Di Stadio, D.; Chandorkar, Y.; Rottmar, M.; Maniura-Weber, K.; Blugan, G.; Brugger, J. Multiscale 2D/3D Microshaping and Property Tuning of Polymer-Derived SiCN Ceramics. *J Eur Ceram Soc* 2022, *42* (5), 1963–1970. https://doi.org/10.1016/J.JEURCERAMSOC.2021.12.044.
- (34) Yang, J.; Yu, R.; Li, X.; He, Y.; Wang, L.; Huang, W.; Jiao, J. Silicon Carbide Whiskers Reinforced SiOC Ceramics through Digital Light Processing 3D Printing Technology. *Ceram Int* 2021, 47 (13), 18314–18322. https://doi.org/10.1016/J.CERAMINT.2021.03.152.
- (35) Zhang, K.; Meng, Q.; Qu, Z.; He, R. A Review of Defects in Vat Photopolymerization Additive-Manufactured Ceramics: Characterization, Control, and Challenges. *J Eur Ceram Soc* 2024, *44* (3), 1361–1384. https://doi.org/10.1016/J.JEURCERAMSOC.2023.10.067.
- (36) Guo, H.; Seetoh, I.; Ye, P.; Zhao, Y.; Lai, C.; Du, Z.; Gan, C. L. Mechanical Properties and Failure Behavior of Silicon Nitride Based Plate and Truss Lattices Fabricated by Vat Photopolymerization 3D Printing. *Materials Science and Engineering: A* 2025, 927, 148030. https://doi.org/10.1016/J.MSEA.2025.148030.
- (37) Saqib, M.; Ren, W.; Arshad, Q.; Asghar, A.; Raza, M.; Hamza, M.; Chen, Z. Systematic Optimization of Silicon Nitride Slurries for High-Precision Photopolymerization 3D Printing. *Ceram Int* 2025. https://doi.org/10.1016/J.CERAMINT.2025.03.178.
- (38) Ren, D.; Xu, W.; Gao, Y.; Wang, Y. UV Curing Behavior of a Liquid Polyborosilazane and Stereolithography to SiBCN Ceramic Components. *Ceram Int* 2023, *49* (7), 11571–11578. https://doi.org/10.1016/J.CERAMINT.2022.12.004.
- (39) Pelanconi, M.; Bottacin, S.; Colombo, P.; Ortona, A. Powder Bed Fusion of Polyamide Powders Combined with Different Preceramic Polymers Infiltration and Pyrolysis to Produce Complex-Shaped Ceramics. *J Eur Ceram Soc* 2023, *43* (14), 5871–5881. https://doi.org/10.1016/J.JEURCERAMSOC.2023.06.053.
- (40) Zhou, S.; Mei, H.; Chang, P.; Lu, M.; Cheng, L. Molecule Editable 3D Printed Polymer-Derived Ceramics. *Coord Chem Rev* 2020, 422, 213486. https://doi.org/10.1016/J.CCR.2020.213486.

- (41) Ackley, B. J.; Martin, K. L.; Key, T. S.; Clarkson, C. M.; Bowen, J. J.; Posey, N. D.; Ponder, J. F.; Apostolov, Z. D.; Cinibulk, M. K.; Pruyn, T. L.; Dickerson, M. B. Advances in the Synthesis of Preceramic Polymers for the Formation of Silicon-Based and Ultrahigh-Temperature Non-Oxide Ceramics. *Chem Rev* 2023, 123 (8), 4188–4236. https://doi.org/10.1021/ACS.CHEMREV.2C00381/ASSET/IMAGES/MEDIUM/CR2C00 381\_0047.GIF.
- (42) Wang, J.; Zhang, Q.; Li, S.; Zhao, J.; Wei, J.; Gao, Y.; Jian, Z.; Lu, Z. Recent Advances in Preceramic Polysilazane Precursors in Additive Manufacturing. *Additive Manufacturing Frontiers* 2024, *3* (1), 200119. https://doi.org/10.1016/J.AMF.2024.200119.
- (43) Kim, S.; Biju, C.; Karunarathna, M. S.; Grimes, N. Y.; Hmeidat, N. S.; Reyes-Zacarias, J.; Agarwal, S.; Anisur Rahman, M.; Gilmer, D. B.; Compton, B. G.; Bullock, S. E.; Saito, T.; Cramer, C. L. Tuning Crosslinking of Hybrid Preceramic Polymers in Vat Photopolymerization toward Controlled Ceramic Yields. *Chemical Engineering Journal* 2024, 499, 156585. https://doi.org/10.1016/J.CEJ.2024.156585.
- (44) Fu, S.; Zhu, M.; Zhu, Y. Organosilicon Polymer-Derived Ceramics: An Overview. *Journal of Advanced Ceramics* 2019, 8 (4). https://doi.org/10.1007/s40145-019-0335-3.
- (45) Shi, Z.; Xue, J.; Zhang, H.; Yang, Z.; Huang, J.; Yu, J.; Zhu, Y. 3D Printing of Polymer-Derived Ceramic Scaffolds with Cuttlebone-like Structure for Bone Repair. *Ceram Int* 2025, *51* (8), 9677–9685. https://doi.org/10.1016/J.CERAMINT.2024.12.398.
- (46) Wu, H.; Zhang, W.; Zhang, J. Pyrolysis Synthesis and Microstructure of Zirconium Carbide from New Preceramic Polymers. *Ceram Int* 2014, *40* (4), 5967–5972. https://doi.org/10.1016/J.CERAMINT.2013.11.044.
- (47) Key, T. S.; Patel, D. K.; Wilks, G. B.; Cinibulk, M. K. Modeling the Pyrolysis of Preceramic Polymers: A Kinetic Study of the Polycarbosilane SMP-10. *J Eur Ceram Soc* 2021, *41* (13), 6356–6365. https://doi.org/10.1016/J.JEURCERAMSOC.2021.06.011.
- (48) Chung, Y.; Yoshida, K. Effect of Sintering Atmosphere on the Electrical Properties of Aluminum and Boron-Added Porous Silicon Carbide Ceramics. *Ceram Int* 2025, *51* (5), 6740–6747. https://doi.org/10.1016/J.CERAMINT.2024.12.118.
- (49) Hu, G.; Han, Y.; Wang, Y.; Li, D.; Xing, H.; Zhang, J.; Sun, B. Amorphous Silica Particles Reinforced Nickel Matrix Composites Fabricated by In-Situ Pyrolysis of Polycarbosilane. *J Alloys Compd* 2023, *960*, 170968. https://doi.org/10.1016/J.JALLCOM.2023.170968.
- (50) Eckel, Z. C.; Zhou, C.; Martin, J. H.; Jacobsen, A. J.; Carter, W. B.; Schaedler, T. A. Additive Manufacturing of Polymer-Derived Ceramics. *Science* (1979) 2016, 351 (6268), 58–62. https://doi.org/10.1126/science.aad2688.

- (51) Bauer, A.; Christ, M.; Zimmermann, A.; Aldinger, F. Fracture Toughness of Amorphous Precursor-Derived Ceramics in the Silicon-Carbon-Nitrogen System. *Journal of the American Ceramic Society* 2001, *84* (10), 2203–2207. https://doi.org/10.1111/J.1151-2916.2001.TB00988.X.
- (52) Wang, Y.; Li, H.; Zhang, L.; Cheng, L. Oxidation Behavior of Polymer Derived SiCO Powders. Ceram Int 2009, 35 (3), 1129–1132. https://doi.org/10.1016/J.CERAMINT.2008.05.006.
- (53) Anand, R.; Sahoo, S. P.; Nayak, B. B.; Behera, S. K. Phase Evolution, Nanostructure, and Oxidation Resistance of Polymer Derived SiTiOC Ceramic Hybrid. *Ceram Int* 2019, *45* (5), 6570–6576. https://doi.org/10.1016/J.CERAMINT.2018.12.024.
- (54) Sarraf, F.; Churakov, S. V.; Clemens, F. Preceramic Polymers for Additive Manufacturing of Silicate Ceramics. *Polymers (Basel)* 2023, *15* (22), 4360. https://doi.org/10.3390/POLYM15224360.
- (55) Bura, R.; C, V. G.; Prasad, R. M. Enhanced Corrosion Protection Performance Using Polysilazane-Derived Amorphous SiCN Ceramic Coating. *Surf Coat Technol* 2024, 494 (September). https://doi.org/10.1016/j.surfcoat.2024.131402.
- (56) He, J.; Song, M.; Chen, K.; Kan, D.; Zhu, M. Polymer-Derived Ceramics Technology: Characteristics, Procedure, Product Structures, and Properties, and Development of the Technology in High-Entropy Ceramics. *Crystals 2022, Vol. 12, Page 1292* 2022, *12* (9), 1292. https://doi.org/10.3390/CRYST12091292.
- (57) Thakur, T.; Carretta, M.; Komissarenko, D.; Blugan, G. Advancements in DLP 3D Printing: High Strength Alumina Toughened Zirconia Ceramics for Biomedical Applications. *Open Ceramics* 2024, *18*, 100601. https://doi.org/10.1016/J.OCERAM.2024.100601.
- (58) Liu, J.; Yang, R. Tuning the Thermal Conductivity of Polymers with Mechanical Strains. *Physical Review B Condensed Matter and Materials Physics*. 2010. https://doi.org/10.1103/PhysRevB.81.174122.
- (59) Wen, Q.; Yu, Z.; Riedel, R. The Fate and Role of in Situ Formed Carbon in Polymer-Derived Ceramics. *Prog Mater Sci* 2020, *109*, 100623. https://doi.org/10.1016/J.PMATSCI.2019.100623.
- (60) Chaudhary, R. P.; Parameswaran, C.; Idrees, M.; Rasaki, A. S.; Liu, C.; Chen, Z.; Colombo, P. Additive Manufacturing of Polymer-Derived Ceramics: Materials, Technologies, Properties and Potential Applications. *Prog Mater Sci* 2022, *128*, 100969. https://doi.org/10.1016/j.pmatsci.2022.100969.
- (61) Xiong, S.; Liu, J.; Cao, J.; Li, Z.; Idrees, M.; Lin, X.; Long, Z.; Liu, Z.; Wang, P.; Liu, C.; Chen, Z. 3D Printing of Crack-Free Dense Polymer-Derived Ceramic Monoliths and

- Lattice Skeletons with Improved Thickness and Mechanical Performance. *Addit Manuf* 2022, *57*, 102964. https://doi.org/10.1016/J.ADDMA.2022.102964.
- (62) Prasad, R. M.; Mera, G.; Morita, K.; Müller, M.; Kleebe, H. J.; Gurlo, A.; Fasel, C.; Riedel, R. Thermal Decomposition of Carbon-Rich Polymer-Derived Silicon Carbonitrides Leading to Ceramics with High Specific Surface Area and Tunable Microand Mesoporosity. *J Eur Ceram Soc* 2012, 32 (2), 477–484. https://doi.org/10.1016/J.JEURCERAMSOC.2011.08.020.
- (63) Zambotti, A.; Kulkarni, A.; Semerci, T.; Vakifahmetoglu, C.; Pelanconi, M.; Bottacin, S.; Balzarotti, R.; Ortona, A.; Sorarù, G. D. Macroporous Polymer-Derived Ceramics Produced by Standard and Additive Manufacturing Methods: How the Shaping Technique Can Affect Their High Temperature Thermal Behavior. *Open Ceramics* 2024, *18*, 100603. https://doi.org/10.1016/J.OCERAM.2024.100603.
- (64) Bernard, S.; Fiaty, K.; Cornu, D.; Miele, P.; Laurent, P. Kinetic Modeling of the Polymer-Derived Ceramics Route: Investigation of the Thermal Decomposition Kinetics of Poly[B-(Methylamino)Borazine] Precursors into Boron Nitride. 2006. https://doi.org/10.1021/jp055981m.
- (65) Jiang, L.; Long, C.; Xiong, S.; Wang, X.; Mo, Y.; Zeng, J.; Liu, Z.; Liu, C.; Chen, Z. 4D Printing of Shape-Programmable Polymer-Derived Ceramics via Two-Stage Folding-Assisted Pyrolysis Strategy. *Virtual Phys Prototyp* 2024, 19 (1). https://doi.org/10.1080/17452759.2024.2406408.
- (66) Bura, R.; C, V. G.; Prasad, R. M. Enhanced Corrosion Protection Performance Using Polysilazane-Derived Amorphous SiCN Ceramic Coating. *Surf Coat Technol* 2024, 494, 131402. https://doi.org/10.1016/J.SURFCOAT.2024.131402.
- (67) Tang, H.; Wang, K.; Ren, K.; Wang, Y. Microstructural Evolution and Microwave Transmission/Absorption Transition in Polymer-Derived SiOC Ceramics. *Ceram Int* 2023, 49 (12), 20406–20418. https://doi.org/10.1016/J.CERAMINT.2023.03.169.
- (68) Schmalz, T.; Kraus, T.; Günthner, M.; Liebscher, C.; Glatzel, U.; Kempe, R.; Motz, G. Catalytic Formation of Carbon Phases in Metal Modified, Porous Polymer Derived SiCN Ceramics. *Carbon N Y* 2011, *49* (9), 3065–3072. https://doi.org/10.1016/J.CARBON.2011.03.027.
- (69) Poerschke, D. L.; Braithwaite, A.; Park, D.; Lauten, F. Crystallization Behavior of Polymer-Derived Si-O-C for Ceramic Matrix Composite Processing. *Acta Mater* 2018, 147, 329–341. https://doi.org/10.1016/J.ACTAMAT.2018.01.052.
- (70) Kurtenbach, D.; Martin, H. P.; Müller, E.; Roewer, G.; Hoell, A. Crystallization of Polymer Derived Silicon Carbide Materials. *J Eur Ceram Soc* 1998, *18* (13), 1885–1891. https://doi.org/10.1016/S0955-2219(98)00136-8.

- (71) Li, W.; Ji, X.; Gai, K.; Yang, Y.; Wang, Q.; Zhao, T. Regulating Crystalline Behavior to Create Fully Crystallized α-Al2O3-Mullite Continuous Ceramic Fibers Derived from the Melt-Spinning of Polymer Precursor. *Ceram Int* 2025, *51* (6), 7897–7905. https://doi.org/10.1016/J.CERAMINT.2024.12.226.
- (72) Fu, Y.; Xu, L.; Zhao, F.; Shao, C.; Li, Y.; Li, L.; Chen, S.; Chen, Q.; Wang, L.; Sun, D.; Wu, C. Ultrafast High-Temperature Sintering of Polymer-Derived Ceramic Thick Film Sensors. *Ceram Int* 2024, 50 (19), 36908–36918. https://doi.org/10.1016/J.CERAMINT.2024.07.078.
- (73) He, J.; Song, M.; Chen, K.; Kan, D.; Zhu, M. Polymer-Derived Ceramics Technology: Characteristics, Procedure, Product Structures, and Properties, and Development of the Technology in High-Entropy Ceramics. *Crystals* 2022, *Vol.* 12, *Page* 1292 2022, *12* (9), 1292. https://doi.org/10.3390/CRYST12091292.
- (74) Zhu, L. L.; Dai, M. M.; Xu, X.; Zhao, C. C.; Zhang, G. X.; Jian, Y. J.; Guo, W. M.; Lin, H. T. Alumina Ceramics Joined with Screen-Printed B2O3 by Spark Plasma Sintering. *Ceram Int* 2021, 47 (21), 30838–30843. https://doi.org/10.1016/J.CERAMINT.2021.07.264.
- (75) Atkinson, H. V.; Davies, S. Fundamental Aspects of Hot Isostatic Pressing: An Overview. *Metall Mater Trans A Phys Metall Mater Sci* 2000, *31* (12), 2981–3000. https://doi.org/10.1007/S11661-000-0078-2/METRICS.
- (76) Makurunje, P.; Middleburgh, S. C.; Lee, W. E. Addressing High Processing Temperatures in Reactive Melt Infiltration for Multiphase Ceramic Composites. *J Eur Ceram Soc* 2023, 43 (2), 183–197. https://doi.org/10.1016/J.JEURCERAMSOC.2022.09.002.
- (77) Lange, F. F.; Tu, W. C.; Evans, A. G. Processing of Damage-Tolerant, Oxidation-Resistant Ceramic Matrix Composites by a Precursor Infiltration and Pyrolysis Method. *Materials Science and Engineering: A* 1995, *195* (C), 145–150. https://doi.org/10.1016/0921-5093(94)06513-6.
- (78) Tang, J.; Liu, M.; Wei, Y.; Yang, Y.; Huang, Z. An Efficient and Low-Cost Liquid Silicon Infiltration Method to Prepare SiC-Coated Carbon Short Fiber for Fiber Protection of Cf/SiC Ceramic Matrix Composites. *Ceram Int* 2021, 47 (9), 13235–13241. https://doi.org/10.1016/J.CERAMINT.2021.01.115.
- (79) Delhaes, P. Chemical Vapor Deposition and Infiltration Processes of Carbon Materials. *Carbon N Y* 2002, *40* (5), 641–657. https://doi.org/10.1016/S0008-6223(01)00195-6.
- (80) Miele, P.; Bernard, S.; Cornu, D.; Toury, B. Recent Developments in Polymer-Derived Ceramic Fibers (PDCFs): Preparation, Properties and Applications A Review. *Soft Mater* 2007, *4* (2–4), 249–286. https://doi.org/10.1080/15394450701310228.

- (81) Ichikawa, H. Polymer-Derived Ceramic Fibers. 2016. https://doi.org/10.1146/annurev-matsci-070115-032127.
- (82) Khecho, A.; Rahman, M. M. T.; Reddy, D.; El-Ghannam, A.; Joyee, E. B. DLP-Based Additive Manufacturing of Hollow 3D Structures with Surface Activated Silicone Carbide-Polymer Composite. *Compos B Eng* 2025, *296*, 112236. https://doi.org/10.1016/J.COMPOSITESB.2025.112236.
- (83) Bauer, J.; Hengsbach, S.; Tesari, I.; Schwaiger, R.; Kraft, O. High-Strength Cellular Ceramic Composites with 3D Microarchitecture. *Proceedings of the National Academy of Sciences* 2014, *111* (7), 2453–2458. https://doi.org/10.1073/pnas.1315147111.
- (84) Ou, J.; Huang, M.; Wu, Y.; Huang, S.; Lu, J.; Wu, S. Additive Manufacturing of Flexible Polymer-Derived Ceramic Matrix Composites. *Virtual Phys Prototyp* 2023, *18* (1). https://doi.org/10.1080/17452759.2022.2150230.
- (85) Liu, K.; Qiu, L.; Zhang, Y.; Du, Y.; Sun, C.; Zhang, S.; Tu, R.; Wu, Y.; Sun, H.; Shi, Y. Additive Manufacturing of Continuous Carbon Fibers Reinforced Silicon Carbide Ceramic Composites. *Int J Appl Ceram Technol* 2023. https://doi.org/10.1111/ijac.14488.
- (86) Essmeister, J.; Altun, A. A.; Staudacher, M.; Lube, T.; Schwentenwein, M.; Konegger, T. Stereolithography-Based Additive Manufacturing of Polymer-Derived SiOC/SiC Ceramic Composites. *J Eur Ceram Soc* 2022, *42* (13), 5343–5354. https://doi.org/10.1016/j.jeurceramsoc.2022.06.021.
- (87) Shahzad, A.; Lazoglu, I. Direct Ink Writing (DIW) of Structural and Functional Ceramics: Recent Achievements and Future Challenges. *Compos B Eng* 2021, 225, 109249. https://doi.org/10.1016/J.COMPOSITESB.2021.109249.
- (88) Zhao, Y.; Zhu, J.; He, W.; Liu, Y.; Sang, X.; Liu, R. 3D Printing of Unsupported Multi-Scale and Large-Span Ceramic via near-Infrared Assisted Direct Ink Writing. *Nat Commun* 2023, *14* (1), 2381. https://doi.org/10.1038/s41467-023-38082-8.
- (89) Bai, X.; Ding, G.; Zhang, K.; Wang, W.; Zhou, N.; Fang, D.; He, R. Stereolithography Additive Manufacturing and Sintering Approaches of SiC Ceramics. *Open Ceramics* 2021, 5, 100046. https://doi.org/10.1016/j.oceram.2020.100046.
- (90) Essmeister, J.; Altun, A. A.; Staudacher, M.; Lube, T.; Schwentenwein, M.; Konegger, T. Stereolithography-Based Additive Manufacturing of Polymer-Derived SiOC/SiC Ceramic Composites. *J Eur Ceram Soc* 2022, *42* (13), 5343–5354. https://doi.org/10.1016/j.jeurceramsoc.2022.06.021.
- (91) Mahmood, A.; Akram, T.; Chen, H.; Chen, S. On the Evolution of Additive Manufacturing (3D/4D Printing) Technologies: Materials, Applications, and Challenges. *Polymers (Basel)* 2022, *14* (21), 4698. https://doi.org/10.3390/polym14214698.

- (92) Lacelle, T.; Sampson, K. L.; Sarvestani, H. Y.; Rahimizadeh, A.; Robles, J. B.; Mirkhalaf, M.; Rafiee, M.; Jakubinek, M. B.; Paquet, C.; Ashrafi, B. Additive Manufacturing of Polymer Derived Ceramics: Materials, Methods, and Applications. *APL Mater* 2023, *11* (7), 70602. https://doi.org/10.1063/5.0151661/2901841.
- (93) Cramer, C. L.; Yoon, B.; Lance, M. J.; Cakmak, E.; Campbell, Q. A.; Mitchell, D. J. Additive Manufacturing of C/C-SiC Ceramic Matrix Composites by Automated Fiber Placement of Continuous Fiber Tow in Polymer with Pyrolysis and Reactive Silicon Melt Infiltration. *Journal of Composites Science* 2022, *6* (12). https://doi.org/10.3390/jcs6120359.
- (94) Additive Manufacturing of Ceramics from Preceramic Polymers: A Versatile Stereolithographic Approach Assisted by Thiol-Ene Click Chemistry.
- (95) Wang, X.; Schmidt, F.; Hanaor, D.; Kamm, P. H.; Li, S.; Gurlo, A. Additive Manufacturing of Ceramics from Preceramic Polymers: A Versatile Stereolithographic Approach Assisted by Thiol-Ene Click Chemistry. *Addit Manuf* 2019, 27, 80–90. https://doi.org/10.1016/j.addma.2019.02.012.
- (96) Tucker-Schwartz, A. K.; Farrell, R. A.; Garrell, R. L. Thiol Ene Click Reaction as a General Route to Functional Trialkoxysilanes for Surface Coating Applications. *J Am Chem Soc* 2011, *133* (29), 11026–11029. https://doi.org/10.1021/ja202292q.
- (97) Eckel, Z. C.; Zhou, C.; Martin, J. H.; Jacobsen, A. J.; Carter, W. B.; Schaedler, T. A. Additive Manufacturing of Polymer-Derived Ceramics. *Science* (1979) 2016, 351 (6268), 58–62. https://doi.org/10.1126/science.aad2688.
- (98) Kuo, C. F. J.; Dewangga, G. R. S.; Chen, J. B. Fabrication of a Thermally Conductive Silicone Composite by Incorporating Surface-Modified Boron Nitride. *Textile Research Journal* 2019, 89 (13), 2637–2647. https://doi.org/10.1177/0040517518798654.
- (99) Abass, M. A.; Syed, A. A.; Gervais, C.; Singh, G. Synthesis and Electrochemical Performance of a Polymer-Derived Silicon Oxycarbide/Boron Nitride Nanotube Composite. *RSC Adv* 2017, 7 (35), 21576–21584. https://doi.org/10.1039/c7ra01545c.
- (100) Gervais, C. Solid-State NMR Applied to Si-Based Polymer Derived Ceramics: A Review. *Open Ceramics* 2023, *15*. https://doi.org/10.1016/j.oceram.2023.100376.
- (101) Qazzazie-Hauser, A.; Honnef, K.; Hanemann, T. Crosslinking Behavior of UV-Cured Polyorganosilazane as Polymer-Derived Ceramic Precursor in Ambient and Nitrogen Atmosphere. *Polymer (Guildf)* 2021, *13* (15), 2424. https://doi.org/10.3390/polym13152424.
- (102) Thain, S. IR Spectroscopy and FTIR Spectroscopy: How an FTIR Spectrometer Works and FTIR Analysis. *Technology Networks Analysis & Separations* 2022.

- (103) Jones, R. R.; Hooper, D. C.; Zhang, L.; Wolverson, D.; Valev, V. K. Raman Techniques: Fundamentals and Frontiers. *Nanoscale Research Letters*. 2019. https://doi.org/10.1186/s11671-019-3039-2.
- (104) Mandrile, L.; Giovannozzi, A. M.; Pennecchi, F.; Saverino, A.; Lobascio, C.; Rossi, A. M. Direct Detection and Quantification of Molecular Surface Contaminants by Infrared and Raman Spectroscopy. *Analytical Methods* 2015, 7 (6), 2813–2821. https://doi.org/10.1039/C4AY02850C.
- (105) Li, Z.; Chen, Z.; Liu, J.; Fu, Y.; Liu, C.; Wang, P.; Jiang, M.; Lao, C. Additive Manufacturing of Lightweight and High-Strength Polymer-Derived SiOC Ceramics. *Virtual Phys Prototyp* 2020, *15* (2), 163–177. https://doi.org/10.1080/17452759.2019.1710919.
- (106) Belova, V.; Jankowski, M.; Saedi, M.; Groot, I. M. N.; Renaud, G.; Konovalov, O. V. Employing Surface Curvature for Spatially Resolved X-Ray Reflectivity: Graphene Domains on Liquid Copper. *Adv Mater Interfaces* 2023, *10* (15). https://doi.org/10.1002/admi.202300053.
- (107) Meza, L. R.; Das, S.; Greer, J. R. Strong, Lightweight, and Recoverable Three-Dimensional Ceramic Nanolattices. *Science* (1979) 2014, 345 (6202), 1322–1326. https://doi.org/10.1126/science.1255908.
- (108) He, R.; Zhou, N.; Zhang, K.; Zhang, X.; Zhang, L.; Wang, W.; Fang, D. Progress and Challenges towards Additive Manufacturing of SiC Ceramic. *Journal of Advanced Ceramics* 2021, *10* (4), 637–674. https://doi.org/10.1007/s40145-021-0484-z.
- (109) Ding, G.; He, R.; Zhang, K.; Xia, M.; Feng, C.; Fang, D. Dispersion and Stability of SiC Ceramic Slurry for Stereolithography. *Ceram Int* 2020, *46* (4), 4720–4729. https://doi.org/10.1016/j.ceramint.2019.10.203.
- (110) Hagelüken, L.; Sasikumar, P. V. W.; Lee, H. Y.; Di Stadio, D.; Chandorkar, Y.; Rottmar, M.; Maniura-Weber, K.; Blugan, G.; Brugger, J. Multiscale 2D/3D Microshaping and Property Tuning of Polymer-Derived SiCN Ceramics. *J Eur Ceram Soc* 2022, *42* (5), 1963–1970. https://doi.org/10.1016/j.jeurceramsoc.2021.12.044.
- (111) Chen, X.; Yin, J.; Xia, A.; Liu, X.; Huang, Z. Laser Additive Manufacturing of SiC Ceramics. *Advanced Ceramics for Versatile Interdisciplinary Applications* 2022, 41–67. https://doi.org/10.1016/B978-0-323-89952-9.00014-2.
- (112) Kemp, J. W.; Hmeidat, N. S.; Compton, B. G. Boron Nitride-Reinforced Polysilazane-Derived Ceramic Composites via Direct-Ink Writing. *Journal of the American Ceramic Society* 2020, *103* (8), 4043–4050. https://doi.org/10.1111/jace.17084.

- (113) Gorjan, L.; Tonello, R.; Sebastian, T.; Colombo, P.; Clemens, F. Fused Deposition Modeling of Mullite Structures from a Preceramic Polymer and γ-Alumina. *J Eur Ceram Soc* 2019, *39* (7), 2463–2471. https://doi.org/10.1016/j.jeurceramsoc.2019.02.032.
- (114) Friedel, T.; Travitzky, N.; Niebling, F.; Scheffler, M.; Greil, P. Fabrication of Polymer Derived Ceramic Parts by Selective Laser Curing. *J Eur Ceram Soc* 2005, 25, 193–197. https://doi.org/10.1016/j.jeurceramsoc.2004.07.017.
- (115) Sieber, H.; Friedrich, H.; Zeschky, J.; Greil, P. Light Weight Ceramic Composites from Laminated Paper Structures. *24th Annual Conference on Composites, Advanced Ceramics, Materials, and Structures: B* 2008, 129–134. https://doi.org/10.1002/9780470294635.ch17.
- (116) Chen, Z.; Li, Z.; Li, J.; Liu, C.; Lao, C.; Fu, Y.; Liu, C.; Li, Y.; Wang, P.; He, Y. 3D Printing of Ceramics: A Review. *J Eur Ceram Soc* 2019, *39* (4), 661–687. https://doi.org/10.1016/j.jeurceramsoc.2018.11.013.
- (117) Wei, L.; Li, J.; Zhang, S.; Li, B.; Liu, Y.; Wang, F.; Dong, S. Fabrication of SiOC Ceramic with Cellular Structure via UV-Assisted Direct Ink Writing. *Ceram Int* 2020, 46 (3), 3637–3643. https://doi.org/10.1016/j.ceramint.2019.10.083.
- (118) Huang, M.; Wu, Y.; Ou, J.; Huang, Y.; Wang, J.; Wu, S. 3D-Printing of Polymer-derived SiCN Ceramic Matrix Composites by Digital Light Processing. *J Eur Ceram Soc* 2022, 42 (13), 5476–5483. https://doi.org/10.1016/j.jeurceramsoc.2022.06.056.
- (119) Huiwen, Xiong, Lianzhong Zhao, et al. 3D SiC Containing Uniformly Dispersed, Aligned SiC Whiskers: Printability, Microstructure and Mechanical Properties. Journal of Alloys and Compounds 2019, p 151824. https://doi.org/https://doi.org/10.1016/j.jallcom.2019.151824.
- (120) Stevens, L. M.; Tagnon, C.; Page, Z. A. "invisible" Digital Light Processing 3D Printing with Near Infrared Light. *ACS Appl Mater Interfaces* 2022, *14* (20), 22912–22920. https://doi.org/10.1021/acsami.1c22046.
- (121) Zhu, J.; Zhang, Q.; Yang, T.; Liu, Y.; Liu, R. 3D Printing of Multi-Scalable Structures via High Penetration near-Infrared Photopolymerization. *Nat Commun* 2020, *11* (1), 1–7. https://doi.org/10.1038/s41467-020-17251-z.
- (122) El Chawich, G.; El Hayek, J.; Rouessac, V.; Cot, D.; Rebière, B.; Habchi, R.; Garay, H.; Bechelany, M.; Zakhour, M.; Miele, P.; Salameh, C. Design and Manufacturing of Si-Based Non-Oxide Cellular Ceramic Structures through Indirect 3D Printing. *Materials* 2022, *15* (2), 471. https://doi.org/10.3390/ma15020471.
- (123) Scarparo, M. A. F.; Kiel, A.; Zhiyao, Z.; Ferrari, C. A.; Chen, Q. J.; Miller, A. S.; Allen, S. D. Study of Resin Based Materials Using CO2 Laser Stereolithography. *Polymer* (*Guildf*) 1997, 38 (9), 2175–2181. https://doi.org/10.1016/S0032-3861(96)00763-X.

- (124) Fu, L. Laser Curing of Inks for Plastic Electronic Applications, University of Liverpool, 2014.
- (125) Joseph Fortenbaugh, R.; Lear, B. J. On-Demand Curing of Polydimethylsiloxane (PDMS) Using the Photothermal Effect of Gold Nanoparticles. *Nanoscale* 2017, *9* (25), 8555–8559. https://doi.org/10.1039/c7nr01423f.
- (126) Lear, Benjamin J, et al. Photothermal Curing of Thermoset Resins. US 20200056043A1, May 4, 2020.
- (127) Mathieu L. Viger, et al. Near-Infrared-Induced Heating of Confined Water in Polymeric Particles for Efficient Payload Release. *ACS Nano* 2014, 8 (5), 4815–4826. https://doi.org/10.1021/nn500702g.
- (128) Fortenbaugh, R. J.; Carrozzi, S. A.; Lear, B. J. Photothermal Control over the Mechanical and Physical Properties of Polydimethylsiloxane. *Macromolecules* 2019. https://doi.org/10.1021/acs.macromol.9b00134.
- (129) Hong, Z.; Liang, R. IR-Laser Assisted Additive Freeform Optics Manufacturing. *Scientific Reports*. 2017. https://doi.org/10.1038/s41598-017-07446-8.
- (130) Bauer, J.; Crook, C.; Guell Izard, A.; Eckel, Z. C.; Ruvalcaba, N.; Schaedler, T. A.; Valdevit, L. Additive Manufacturing of Ductile, Ultrastrong Polymer-Derived Nanoceramics. *Matter* 2019, *1* (6), 1547–1556. https://doi.org/10.1016/j.matt.2019.09.009.
- (131) Pan, Z.; Wang, D.; Guo, X.; Li, Y.; Zhang, Z.; Xu, C. High Strength and Microwave-Absorbing Polymer-Derived SiCN Honeycomb Ceramic Prepared by 3D Printing. *J Eur Ceram Soc* 2022, *42* (4), 1322–1331. https://doi.org/10.1016/j.jeurceramsoc.2021.12.003.
- (132) Seah, M. P. Summary of ISO/TC 201 Standard: VII ISO 15472 : 2001—Surface Chemical Analysis—x-Ray Photoelectron Spectrometers—Calibration of Energy Scales. *Surface and Interface Analysis* 2001, *31* (8), 721–723. https://doi.org/10.1002/sia.1076.
- (133) Santhosh, U.; Ahmad, J.; Easler, T.; Gowayed, Y. A Polymer Infiltration and Pyrolysis (PIP) Process Model for Ceramic Matrix Composites (Composite ceramics). *Journal of the American Ceramic Society* 2021, *104* (12), 6108–6130. https://doi.org/10.1111/jace.17966.
- (134) ANSTIS, G. R.; CHANTIKUL, P.; LAWN, B. R.; MARSHALL, D. B. A Critical Evaluation of Indentation Techniques for Measuring Fracture Toughness: I, Direct Crack Measurements. *Journal of the American Ceramic Society* 1981, *64* (9), 533–538. https://doi.org/10.1111/j.1151-2916.1981.tb10320.x.
- (135) De Jong, M.; Chen, W.; Angsten, T.; Jain, A.; Notestine, R.; Gamst, A.; Sluiter, M.; Ande, C. K.; Van Der Zwaag, S.; Plata, J. J.; Toher, C.; Curtarolo, S.; Ceder, G.; Persson, K. A.;

- Asta, M. Charting the Complete Elastic Properties of Inorganic Crystalline Compounds. *Sci Data* 2015, 2 (1), 1–13. https://doi.org/10.1038/sdata.2015.9.
- (136) Quinn, G. D. Fracture Toughness of Ceramics by the Vickers Indentation Crack Length Method: A Critical Review. *The American Ceramic Society* 2008, 45–62. https://doi.org/10.1002/9780470291313.ch5.
- (137) Kesmez, Ö.; Arpaç, E.; Kiraz, N.; Selli, N. T.; Tunalı, A. Mechanical, Anti-Bacterial, and Easy-to-Clean Properties of Hybrid Polymer-Based Composites Containing Modified SiO2 Prepared by Thermal Polymerization. *Chemical Papers* 2020, *74* (10), 3383–3398. https://doi.org/10.1007/s11696-020-01167-5.
- (138) Sahar Jafari, et al. Composition Limited Hydrogen Effusion Rate of A-SiNx: H Passivation Stack. *AIP Conf Proc* 2019, 2147, 050004. https://doi.org/https://doi.org/10.1063/1.5123853.
- (139) Michael A.Hickner and Tawanda J. Zimudzi. Signal Enhanced FTIR Analysis of Alignment in NAFION Thin Films at SiO2 and Au Interfaces. *ACS Macro Lett* 2016, 5, 83–87. https://doi.org/10.1021/acsmacro-lett.5b00800.
- (140) Superconductivity in Heavily Boron-Doped Silicon Carbide.Pdf. *Sci. Technol. Adv. Mater.* 2008, *9*, 044205. https://doi.org/10.1088/1468-6996/9/4/044205.
- (141) Cramer, C. L.; Armstrong, H.; Flores-Betancourt, A.; Han, L.; Elliott, A. M.; Lara-Curzio, E.; Saito, T.; Nawaz, K. Processing and Properties of SiC Composites Made via Binder Jet 3D Printing and Infiltration and Pyrolysis of Preceramic Polymer. *International Journal of Ceramic Engineering & Science* 2020, 2 (6), 320–331. https://doi.org/10.1002/ces2.10070.
- (142) Cramer, C. L.; Armstrong, H.; Flores-Betancourt, A.; Han, L.; Elliott, A. M.; Lara-Curzio, E.; Saito, T.; Nawaz, K. Processing and Properties of SiC Composites Made via Binder Jet 3D Printing and Infiltration and Pyrolysis of Preceramic Polymer. *International Journal of Ceramic Engineering & Science* 2020, 2 (6), 320–331. https://doi.org/10.1002/ces2.10070.
- (143) Yujuan Huang, Huiwen Xiong, et al. Ultralight Porous SiC with Attracting Strength: Freeze Casting of Polycarbosilane/SiCp/Camphene-Based Suspensions. Ceramics International 2020, pp 9582–9589. https://doi.org/https://doi.org/10.1016/j.ceramint.2019.12.223.
- (144) Allen, A. J.; Levin, I.; Witt, S. E. Materials Research & Measurement Needs for Ceramics Additive Manufacturing. *Journal of the American Ceramic Society* 2020, *103* (11), 6055–6069. https://doi.org/10.1111/jace.17369.

- (145) Jana, P.; Santoliquido, O.; Ortona, A.; Colombo, P.; Sorarù, G. D. Polymer-Derived SiCN Cellular Structures from Replica of 3D Printed Lattices. *Journal of the American Ceramic Society* 2018, *101* (7), 2732–2738. https://doi.org/10.1111/jace.15533.
- (146) Hagelüken, L.; Sasikumar, P. V. W.; Lee, H. Y.; Di Stadio, D.; Chandorkar, Y.; Rottmar, M.; Maniura-Weber, K.; Blugan, G.; Brugger, J. Multiscale 2D/3D Microshaping and Property Tuning of Polymer-Derived SiCN Ceramics. *J Eur Ceram Soc* 2022, *42* (5), 1963–1970. https://doi.org/10.1016/j.jeurceramsoc.2021.12.044.
- (147) Ren, Z.; Mujib, S. Bin; Singh, G. High-Temperature Properties and Applications of Si-Based Polymer-Derived Ceramics: A Review. *Materials* 2021, *14* (3), 1–18. https://doi.org/10.3390/ma14030614.
- (148) Hull, C. W. Apparatus for Production of Three-Dimensional Objects by Stereolithography. U.S. Patent No 4,575,300. Washington DC: Patent and Trademak Office, 1986.
- (149) Huang, K.; Elsayed, H.; Franchin, G.; Colombo, P. Complex SiOC Ceramics from 2D Structures by 3D Printing and Origami. *Addit Manuf* 2020, *33*, 101144. https://doi.org/10.1016/j.addma.2020.101144.
- (150) Chen, H.; Guo, L.; Zhu, W.; Li, C. Recent Advances in Multi-Material 3D Printing of Functional Ceramic Devices. *Polymers (Basel)* 2022, *14* (21). https://doi.org/10.3390/polym14214635.
- (151) Tehfe, M. A.; Louradour, F.; Lalevée, J.; Fouassier, J. P. Photopolymerization Reactions: On the Way to a Green and Sustainable Chemistry. *Applied Sciences (Switzerland)* 2013, 3 (2). https://doi.org/10.3390/app3020490.
- (152) Scarparo, M. A. F.; Kiel, A.; Zhiyao, Z.; Ferrari, C. A.; Chen, Q. J.; Miller, A. S.; Allen, S. D. Study of Resin Based Materials Using CO2 Laser Stereolithography. *Polymer* (*Guildf*) 1997, 38 (9), 2175–2181. https://doi.org/10.1016/S0032-3861(96)00763-X.
- (153) Kam, D.; Rulf, O.; Reisinger, A.; Lieberman, R.; Magdassi, S. 3D Printing by Stereolithography Using Thermal Initiators. *Nature Communications* 2024 15:1 2024, 15 (1), 1–10. https://doi.org/10.1038/s41467-024-46532-0.
- (154) Jardini, A. L. M.; MacIel, R.; Scarparo, M. A. F.; Andrade, S. R.; Moura, L. F. M. Improvement of the Spatial Resolution of Prototypes Using Infrared Laser Stereolithography on Thermosensitive Resins. *J Mater Process Technol* 2006, *172* (1), 104–109. https://doi.org/10.1016/J.JMATPROTEC.2005.09.012.
- (155) Namazu, T.; Ishikawa, T.; Hasegawa, Y. Influence of Polymer Infiltration and Pyrolysis Process on Mechanical Strength of Polycarbosilane-Derived Silicon Carbide Ceramics. *J Mater Sci* 2011, 46 (9), 3046–3051. https://doi.org/10.1007/s10853-010-5182-0.

- (156) *X-ray Photoelectron Spectroscopy (XPS) Reference Pages*. M.C. Biesinger. http://www.xpsfitting.com/.
- (157) Cramer, C. L.; Elliott, A. M.; Lara-Curzio, E.; Flores-Betancourt, A.; Lance, M. J.; Han, L.; Blacker, J.; Trofimov, A. A.; Wang, H.; Cakmak, E.; Nawaz, K. Properties of SiC-Si Made via Binder Jet 3D Printing of SiC Powder, Carbon Addition, and Silicon Melt Infiltration. *Journal of the American Ceramic Society* 2021, *104* (11), 5467–5478. https://doi.org/10.1111/jace.17933.
- (158) Oh, J. W.; Park, J.; Nahm, S.; Choi, H. SiC-Si Composite Part Fabrication via SiC Powder Binder Jetting Additive Manufacturing and Molten-Si Infiltration. *Int J Refract Metals Hard Mater* 2021, *101*, 105686. https://doi.org/10.1016/j.ijrmhm.2021.105686.
- (159) Park, K. M.; Min, K. S.; Roh, Y. S. Design Optimization of Lattice Structures under Compression: Study of Unit Cell Types and Cell Arrangements. *Materials* 2022, *15* (1). https://doi.org/10.3390/ma15010097.
- (160) Zheng, X.; Lee, H.; Weisgraber, T. H.; Shusteff, M.; DeOtte, J.; Duoss, E. B.; Kuntz, J. D.; Biener, M. M.; Ge, Q.; Jackson, J. A.; Kucheyev, S. O.; Fang, N. X.; Spadaccini, C. M. Ultralight, Ultrastiff Mechanical Metamaterials. *Science* (1979) 2014, 344 (6190), 1373–1377. https://doi.org/10.1126/science.1252291.
- (161) Li, J.; Yu, Z.; Zhou, Z.; Wang, Y.; Li, J. Mechanical Analysis and Failure Modes Prediction of Composite Rock under Uniaxial Compression. *Sci Rep* 2021, *11* (1). https://doi.org/10.1038/s41598-021-02331-x.
- (162) Colombo, P.; Hellmann, J. R.; Shelleman, D. L. Mechanical Properties of Silicon Oxycarbide Ceramic Foams. *Journal of the American Ceramic Society* 2001, 84 (10), 2245–2251. https://doi.org/10.1111/j.1151-2916.2001.tb00996.x.
- (163) St-Pierre, L.; Fleck, N. A.; Deshpande, V. S. The Predicted Compressive Strength of a Pyramidal Lattice Made from Case Hardened Steel Tubes. *Int J Solids Struct* 2014, *51* (1), 41–52. https://doi.org/10.1016/j.ijsolstr.2013.09.008.
- (164) Barros, M. L.; Scarparo, M. A. F.; Kiel, A.; Gerck, E.; Hurtak, J. J. Stereolithography with Thermosensitive Resins Using a CO2 Laser. *J Appl Polym Sci* 1994, *54* (10), 1575–1578. https://doi.org/10.1002/app.1994.070541022.
- (165) Packirisamy, S.; Sreejith, K. J.; Devapal, D.; Swaminathan, B. Polymer-Derived Ceramics and Their Space Applications. *Handbook of Advanced Ceramics and Composites* 2020, 1–107. https://doi.org/10.1007/978-3-319-73255-8\_31-2.
- (166) V. V. Kidalov, S. A. K. et al. Properties of SiC Films Obtained by the Method of Substitution of Atoms on Porous Silicon. *ECS Journal of Solid State Science and Technology* 2018, *4* (7), 158–160. https://doi.org/10.1149/2.0061804jss.

- (167) Thulasiraman, A. V.; Ganesapillai, M. A Systematic Review on the Synthesis of Silicon Carbide: An Alternative Approach to Valorisation of Residual Municipal Solid Waste. *Processes* 2023, Vol. 11, Page 283 2023, 11 (1), 283. https://doi.org/10.3390/PR11010283.
- (168) Delage, J.; Saiz, E.; Al Nasiri, N. Fracture Behaviour of SiC/SiC Ceramic Matrix Composite at Room Temperature. *J Eur Ceram Soc* 2022, 42 (7), 3156–3167. https://doi.org/10.1016/J.JEURCERAMSOC.2022.01.060.
- (169) Viard, A.; Fonblanc, D.; Lopez-Ferber, D.; Schmidt, M.; Lale, A.; Durif, C.; Balestrat, M.; Rossignol, F.; Weinmann, M.; Riedel, R.; Bernard, S. Polymer Derived Si–B–C–N Ceramics: 30 Years of Research. *Adv Eng Mater* 2018, *20* (10), 1800360. https://doi.org/10.1002/ADEM.201800360.
- (170) Ren, Z.; Mujib, S. Bin; Singh, G. High-Temperature Properties and Applications of Si-Based Polymer-Derived Ceramics: A Review. *Materials* 2021, *14* (3), 1–18. https://doi.org/10.3390/MA14030614.
- (171) Sarraf, F.; Churakov, S. V.; Clemens, F. Preceramic Polymers for Additive Manufacturing of Silicate Ceramics. *Polymers (Basel)* 2023, *15* (22), 1–29. https://doi.org/10.3390/POLYM15224360.
- (172) Colombo, P.; Sglavo, V.; Pippel, E.; Woltersdorf, J. Joining of Reaction-Bonded Silicon Carbide Using a Preceramic Polymer. *J Mater Sci* 1998, *33* (9), 2405–2412. https://doi.org/10.1023/A:1004312109836/METRICS.
- (173) Wen, Q.; Yu, Z.; Riedel, R. The Fate and Role of in Situ Formed Carbon in Polymer-Derived Ceramics. *Prog Mater Sci* 2019, *109*, 100623. https://doi.org/10.1016/j.pmatsci.2019.100623.
- (174) Colombo, P.; Mera, G.; Riedel, R.; Sorarù, G. D. Polymer-Derived Ceramics: 40 Years of Research and Innovation in Advanced Ceramics. *Journal of the American Ceramic Society* 2010, *93* (7), 1805–1837. https://doi.org/10.1111/J.1551-2916.2010.03876.X.
- (175) Lacelle, T.; Sampson, K. L.; Yazdani Sarvestani, H.; Rahimizadeh, A.; Barroeta Robles, J.; Mirkhalaf, M.; Rafiee, M.; Jakubinek, M. B.; Paquet, C.; Ashrafi, B. Additive Manufacturing of Polymer Derived Ceramics: Materials, Methods, and Applications. *APL Mater* 2023, *11* (7), 70602. https://doi.org/10.1063/5.0151661/2901841.
- (176) Halloran, J. W. Ceramic Stereolithography: Additive Manufacturing for Ceramics by Photopolymerization. 2016. https://doi.org/10.1146/annurev-matsci-070115-031841.
- (177) Zocca, A.; Gomes, C. M.; Staude, A.; Bernardo, E.; Günster, J.; Colombo, P. SiOC Ceramics with Ordered Porosity by 3D-Printing of a Preceramic Polymer. *Materials Research Society* 2013, 28 (17), 2243–2252. https://doi.org/10.1557/jmr.2013.129.

- (178) Yazdani Sarvestani, H.; Lacelle, T.; Sohrabi-Kashani, A.; Shashoua, A.; Karamzadeh, V.; Ravanbakhsh, H.; Robitaille, A.; Lavoie, H.; Paquet, C.; Jakubinek, M. B.; Ashrafi, B. 3D-Printed Polymer-Derived Ceramics with Tunable Cellular Architectures. *Appl Mater Today* 2024, *39*, 102327. https://doi.org/10.1016/J.APMT.2024.102327.
- (179) Xiong, S.; Liu, J.; Cao, J.; Li, Z.; Idrees, M.; Lin, X.; Long, Z.; Liu, Z.; Wang, P.; Liu, C.; Chen, Z. 3D Printing of Crack-Free Dense Polymer-Derived Ceramic Monoliths and Lattice Skeletons with Improved Thickness and Mechanical Performance. *Addit Manuf* 2022, *57*, 102964. https://doi.org/10.1016/J.ADDMA.2022.102964.
- (180) Xia, A.; Yin, J.; Chen, X.; Liu, X.; Huang, Z. Polymer-Derived Si-Based Ceramics: Recent Developments and Perspectives. *Crystals* 2020, Vol. 10, Page 824 2020, 10 (9), 824. https://doi.org/10.3390/CRYST10090824.
- (181) Du, W.; Ma, B.; Thomas, J.; Singh, D. Concurrent Reaction-Bonded Joining and Densification of Additively Manufactured Silicon Carbide by Liquid Silicon Infiltration. *J Eur Ceram Soc* 2023, *43* (6), 2345–2353. https://doi.org/10.1016/J.JEURCERAMSOC.2023.01.032.
- (182) Rui, M.; Zhang, Y.; Ye, J. Environment-Friendly Preparation of Reaction-Bonded Silicon Carbide by Addition of Boron in the Silicon Melt. *Materials* 2021, *14* (5), 1–9. https://doi.org/10.3390/MA14051090.
- (183) Raj, P.; Gupta, G. S.; Rudolph, V. Silicon Carbide Formation by Carbothermal Reduction in the Acheson Process: A Hot Model Study. *Thermochim Acta* 2020, 687, 178577. https://doi.org/10.1016/J.TCA.2020.178577.
- (184) Hackbarth, H. G.; Key, T. S.; Ackley, B. J.; Opletal, G.; Rawal, A.; Gallington, L.; Yang, Y.; Thomsen, L.; Dickerson, M. B.; Pruyn, T. L.; Bedford, N. M. Uncovering Atomic-Scale Polymer-to-Ceramic Transformations in SiC Polymer Derived Ceramics from Polycarbosilanes. *J Eur Ceram Soc* 2024, 44 (4), 1932–1945. https://doi.org/10.1016/J.JEURCERAMSOC.2023.11.014.
- (185) Filsinger, D. H.; Bourrie, D. B. Silica to Silicon: Key Carbothermic Reactions and Kinetics. *Journal of the American Ceramic Society* 1990, *73* (6), 1726–1732. https://doi.org/10.1111/J.1151-2916.1990.TB09820.X.
- (186) Zhu, S.; Ding, S.; Xi, H.; Wang, R. Low-Temperature Fabrication of Porous SiC Ceramics by Preceramic Polymer Reaction Bonding. *Mater Lett* 2005, *59* (5), 595–597. https://doi.org/10.1016/J.MATLET.2004.11.003.
- (187) Santhosh, B.; Vakifahmetoglu, C.; Ionescu, E.; Reitz, A.; Albert, B.; Sorarù, G. D. Processing and Thermal Characterization of Polymer Derived SiCN(O) and SiOC Reticulated Foams. *Ceram Int* 2020, *46* (5), 5594–5601. https://doi.org/10.1016/J.CERAMINT.2019.11.003.

- (188) Yuan, Z.; Zhang, Y.; Zhou, Y.; Dong, S. Effect of Solid Loading on Properties of Reaction Bonded Silicon Carbide Ceramics by Gelcasting. *RSC Adv* 2014, *4* (92), 50386–50392. https://doi.org/10.1039/C4RA05817H.
- (189) Kumar, P. V.; Gupta, G. S. Study of Formation of Silicon Carbide in the Acheson Process. *Steel Research* 2002, *73* (2), 31–38. https://doi.org/10.1002/SRIN.200200170.
- (190) Margiotta, J. C.; Zhang, D.; Nagle, D. C.; Feeser, C. E. Formation of Dense Silicon Carbide by Liquid Silicon Infiltration of Carbon with Engineered Structure. *Materials Research Society* 2008, *23* (5), 1237–1248. https://doi.org/10.1557/JMR.2008.0167.
- (191) Hofbauer, P. J.; Raether, F. Effects of Oxygen on the Liquid Silicon Infiltration (LSI) Process. *Open Ceramics* 2023, *14*, 100337. https://doi.org/10.1016/j.oceram.2023.100337.
- (192) Mainzer, B.; Roder, K.; Wöckel, L.; Frieß, M.; Koch, D.; Nestler, D.; Wett, D.; Podlesak, H.; Wagner, G.; Ebert, T.; Spange, S. Development of Wound SiCBNx/SiNx/SiC with near Stoichiometric SiC Matrix via LSI Process. *J Eur Ceram Soc* 2016, *36* (7), 1571–1580. https://doi.org/10.1016/J.JEURCERAMSOC.2015.12.015.
- (193) Roger, J.; Marchais, A.; Le Petitcorps, Y. Examination of the Interaction between Liquid Silicon and Bulk Silicon Carbide. *J Cryst Growth* 2015, 426, 1–8. https://doi.org/http://dx.doi.org/10.1016/j.jcrysgro.2015.05.013.
- (194) Tang, J.; Liu, M.; Wei, Y.; Yang, Y.; Huang, Z. An Efficient and Low-Cost Liquid Silicon Infiltration Method to Prepare SiC-Coated Carbon Short Fiber for Fiber Protection of Cf/SiC Ceramic Matrix Composites. *Ceram Int* 2021, 47 (9), 13235–13241. https://doi.org/10.1016/J.CERAMINT.2021.01.115.
- (195) Foti, G. Silicon Carbide: From Amorphous to Crystalline Material. *Appl Surf Sci* 2001, *184* (1–4), 20–26. https://doi.org/10.1016/S0169-4332(01)00751-6.
- (196) Konstantinou, G.; Kakkava, E.; Hagelüken, L.; Warriam Sasikumar, P. V.; Wang, J.; Makowska, M. G.; Blugan, G.; Nianias, N.; Marone, F.; Van Swygenhoven, H.; Brugger, J.; Psaltis, D.; Moser, C. Additive Micro-Manufacturing of Crack-Free PDCs by Two-Photon Polymerization of a Single, Low-Shrinkage Preceramic Resin. *Addit Manuf* 2020, 35, 101343. https://doi.org/10.1016/J.ADDMA.2020.101343.
- (197) Barroso, G. S.; Krenkel, W.; Motz, G. Low Thermal Conductivity Coating System for Application up to 1000 °C by Simple PDC Processing with Active and Passive Fillers. *J Eur Ceram Soc* 2015, *35* (12), 3339–3348. https://doi.org/10.1016/J.JEURCERAMSOC.2015.02.006.
- (198) Rotaru, R.; Savin, M.; Tudorachi, N.; Peptu, C.; Samoila, P.; Sacarescu, L.; Harabagiu, V. Ferromagnetic Iron Oxide–Cellulose Nanocomposites Prepared by Ultrasonication. *Polym Chem* 2018, *9* (7), 860–868. https://doi.org/10.1039/C7PY01587A.

- (199) Hu, Z.; Zheng, D.; Tu, R.; Yang, M.; Li, Q.; Han, M.; Zhang, S.; Zhang, L.; Goto, T. Structural Controlling of Highly-Oriented Polycrystal 3C-SiC Bulks via Halide CVD. *Materials* 2019, *12* (3). https://doi.org/10.3390/MA12030390.
- (200) Gorovenko, V. I.; Knyazik, V. A.; Shteinberg, A. S. High-Temperature Interaction between Silicon and Carbon. *Ceram Int* 1993, *19* (2), 129–132. https://doi.org/10.1016/0272-8842(93)90086-7.
- (201) Devon, M. J.; Rudin, A. A Simple Technique for Measuring the Refractive Index of Polymer Latexes at Various Wavelengths. *J Appl Polym Sci* 1987, *34* (2), 469–476. https://doi.org/10.1002/APP.1987.070340202.
- (202) Edward D. Palik. *Handbook of Optical Constants of Solids*; Academic Press: Boston, 1985.
- (203) Viard, A.; Fonblanc, D.; Lopez-Ferber, D.; Schmidt, M.; Lale, A.; Durif, C.; Balestrat, M.; Rossignol, F.; Weinmann, M.; Riedel, R.; Bernard, S. Polymer Derived Si–B–C–N Ceramics: 30 Years of Research. *Adv Eng Mater* 2018, 20 (10), 1800360. https://doi.org/10.1002/ADEM.201800360.
- (204) Wen, Q.; Qu, F.; Yu, Z.; Graczyk-Zajac, M.; Xiong, X.; Riedel, R. Si-Based Polymer-Derived Ceramics for Energy Conversion and Storage. *Journal of Advanced Ceramics* 2021 11:2 2022, 11 (2), 197–246. https://doi.org/10.1007/S40145-021-0562-2.
- (205) Konstantinou, G.; Kakkava, E.; Hagelüken, L.; Sasikumar, P. V. W.; Wang, J.; Makowska, M. G.; Blugan, G.; Nianias, N.; Marone, F.; Swygenhoven, H. Van; Brugger, J.; Psaltis, D.; Moser, C. Additive Micro-Manufacturing of Crack-Free PDCs by Two-Photon Polymerization of a Single, Low-Shrinkage Preceramic Resin. *Addit Manuf* 2020, 35, 101343. https://doi.org/10.1016/J.ADDMA.2020.101343.
- (206) Filsinger, D. H.; Bourrie, D. B. Silica to Silicon: Key Carbothermic Reactions and Kinetics. *Journal of the American Ceramic Society* 1990, *73* (6), 1726–1732. https://doi.org/10.1111/J.1151-2916.1990.TB09820.X.
- (207) Bernard, S.; Fiaty, K.; Cornu, D.; Miele, P.; Laurent, P. Kinetic Modeling of the Polymer-Derived Ceramics Route: Investigation of the Thermal Decomposition Kinetics of Poly[B-(Methylamino)Borazine] Precursors into Boron Nitride. 2006. https://doi.org/10.1021/jp055981m.
- (208) Mera, G.; Gallei, M.; Bernard, S.; Ionescu, E. Ceramic Nanocomposites from Tailor-Made Preceramic Polymers. *Nanomaterials* 2015, *5* (2), 468. https://doi.org/10.3390/NANO5020468.
- (209) Hackbarth, H. G.; Key, T. S.; Ackley, B. J.; Opletal, G.; Rawal, A.; Gallington, L.; Yang, Y.; Thomsen, L.; Dickerson, M. B.; Pruyn, T. L.; Bedford, N. M. Uncovering Atomic-Scale Polymer-to-Ceramic Transformations in SiC Polymer Derived Ceramics from

- Polycarbosilanes. *J Eur Ceram Soc* 2024, *44* (4), 1932–1945. https://doi.org/10.1016/J.JEURCERAMSOC.2023.11.014.
- (210) Luan, X.; Zhang, Q.; Yu, R.; Wang, L.; Cheng, L.; Li, J.; Fasel, C.; Riedel, R. Polyborosilazane-Derived High Temperature Resistant SiBCNO. 2019. https://doi.org/10.1002/adem.201801295.
- (211) Wen, Q.; Yu, Z.; Riedel, R. The Fate and Role of in Situ Formed Carbon in Polymer-Derived Ceramics. *Prog Mater Sci* 2019, *109*, 100623. https://doi.org/10.1016/j.pmatsci.2019.100623.
- (212) Galusek, D.; Lenčéš, Z.; Šajgalík, P.; Riedel, R. THERMAL ANALYSIS STUDY OF POLYMER-TO-CERAMIC CONVERSION OF ORGANOSILICON PRECURSORS. *Journal of Mining and Metallurgy* 2008, *44*, 35–38. https://doi.org/10.2298/JMMB0801035G.
- (213) Ionescu, E.; Riedel, R.; Clarke, D. R. The Thermal Conductivity of Polymer-Derived Amorphous Si-O-C Compounds and Nano-Composites. 2016. https://doi.org/10.1111/jace.13947.
- (214) Daniel, I.; Gillet, P.; Poe, B. T.; McMillan, P. F. In-Situ High-Temperature Raman Spectroscopic Studies of Aluminosilicate Liquids. *Phys Chem Miner* 1995, 22 (2), 74–86. https://doi.org/10.1007/BF00202467/METRICS.
- (215) Raman Spectroscopy for Detecting Supported Planar Lipid Bilayers Composed of Ganglioside-GM1/Sphingomyelin/Cholesterol in the Presence of Amyloid-β.
- (216) Kleebe, H.-J.; Gregori, G.; Babonneau, F.; Blum, Y. D.; MacQueen, D. B.; Masse, S. Evolution of C-Rich SiOC Ceramics: Part I. Characterization by Integral Spectroscopic Techniques: Solid-State NMR and Raman Spectroscopy. *International Journal of Materials Research* 2006, 97 (6), 699–709. https://doi.org/10.1515/IJMR-2006-0115.
- (217) Jiang, T.; Wang, Y.; Wang, Y.; Orlovskaya, N.; An, L. Quantitative Raman Analysis of Free Carbon in Polymer-Derived Ceramics. *Journal of the American Ceramic Society* 2009, 92 (10), 2455–2458. https://doi.org/10.1111/J.1551-2916.2009.03233.X.
- (218) Ma, C.; Li, Y. Phase Transition in Polymer Derived Ceramics (PDCs) and Its Effect on Mechanical Response.
- (219) Ma, C.; Li, Y. Phase Transition in Polymer Derived Ceramics (PDCs) and Its Effect on Mechanical Response.
- (220) Ma, C.; Li, Y. MODELING OF PHASE TRANSITION IN FABRICATION OF POLYMER-DERIVED CERAMICS (PDCS).

- (221) D'Elia, R.; Dusserre, G.; Confetto, S. Del; Eberling-Fux, N.; Descamps, C.; Cutard, T. Effect of Dicumyl Peroxide Concentration on the Polymerization Kinetics of a Polysilazane System. *Polym Eng Sci* 2018, *58* (6), 859–869. https://doi.org/10.1002/PEN.24638.
- (222) Kramm, G.; Mölders, N. Planck's Blackbody Radiation Law: Presentation in Different Domains and Determination of the Related Dimensional Constants.
- (223) GEORGE SOCRATES. Infrared and Raman Group. The University of West London 2001.
- (224) Mera, G.; Navrotsky, A.; Sen, S.; Kleebe, H.-J.; Riedel, R. Polymer-Derived SiCN and SiOC Ceramics-Structure and Energetics at the Nanoscale. https://doi.org/10.1039/c2ta00727d.
- (225) Kar, R.; Maiti, N. Observation of D Band Splitting in Vertically Aligned Graphene Nanowalls and Their Evolution with Laser Power during Raman Spectroscopy. *Journal of Nanoparticle Research* 2021, 23 (1), 1–10. https://doi.org/10.1007/S11051-021-05147-Y/FIGURES/9.
- (226) Khafizov, M.; Chauhan, V.; Wang, Y.; Riyad, F.; Hang, N.; Hurley, D. H.; Khafizov, M.; Chauhan, V.; Wang, Y.; Riyad, F.; Hang, N.; Hurley, D. H. Investigation of Thermal Transport in Composites and Ion Beam Irradiated Materials for Nuclear Energy Applications. *JMatR* 2017, *32* (1), 204–216. https://doi.org/10.1557/JMR.2016.421.
- (227) Liu, L. Z.; Wang, J.; Wu, X. L.; Li, T. H.; Chu, P. K. Longitudinal Optical Phonon-Plasmon Coupling in Luminescent 3C-SiC Nanocrystal Films. *Opt Lett* 2010, *35* (23), 4024. https://doi.org/10.1364/OL.35.004024.
- (228) Bakthavatsalam, S.; Dodo, K.; Sodeoka, M. A Decade of Alkyne-Tag Raman Imaging (ATRI): Applications in Biological Systems. *RSC Chem Biol* 2021, *2* (5), 1415. https://doi.org/10.1039/D1CB00116G.
- (229) Koyanagi, T.; Katoh, Y.; Lance, M. J. Raman Spectroscopy of Neutron Irradiated Silicon Carbide: Correlation among Raman Spectra, Swelling, and Irradiation Temperature. *Journal of Raman Spectroscopy* 2018, *49* (10), 1686–1692. https://doi.org/10.1002/JRS.5425.
- (230) He, R.; Ding, G.; Zhang, K.; Li, Y.; Fang, D. Fabrication of SiC Ceramic Architectures Using Stereolithography Combined with Precursor Infiltration and Pyrolysis. *Ceram Int* 2019, *45* (11), 14006–14014. https://doi.org/10.1016/J.CERAMINT.2019.04.100.
- (231) Steyrer, B.; Busetti, B.; Harakály, G.; Liska, R.; Stampfl, J. Hot Lithography vs. Room Temperature DLP 3D-Printing of a Dimethacrylate. *Addit Manuf* 2018, *21*, 209–214. https://doi.org/10.1016/J.ADDMA.2018.03.013.

- (232) Li, C.; Snarr, S. E.; Denlinger, E. R.; Irwin, J. E.; Gouge, M. F.; Michaleris, P.; Beaman, J. J. Experimental Parameter Identification for Part-Scale Thermal Modeling of Selective Laser Sintering of PA12. *Addit Manuf* 2021, *48*, 102362. https://doi.org/10.1016/J.ADDMA.2021.102362.
- (233) Harada, M.; Hamaura, N.; Ochi, M.; Agari, Y. Thermal Conductivity of Liquid Crystalline Epoxy/BN Filler Composites Having Ordered Network Structure. *Compos B Eng* 2013, 55, 306–313. https://doi.org/10.1016/J.COMPOSITESB.2013.06.031.
- (234) Wei, X.; Wang, Z.; Tian, Z.; Luo, T. Thermal Transport in Polymers: A Review. *J Heat Transfer* 2021, *143* (7), 1ENG. https://doi.org/10.1115/1.4050557/1104438.
- (235) Mehra, N.; Mu, L.; Ji, T.; Yang, X.; Kong, J.; Gu, J.; Zhu, J. Thermal Transport in Polymeric Materials and across Composite Interfaces. *Appl Mater Today* 2018, *12*, 92–130. https://doi.org/10.1016/J.APMT.2018.04.004.
- (236) Hu, Q.; Bai, X.; Zhang, C.; Zeng, X.; Huang, Z.; Li, J.; Li, J.; Zhang, Y. Oriented BN/Silicone Rubber Composite Thermal Interface Materials with High out-of-Plane Thermal Conductivity and Flexibility. *Compos Part A Appl Sci Manuf* 2022, *152*, 106681. https://doi.org/10.1016/J.COMPOSITESA.2021.106681.
- (237) Pateloup, V.; Michaud, P.; Chartier, T. Optimization of Part Orientation and Adapted Supports for Manufacturing of Ceramic Parts by Stereolithography Using Finite Element Simulations. *Open Ceramics* 2021, *6*, 100132. https://doi.org/10.1016/J.OCERAM.2021.100132.
- (238) Sanderson, B.; Diba, F.; Kishawy, H.; Hosseini, A. Finite Element Analysis of Additive Manufacturing of Polymers Using Selective Laser Sintering. *International Journal of Advanced Manufacturing Technology* 2023, *129* (3–4), 1631–1647. https://doi.org/10.1007/S00170-023-12370-5/FIGURES/13.
- (239) Ali, S. F.; Delattre, C.; Rafaralahy, H.; Didier, G.; Jeandel, G.; Boutayeb, M. Control of Transient Coupled Radiative-Conductive Heat Transfer Equation. *IFAC Proceedings Volumes* 2010, *43* (8), 424–429. https://doi.org/10.3182/20100712-3-FR-2020.00070.